Strojniški vestnik

Journal of Mechanical Engineering

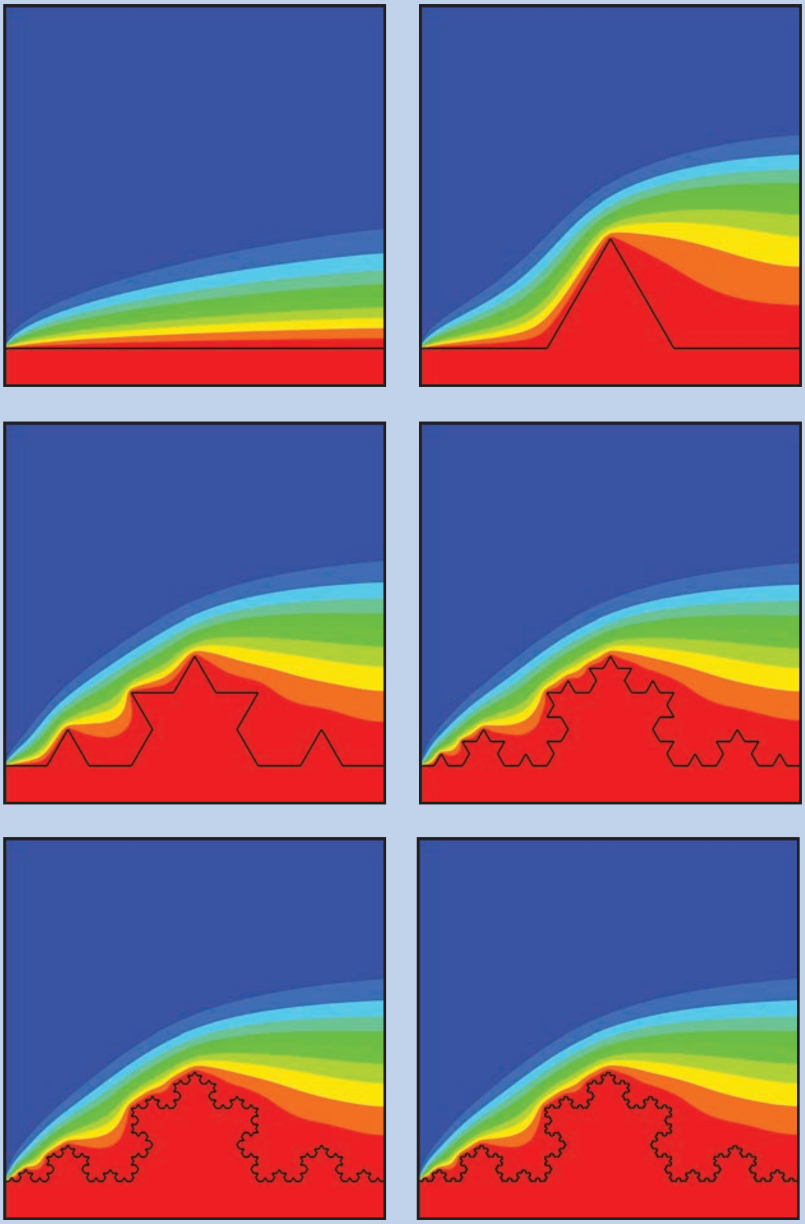

no. 9
year 2022
volume 68

Strojniški vestnik – Journal of Mechanical Engineering (SV-JME)

Aim and Scope

The international journal publishes original and (mini)review articles covering the concepts of materials science, mechanics, kinematics, thermodynamics, energy and environment, mechatronics and robotics, fluid mechanics, tribology, cybernetics, industrial engineering and structural analysis.
The journal follows new trends and progress proven practice in the mechanical engineering and also in the closely related sciences as are electrical, civil and process engineering, medicine, microbiology, ecology, agriculture, transport systems, aviation, and others, thus creating a unique forum for interdisciplinary or multidisciplinary dialogue.
The international conferences selected papers are welcome for publishing as a special issue of SV-JME with invited co-editor(s).

Editorial Office
University of Ljubljana, Faculty of Mechanical Engineering
SV-JME, Aškerčeva 6, SI-1000 Ljubljana, Slovenia
Phone: 386 (0)1 4771 137
Fax: 386 (0)1 2518 567
info@sv-jme.eu, http://www.sv-jme.eu

Print: Demat d.o.o., printed in 250 copies

Founders and Publishers
University of Ljubljana, Faculty of Mechanical Engineering, Slovenia
University of Maribor, Faculty of Mechanical Engineering, Slovenia
Association of Mechanical Engineers of Slovenia
Chamber of Commerce and Industry of Slovenia, Metal Processing Industry Association

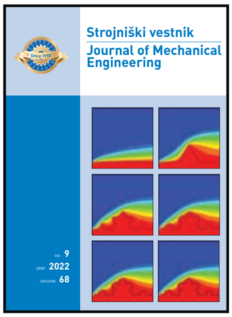

Cover:
Using smaller and smaller rulers the coast length limits to infinity. If this logic is applied to the fractal heat sink geometry, infinite cooling capacity should be obtained using fractals with mathematically infinite surface area. On the figures the formation of Koch snowflake geometry from flat line to 1024 elements on the 5th step is shown. Using colours, the temperature field of cooling air flowing from the left-hand side is plotted. One should note the similarity of geometry and temperature development up to the last figure, where the changes become minor.

Image Courtesy:
Matjaž Ramšak, University of Maribor, Faculty of Mechanical Engineering, Slovenia

ISSN 0039-2480, ISSN 2536-2948 (online)

General information

Strojniški vestnik – Journal of Mechanical Engineering is published in 11 issues per year (July and August is a double issue).

Institutional prices include print & online access: institutional subscription price and foreign subscription €100,00 (the price of a single issue is €10,00); general public subscription and student subscription €50,00 (the price of a single issue is €5,00). Prices are exclusive of tax. Delivery is included in the price. The recipient is responsible for paying any import duties or taxes. Legal title passes to the customer on dispatch by our distributor. Single issues from current and recent volumes are available at the current single-issue price. To order the journal, please complete the form on our website. For submissions, subscriptions and all other information please visit: *http://www.sv-jme.eu*.

You can advertise on the inner and outer side of the back cover of the journal. The authors of the published papers are invited to send photos or pictures with short explanation for cover content.

We would like to thank the reviewers who have taken part in the peer-review process.

The journal is subsidized by Slovenian Research Agency.

SV-JME is indexed / abstracted in: SCI-Expanded, Compendex, Inspec, ProQuest-CSA, SCOPUS, TEMA. The list of the remaining bases, in which SV-JME is indexed, is available on the website.

Strojniški vestnik - Journal of Mechanical Engineering is available on *https://www.sv-jme.eu*.

Contents

Strojniški vestnik - Journal of Mechanical Engineering
volume 68, (2022), number 9
Ljubljana, September 2022
ISSN 0039-2480

Published monthly

Papers

Strojniški vestnik - Journal of Mechanical Engineering 68(2022)9, 517-528

DOI:10.5545/sv-jme.2022.28
Original Scientific Paper
Received for review: 2022-01-24
Received revised form: 2022-04-25
Accepted for publication: 2022-06-13

Fractal Geometry as an Effective Heat Sink

Matjaž Ramšak[1]
[1]Faculty of Mechanical Engineering, University of Maribor, Slovenia

"How long is the coast of Britain?" was the question stated by Mandelbrot. Using smaller and smaller rulers the coast length limits to infinity. If this logic is applied to the fractal heat sink geometry, infinite cooling capacity should be obtained using fractals with mathematically infinite surface area. The aim of this article is to check this idea using Richardson extrapolation of numerical simulation results varying the fractal element length from one to zero. As expected, the extrapolated cooling capacity has a noninfinite limit. The presented fractal heat sink geometry is non-competitive to the straight fins.

Keywords: fractal heat sink, light-emitting diode and central processing unit cooling, conjugate heat transfer, laminar flow, boundary element method, Koch snowflake

Highlights
- *Infinite fractal heat transfer area leads to zero Nusselt number. Their product limits to finite value of heat flow.*
- *Richardson extrapolation of numerical simulation results confirm that.*
- *Fractal flow pattern follows fractal geometry.*
- *Fractal heat sink could not compete with straight fins.*
- *Conjugate heat transfer is simulated using boundary element method inhouse code.*

0 INTRODUCTION

The convective heat transfer per unit time $\dot{Q}$ between a heat sink and the fluid is computed as

$$\dot{Q} = h\,A\,\Delta T\ , \tag{1}$$

where h is the heat transfer coefficient, A the heat transfer area, and ΔT the temperature difference between the solid surface and fluid free stream. If the heat transfer area tends to infinity, the heat transfer power should tend to infinity too, presuming that the heat transfer coefficient and ΔT are finite nonzero values. The aim of this research is to test this assumption using computational fluid dynamics (CFD). The test is performed using a sequence of Koch snowflake fractal formation starting from a straight line to some small finite value, as shown in the last figure in the article. Using Richardson extrapolation [1], the results are extrapolated to the infinite surface area. If the result of this study confirms the idea, a very effective cooling device should be gained using fractal geometry.

The fractal geometry is encountered in nature in many shapes and purposes. For example, the blood veins with capillaries in lungs for heat and mass exchange. It is well known that the nature evolution solutions are superior to engineering ones in many areas. If this is true for heat sinks, then a fractal heat sink must exist to be better than simple one with the straight fins which is used nowadays in most cases. As it is a popular slogan: there is a room for improvement.

The geometry of heat sinks is subject of many recent articles [2–6]. The fractals are not an unknown topic in this subject. In most papers, fractal geometry is used to characterise the surface roughness [7], where the correlation between the critical heat flow and the fractal surface roughness of the pressure tubes from the cool heavy water moderator is investigated. A 3D laminar flow in a microchannel is analysed numerically in [8], where near wall swirls are obtained of size 1 μm. In the minority group of papers, fractal geometry is used to describe the material porosity, for example [9–12].

Elaborate review article of fractal heat exchangers is written in [13] where the list of similar articles is presented. Almost all of them are numerical simulations. The numerical feasibility study of fractal heat sink is published in [14], where fractal like heat sink is proposed for cooling of electronic device. The conjugate heat transfer in a fractal tree like channels network heat sink is studied numerically and experimentally [15]. A conclusion is made that a fractal heat sink has lower pressure drop, more uniform temperature field distribution, and higher coefficient of performance than that of the traditional helical channel net heat sink. In the latest review article [16] on optimization design of heat sinks the fractal geometry is mentioned only in one cited article [17]. A simple heat sink is simulated consisting of a fractal split microchannel up to second iteration formation only. The challenge of high cooling power in electronic devices and its dissipation using bionic Y-shaped

*Corr. Author's Address: University of Maribor, Faculty of Mechanical Engineering, Smetanova 11, 2000 Maribor, Slovenia, matjaz.ramsak@um.si

fractals is the subject of very recent work of He et al. [18].

The Koch snowflake fractal geometry, again only up to the second iteration formation, is found in [19], where it is applied for micro mixer baffles geometry. The laminar flow is solved up to $Re = 100$, coincidentally the same as in our work.

Table 1. *Results sensitivity on mesh density for $Re = 1$ and solid fluid heat conductivity ratio $k = 1$*

Mesh data				
Mesh name	coarse	medium	fine	finest
Number of Nodes [*1000]	47	92	231	457
Nodes on Koch shortest element	3	3	5	7
Nodes on Outlet	90	180	226	300
Results for isothermal computation				
Number of iterations	940	880	955	940
CPU [h] (serial run)	14	36	100	351
AVG (Interface vorticity)	-2.872	-2.779	-2.682	-2.662
Error to coarser mesh [%]	-	3.35	3.62	0.75
Num. acc. estimation [1] [%]	-	-	1.43	0.50
Results for thermal computation				
AVG (Interface temp.)	0.6536	0.6533	0.6529	0.6528
Error to coarser mesh [%]	-	0.05	0.06	0.02
Num. acc. estimation [1] [%]	-	-	0.04	0.02
Nusselt number	0.5173	0.5206	0.5211	0.5218
Error to coarser mesh [%]	-	0.62	0.10	0.13
Num. acc. estimation [1] [%]	-	-	0.08	0.16

The conjugate heat transfer in this work is computed using in house code based on mixed boundary elements and subdomain boundary element method (BEM). The idea of mixed boundary elements [20] is to split the function and flux approximation using continuous interpolation polynomials for function and discontinuous for function derivative in normal direction to the boundary element. In this manner the problem of undefined normal direction on the corner flux nodal points is elegantly avoided. The main advantage of subdomain technique is sparse matrix in comparison to the classic BEM, where only the boundary of computational domain must be discretised. The subdomain technique in its limit version by [21], where each subdomain is consisted of three or four boundary elements as triangle or quadrilateral subdomain, resulted in extremely sparse system matrix like in finite element method (FEM). The interface boundary conditions between mixed elements of subdomains lead to overdetermined matrix, which is solved using fast iterative least squares method, [22]. The code has been successfully used and validated for the conjugate heat transfer Benchmark revision [23].

The paper is organised as follows. The Problem definition is stated after the Introduction. In the next section Results and Discussion, the main subsection is the last one titled The infinite heat flow idea. Prior to this, various tests are performed for the shortest simulated fractal length $(1/3)^5 = 0.004$ in the fifth iteration consisting of $4^5 = 1024$ elements: mesh sensitivity, Reynolds dependency for isothermal solution, influence of solid/fluid thermal conductivity ratio and influence of Reynolds number value on thermal solution. The paper finishes with concluding remarks on enhanced heat sinks using fractal geometry.

1 PROBLEM DEFINITION

The geometry of the Koch snowflake represents the first cut out of the heat sink of the high heat density source, such as light-emitting diode (LED) or central processing unit (CPU) processor, as shown in Fig. 1. The bottom of the solid wall is heated to a constant temperature. The cooling fluid is flowing into the domain with constant velocity. The zero gradient outlet boundary condition is prescribed. It is not physically adequate since the flow field is not fully developed, but the obtained flow field is as expected at the outflow region and serves well for the numerical example aim. The buoyancy effect is neglected. This could be justified by small fluid solid temperature difference or orienting the gravity in the third dimension not influencing the flow field in the 2D computational cross-section shown in Fig. 1.

The problem is nondimensionalized as follows. Length quantities are nondimensionalized by the length of the computational domain in the mean flow direction. The velocity is nondimensionalized by the inlet velocity. The Reynolds number is computed as $Re = Velocity@inlet \times Length/\nu$. The steady laminar flow of air is presumed as a cooling fluid. The Prandtl number is set to 0.71. The bottom dimensionless temperature is 1.0 and inlet temperature is zero. In this manner the temperature difference ΔT is defined to be 1 in Eq. (11). Computing the steady state solution, the fluid solid thermal diffusivity ratio is the last solution parameter investigated in next sections.

The non-dimensional form of governing equations for a 2D incompressible laminar flow are written using the nondimensional stream function vorticity formulation of Navier-Stokes equations. Stream function equation ψ is

$$\frac{\partial^2 \psi}{\partial x^2} + \frac{\partial^2 \psi}{\partial y^2} = -\omega \,. \tag{2}$$

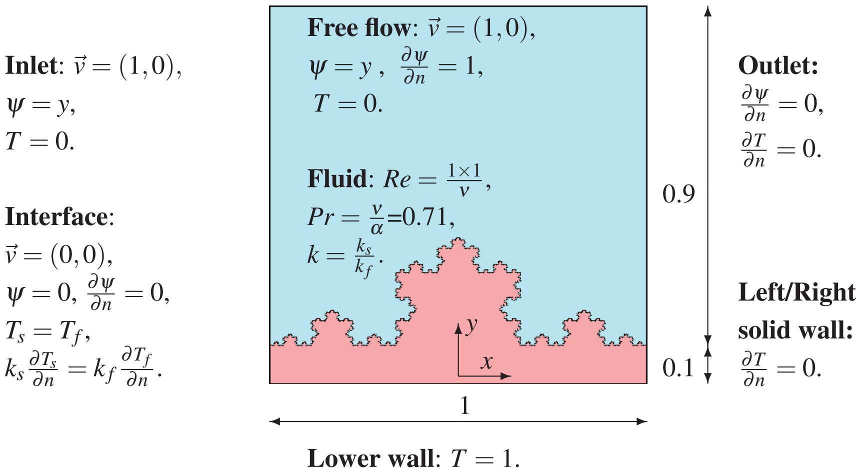

Fig. 1. *The geometry of computational domain and boundary conditions*

Table 2. *Results sensitivity on solid fluid conductivity ratio k for $Re = 1$*

Solid fluid conductivity ratio k	1	10	100	1000	10^4	10^5
AVG (Interface temperature)	0.6529	0.9175	0.9900	0.9990	0.9999	1.0000
Change to prior - lower k [%]	-	28.84	7.32	0.90	0.09	0.01
AVG (Outlet temperature)	0.4030	0.5236	0.5526	0.5562	0.5565	0.5565
Change to prior - lower k [%]	-	23.03	5.25	0.65	0.05	0.00
AVG (Nusselt number)	0.5211	1.1167	1.3659	1.3994	1.4033	1.4036
Change to prior - lower k [%]	-	53.33	18.25	2.39	0.28	0.02
Heat flow $\dot{Q}$ [W]	0.0309	0.0663	0.0811	0.0831	0.0833	0.0833
Change to prior - lower k [%]	-	53.33	18.25	2.39	0.28	0.02
Heat transfer coef. h [W/m^{2}K]	0.0073	0.0157	0.0192	0.0197	0.0198	0.0198
Change to prior - lower k [%]	-	53.33	18.25	2.39	0.28	0.02

Table 3. *Results sensitivity on Reynolds number for $k = 10$*

Reynolds number Re	1	10	100
AVG (Interface vorticity)	-2.682	-2.777	-3.629
AVG (Interface temperature)	0.9175	0.9054	0.8471
AVG (Outlet temperature)	0.5236	0.4766	0.3331
Nusselt number	1.1167	1.2231	1.7366
Heat flow $\dot{Q}$ [W]	0.0663	0.0726	0.1031
Heat transfer coef. h [W/m^{2}K]	0.0157	0.0172	0.0245

Vorticity equation ω is

$$\frac{\partial \omega}{\partial t} + \frac{\partial (v_x \omega)}{\partial x} + \frac{\partial (v_y \omega)}{\partial y} = \frac{1}{Re} \nabla^2 \omega \,, \tag{3}$$

where v_x is the velocity in x direction computed as $v_x = \partial \psi / \partial y$ and v_y as $v_y = -\partial \psi / \partial x$. The energy equation within the fluid region is

$$\frac{\partial T}{\partial t} + \frac{\partial (v_x T)}{\partial x} + \frac{\partial (v_y T)}{\partial y} = \frac{1}{RePr} \nabla^2 T \,, \tag{4}$$

where T is non-dimensional fluid temperature.

Energy equation within the solid region is

$$\frac{\partial T}{\partial t} = \left(\frac{\alpha_s}{\alpha_f} \right) \frac{1}{RePr} \nabla^2 T \,, \tag{5}$$

where α_s and α_f are diffusivities for the solid and fluid regions respectively. For details on equations derivation [23]. The mechanism of heat conduction and its background is clearly explained in Liu et al. [9].

The interface boundary conditions on the wall between solid and fluid are written as temperature equality

$$T_f = T_s \,, \tag{6}$$

and heat flux equality as

$$k_f \left(\frac{\partial T}{\partial n} \right)_{f,interface} = -k_s \left(\frac{\partial T}{\partial n} \right)_{s,interface} \,, \tag{7}$$

where the n is unit normal direction to the fluid solid interface. The local Nusselt number is defined as the

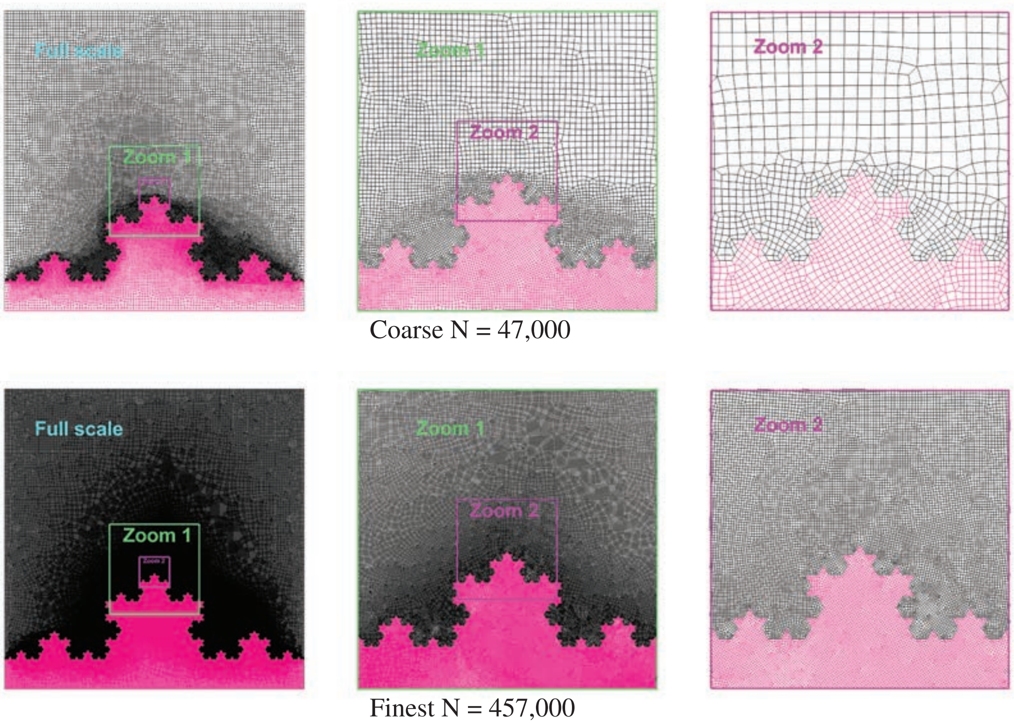

Fig. 2. *Meshes used; Increasing the mesh density the number of outlet nodes are 90, 180, 226 and 300 while on the shortest fractal element of the Koch boundary are 3, 3, 5 and 7 nodes*

Table 4. *Average values at the Koch fluid solid interface for fractal geometry sequence; the fractal element length is denoted using l and the complete interface length using L; the Richardson extrapolation [1] to infinite boundary is presented in the line $l = 0$ including extrapolation accuracy estimation interval. In the last line, the best guestimate values are stated*

l	L	ω_{Koch}	T_{Koch}	Nu	$\dot{Q}$	h
1.000	1.000	-18.58	0.9999	8.158	0.1149	0.1149
0.333	1.333	-15.52	0.9998	6.071	0.1140	0.0855
0.111	1.778	-8.958	0.9998	4.980	0.1247	0.0701
0.037	2.370	-6.397	0.9998	3.954	0.1320	0.0557
0.012	3.160	-4.578	0.9998	3.051	0.1358	0.0430
0.004	4.214	-3.629	0.9998	2.332	0.1384	0.0328
0.0	∞	-2.518	0.9998	-0.899	0.1446	-0.0127
acc. est. $\pm$		1.0	0.0000	1.6	0.0081	0.0219
guestimate		-2.518	0.9998	0	0.1446	0

temperature derivative at the fluid side of the fluid solid interface as

$$Nu = -\frac{\partial T}{\partial n}\bigg|_{f,interface} . \tag{8}$$

The average Nusselt number Nu is the integral value computed as

$$Nu = \frac{1}{L}\int_0^L Nu\, dl \,, \tag{9}$$

where L is the interface wall length. The heat flow $\dot{Q}$ is computed using its definition as

$$\dot{Q} = -Ak_f \left(\frac{\partial T}{\partial n}\right)_f = (L \cdot 1)k_f Nu \,, \tag{10}$$

where A is the actual interface area computed as $L \cdot 1$. The unity length is defined on the 3rd dimension. Heat transfer coefficient h is computed as

$$h = \frac{\dot{Q}}{A\Delta T} \tag{11}$$

where ΔT is one in this case.

In this paper only a steady solution is computed. The steady solution is solid thermal diffusivity α_s independent since the time derivative is zero, see Eq. (5). In this manner the solid fluid thermal conductivity ratio k defined as $k = k_s/k_f$ is the only solid material

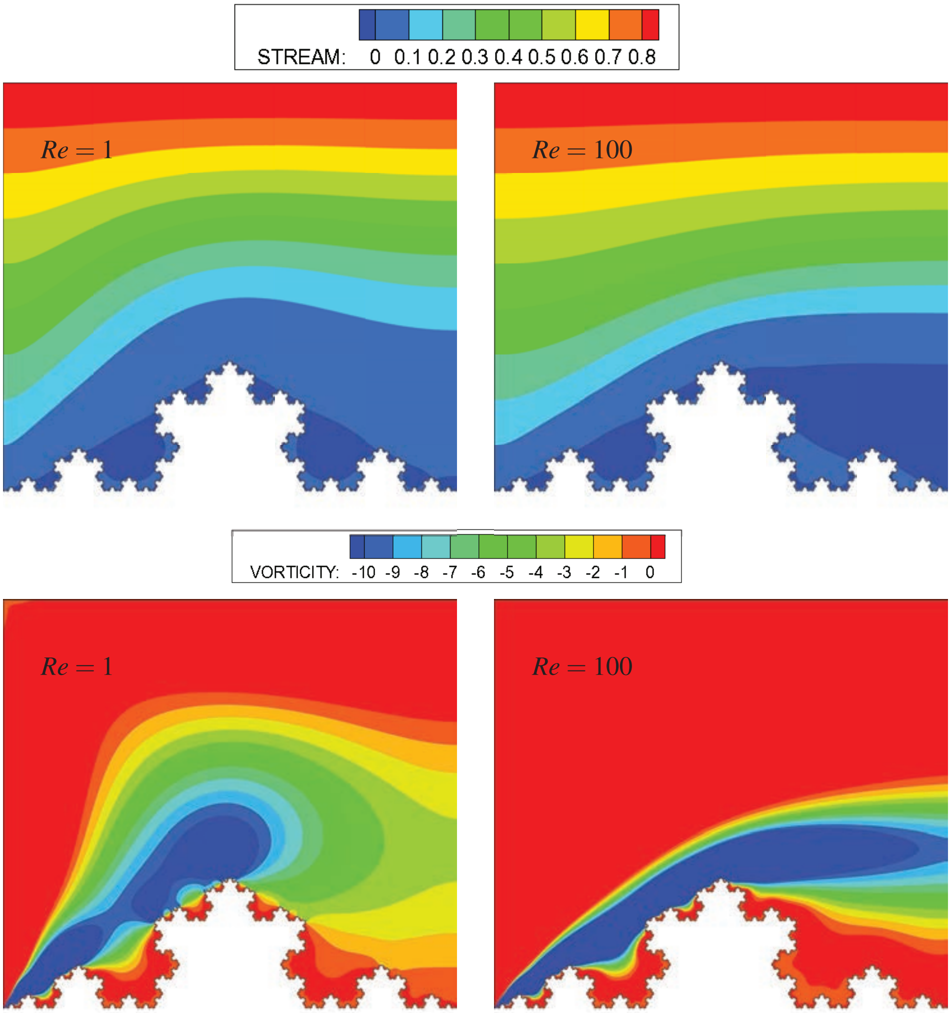

Fig. 3. *The Reynolds number dependency of the stream function and vorticity contour plots*

parameter arising from interface boundary condition Eq. (7), influencing the solution.

All governing equations can be written in the same general form and solved using practically the same multidomain BEM solver applying different boundary conditions for each governing equation. The solver is explained in a detail in [24]. The validation of the developed multidomain BEM solver [23] where the benchmark solution of conjugate heat transfer of backward facing step problem is computed.

2 RESULTS AND DISCUSSION

The basic aim of the article is to check the assumption about the infinite heat flow for infinite length of fractal solid-fluid interface. Before this main numerical test, a few necessary tests are performed using the finest fractal geometry which is numerically the most cumbersome to solve.

2.1 Mesh Sensitivity Study

The aim of this test is to choose the appropriate mesh density and numerical solution accuracy estimation using standard procedure described in [1]. Four mesh densities were used: coarse, medium, fine and finest, see Fig. 2. In Tab. 1 the results are shown for the selected case $Re = 1$ and solid fluid conductivity ratio $k = 1$.

Three integral values are selected as numerical solution accuracy indicators: average (AVG) value of vorticity, temperature and Nusselt value on the solid fluid interface. The AVG (Interface vorticity)

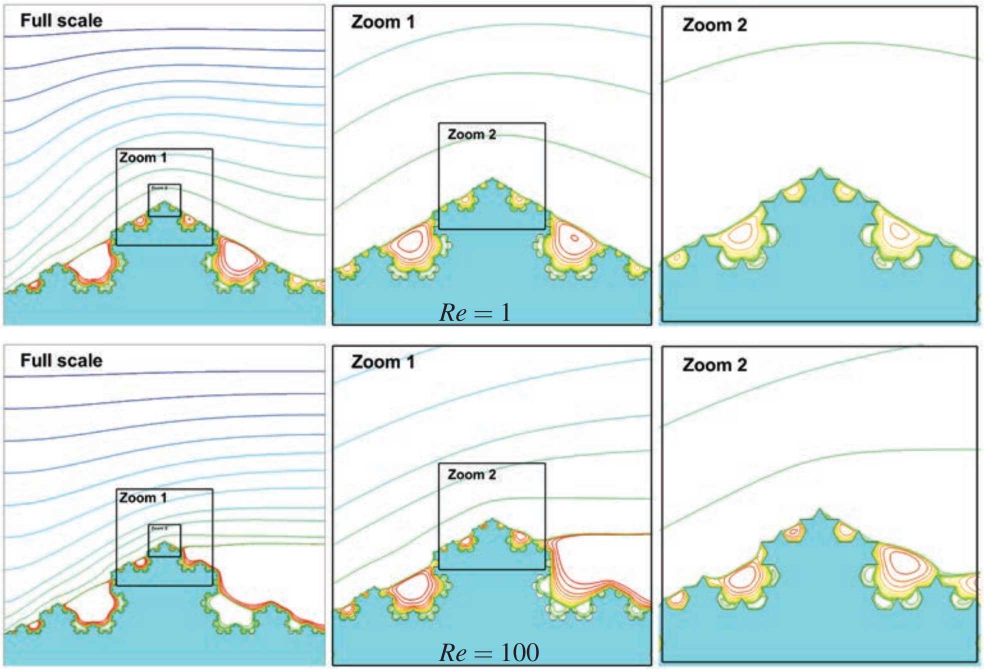

Fig. 4. *Geometry and flow (stream function) self similarity at Reynolds numbers 1 and 100*

numerical solution accuracy is the worst among all, being 0.50 %, which is to be expected since the interface vorticity is the most nonlinear and therefore difficult to solve. The thermal solutions are less mesh sensitive, resulting in maximal 0.02 % error for average temperatures and 0.16 % error for the Nusselt number. Obviously and intuitively, the temperature profile over the interface is less mesh dependent than the vorticity one. Based on the CPU consumption and basic aim, the fine mesh was chosen as a default mesh for all further computations resulting in less than 1 % numerical solution accuracy. Similar numerical accuracy is published in the work [23] where using the same BEM code the benchmark conjugate heat transfer problem was solved.

2.2 Reynolds Number Dependency of Isothermal Solution

The contour plots are presented in Fig. 3 for stream function and vorticity field at $Re = 1$ and $Re = 100$. Close to the Koch snowflake boundary, the streamlines in Figs. 3 are almost symmetrical with respect to the upstream and downstream sides for $Re = 1$. For a higher Re number the symmetry feature is altered, since the recirculation zone appears. In contrast to $Re = 1$, in general, the bright blue colour representing positive stream value change to dark blue colour representing negative stream value on the downstream side. The dark blue zones represent the clockwise and light blue counter clockwise rotation vortices. The symmetry issues are more evident in the smallest cavities. This feature is also visible on vorticity contour plots as a dark and bright red colour, representing the zero-value vorticity contour.

The flow self-similarity is discussed in the next paragraph. Streamlines are shown in Fig. 4, where two successive zooms are enlarged on the right-hand side of the full-scale plot. Zooms 1 and 2 were selected in such a manner that the geometric self-similarity is evident. The flow pattern self-similarity is obvious too, especially for $Re = 1$. The flow pattern is discussed in many aspects in our latest work completely dedicated to the isothermal solution [25].

2.3 Influence of Solid Fluid Conductivity Ratio k

The real solid fluid conductivity ratio k values are 16000, 9000 and 2300 for Cu, Al and steel heat sink material, respectively. The test values are chosen to be in the range from 1 to 10^5. The Nusselt

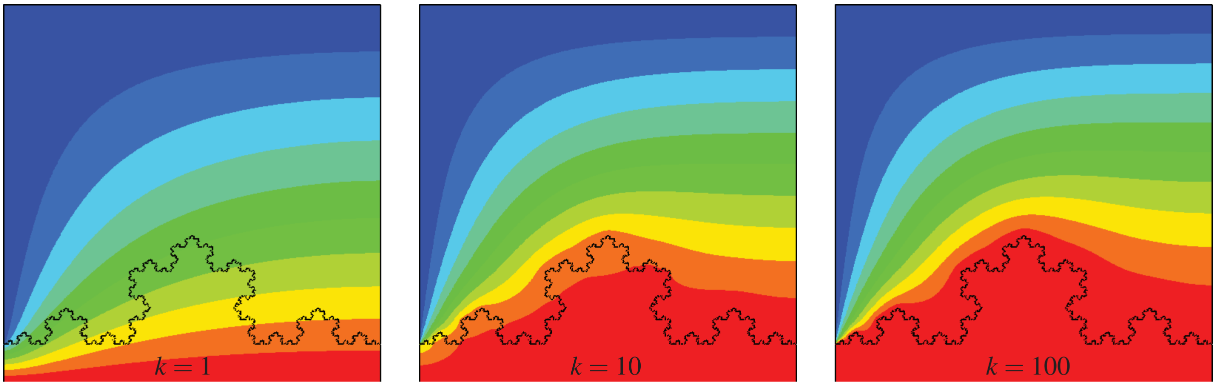

Fig. 5. *Influence of solid fluid conductivity ratio k on temperature field for $Re = 1$*

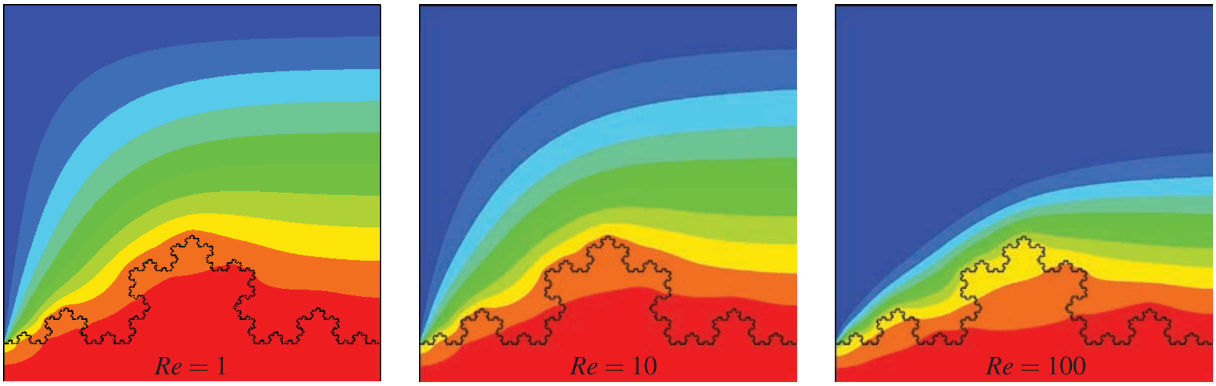

Fig. 6. *Influence of Reynolds number on temperature field for $k = 10$*

values are not changing significantly (only 2.39 %) when increasing k over 100, see Tab. 2 and Fig. 5, indicating no significant changes. Increasing k, solid gradients decrease obtaining an almost constant solid temperature. Replacing the steel with Al the cooling heat flow increases for 0.3 % in this problem configuration. The neglecting improvement of 0.02 % is obtained replacing Al with Cu.

Interesting temperature contours are obtained for $k = 1$, equalling the heat conductivity in fluid and solid, see Fig. 5. In this case ($Re = 1$), the solid domain influence on temperature nearly vanishes, since the conduction equals convection, obtaining large temperature gradients in the solid domain.

The Biot number ($Bi = Length \cdot h/k_s$) analysis follows. The characteristic *Length* is defined in this case as $Length = A/L$ where the A is finite heat sink cross section approximately $0.1 \cdot 1$ and L the length of the fractal cooling surface area. Increasing L to the infinity the characteristic length and Bi limits to zero. Additionally, increasing k and consequently k_s values the Bi number also limits to zero value. Both parameters clearly indicating very low Bi values and consequently the uniform solid temperature as already mentioned. Using results in Tab. 2 the maximum Bi number value is $Bi = 0.0002$ using $L = 4.214$, $Length = 0.0237$, $h = 0.0073$ and $k = 1$, confirming that heat conduction in solid prevails heat convection to fluid.

2.4 Influence of Reynolds Number on the Thermal Solution

For this test, the fluid solid conductivity ratio k value is fixed to 10 in order to obtain temperature changes in the solid. In this academic case the heat sink is made using isolative material such as wood or plastic. Increasing the Re number, the heat convection prevails over diffusion, resulting in nearly linear growth of the Nusselt number values, see Tab. 3 and Fig. 6. One should expect that increasing Re and consequently the cooling heat rate, the outlet temperature should increase too. Wrong, the outlet temperature decreases since the mass flow

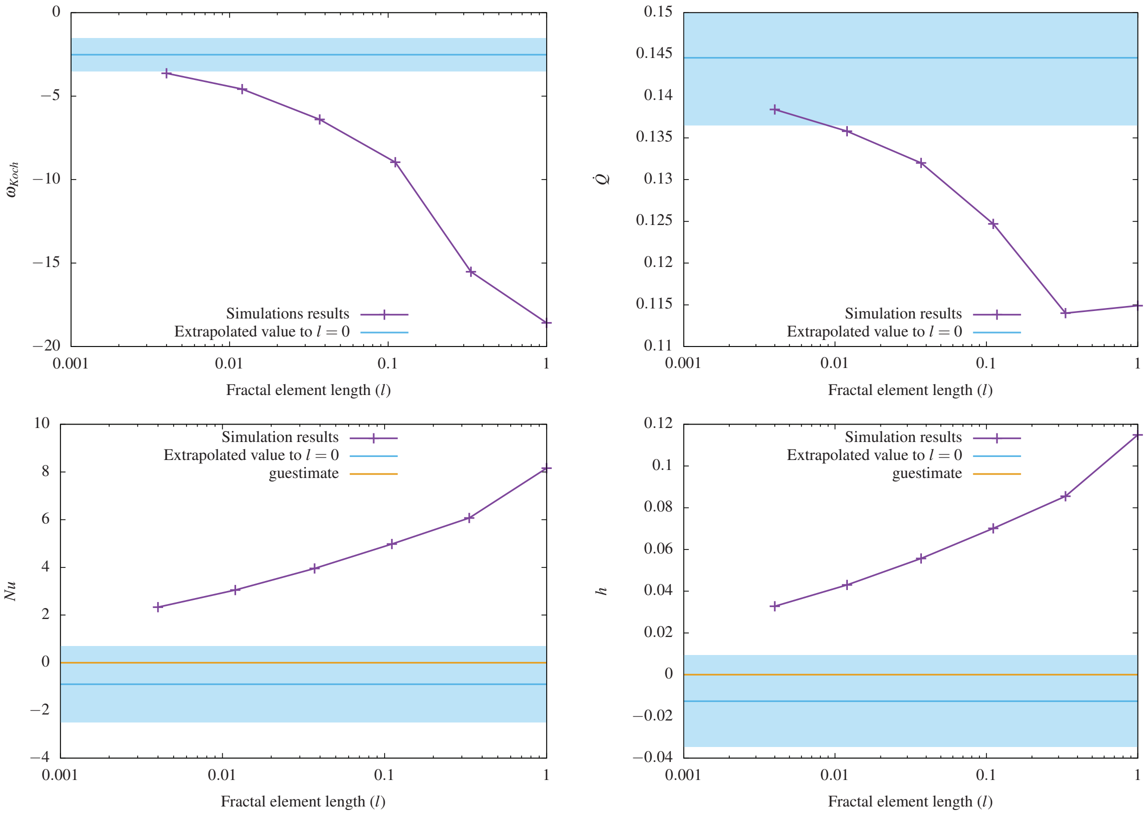

Fig. 7. *Graphical presentation of tabulated results in Tab. 4; the shaded area is accuracy estimation of extrapolated result value computed using [1]*

increases. The proper thermodynamic conclusion in this case would be: the enthalpy of outflow, computed as mass flow and temperature product, increases and exergy decreases. Increasing Re number the interface temperature decreases too, indicating higher temperature gradients and consequently, higher heat flux in the solid domain.

2.5 The Infinite Heat Flow Idea

The infinite heat flow idea is tested by forming Koch snowflake fractal geometry starting from the flat heat sink geometry denoted by $l = 1$, where l is the fractal element length. The next geometry iteration is obtained by dividing each fractal element by factor 3 and creating 4 new elements using the Koch snowflake formation procedure, see Fig. 8. In this manner, the Koch boundary length is increased by factor $4/3$ at each formation iteration giving an infinite limit. The final boundary length in this research is $(4/3)^5 = 4.214$ using 5th iteration formation and fractal element size $l = (1/3)^5 = 0.004$. Using Richardson extrapolation [1], the numerical result values limit is computed using l as mesh size parameter which tends to zero. The accuracy estimation is also a part of the extrapolation procedure results.

The infinite heat flow assumption is tested using $Re = 100$ and solid fluid conductivity ratio $k = 10^4$ which matches the Aluminium heat sink material approximately.

In the Figs. 8, 9 and 10 the contour plots of stream function, vorticity and temperature are plotted respectively for each fractal element length l. It is interesting and natural to expect that the flow fields have the same fractal nature as the geometry has in the Koch snowflake formation procedure. This is more evident in the upwind side of the heat sink in comparison to the downwind side where the recirculation zone is present.

The quantitative results are presented in Tab. 4 and graphically in Fig. 7. Observing the heat flow $\dot{Q}$ dynamics the smooth response is obtained generally. The only exception is in the first iteration between $l = 1.0$ and $l = 0.333$. The first question would be how it is possible, that the cooling heat flow is slightly lower for 0.8 % using a single rib ($l = 0.333$) comparing to the flat surface ($l = 1.0$). While the surface area

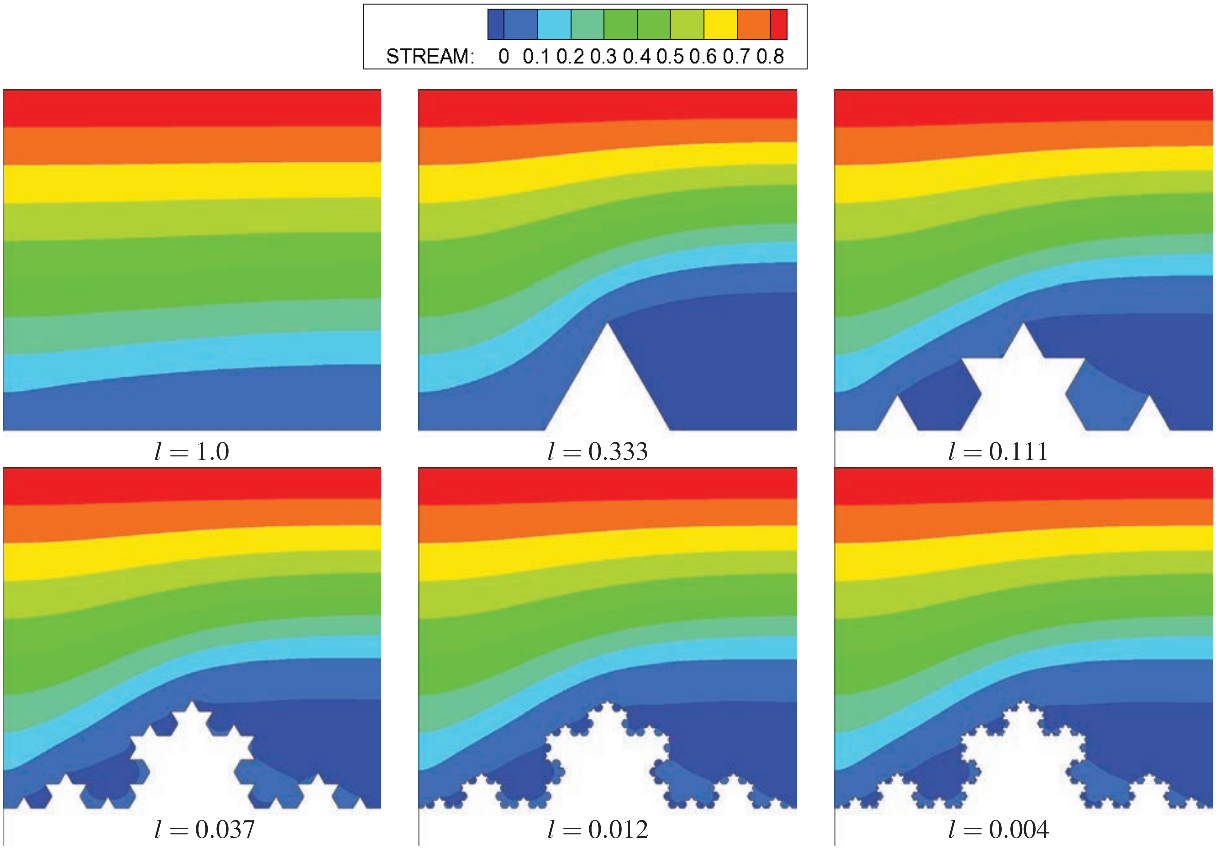

Fig. 8. *Stream function contours for the Koch snowflake formation procedure denoted by fractal element length l; the flow field have the same fractal nature as the geometry*

of ribbed surface A is increased, the heat transfer coefficient h is significantly decreased resulting in slightly lower heat flow which is their product $\dot{Q} = h \cdot A \cdot \Delta T$. In this case the cooling rib is more of a fluid flow and thermal obstacle than cooling enhanced as expected intuitively. Additionally, the recirculation zone performs thermal isolation increasing the thermal boundary layer thickness in downwind area comparing to the flat surface case, see Fig. 10.

The next objectivity of discussion is to verify that the five iterations of the Koch snowflake formation are enough for the testing aim. Comparing results in the last two figures, namely $l = 0.012$ and $l = 0.004$, the macro flow solution does not change any more significantly. Decreasing l further approaching the roughness size value, the flow would change only very close to the boundary until the viscous forces would damp the smallest swirls in cavities limiting to the hydraulic smooth surface flow. If the dimension of the heat sink would be 1 cm, then the shortest fractal element length $l = 0.004$ would be 40 μm, which is equivalent to the N11 Roughness Grade Number which is obtained using sand cast or hot roll manufacturing of heat sink, [26]. Finally, the minimal edge dimension of $l = 40$ μm is still big enough to be in the continuum mechanics having a Knudsen number value of 600.

3 CONCLUSIONS

The infinite cooling capacity idea is very naive. The numerical experiment annulated the idea of course. Decreasing the fractal length l to zero the main conclusions are:

- The area of interface surface converges to infinity.
- Nu and h converged to zero setting the convective heat flow to zero (bearing in mind the extrapolation error).
- The $\dot{Q}$ is increasing monotonically to a specific finite value: heat diffusion.

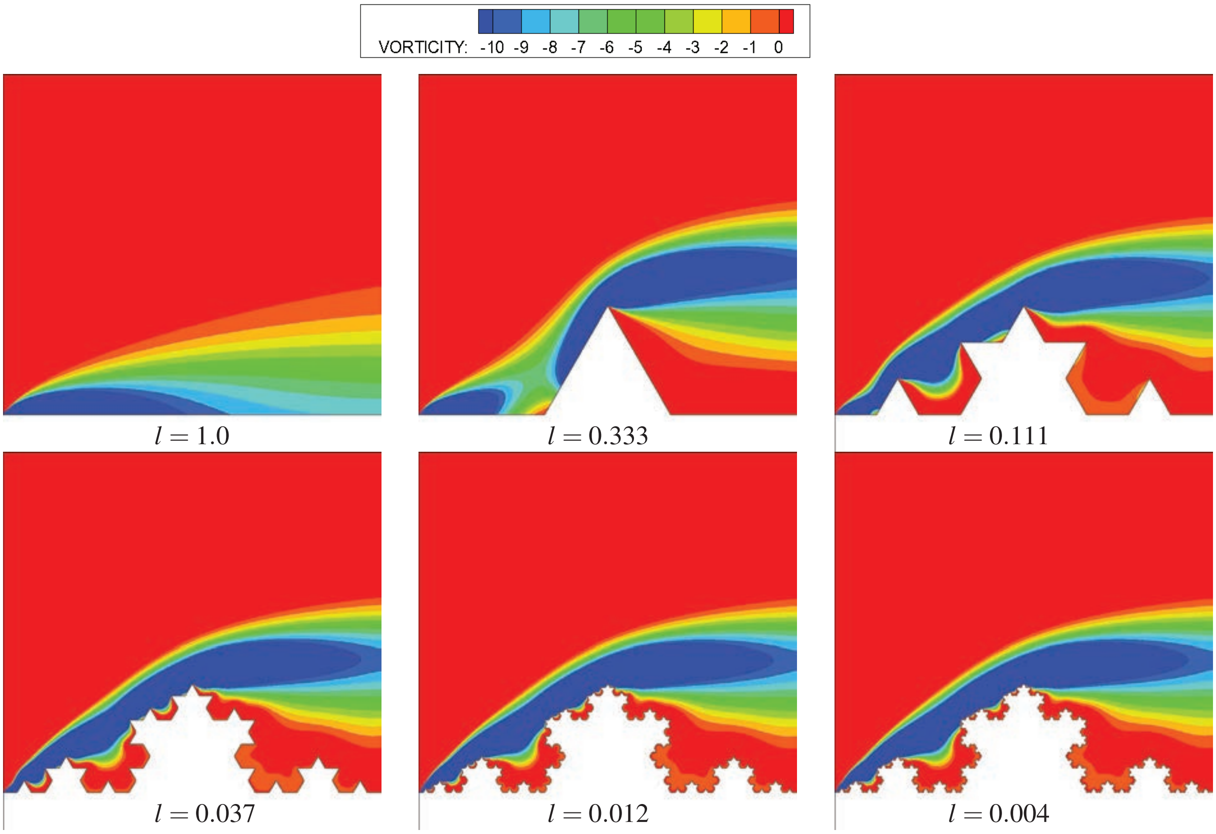

Fig. 9. *Vorticity function contours for the Koch snowflake formation procedure denoted by fractal element length l*

In this manner the resulting heat transfer Eq. (11) could be written as

$$\dot{Q} = \lim_{l \to 0} \Big((h \to 0)(A \to \infty)(\Delta T = 1) \Big), \qquad (12)$$

as stated in Eq. (10). Since the Nusselt number represents the ratio between convection and diffusion, setting the $Nu \to 0$ annulated heat convection leaving the diffusion the only heat transfer mechanism in the solid fluid interface, as it is the fact. The fact is also, that each real surface has a roughness, might be in the fractal manner or not, and that the heat convection from solid surface to fluid is achieved by heat diffusion only at the fluid solid interface. The numerical experiment in this article confirms this fact.

The fractal geometry heat sink as an effective heat sink? No. This kind of fractal heat sink is non-competitive to the simple straight fin heat sink. This is clearly revealed by almost constant fractal fin temperature for aluminium – air configuration in Tab. 2 and 4 indicating the optimal fin should be slenderer generating larger temperature changes.

4 ACKNOWLEDGEMENTS

Authors acknowledge the financial support from the Slovenian Research Agency (research core funding No. P2-0196).

5 REFERENCES

[1] AIAA (1994). Editorial policy statement on numerical accuracy and experimental uncertainty, *AIAA Journal*, vol. 32, no. 1., p. 3-8, **DOI:10.2514/3.48281**.

[2] Močnik, U., Blagojevič, B., Muhič, S. (2020). Numerical analysis with experimental validation of single-phase fluid flow in a dimple pattern heat exchanger channel. *Strojniški vestnik - Journal of Mechanical Engineering*, vol. 66, no. 9, p. 544-553, **DOI:10.5545/sv-jme.2020.6776**.

[3] Yadav, S., Pandey, K.M. (2018). A parametric thermal analysis of triangular fins for improved heat transfer in forced convection. *Strojniški vestnik - Journal of Mechanical Engineering*, vol. 64, no. 6, p. 401-411, **DOI:10.5545/sv-jme.2017.5085**.

[4] Al-Kouz, W.G., Kiwan, S., Alkhalidi, A., Sari, M., Alshare, A. (2018). Numerical study of heat transfer enhancement for

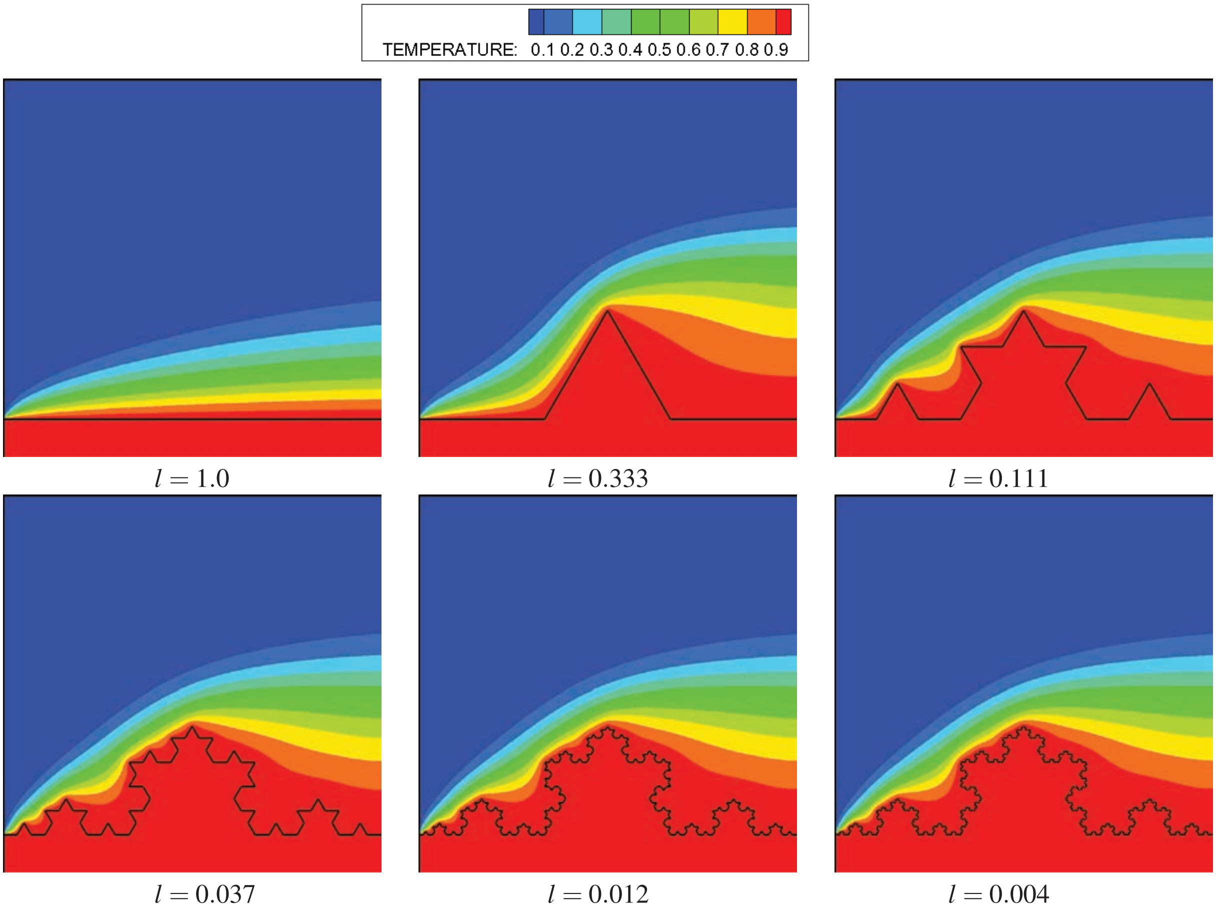

Fig. 10. *Temperature contours for the Koch snowflake formation procedure denoted by fractal element length l*

low-pressure flows in a square cavity with two fins attached to the hot wall using Al_2O_3-air nanofluid. *Strojniški vestnik - Journal of Mechanical Engineering*, vol. 64, no. 1, p. 26-36, **DOI:10.5545/sv-jme.2017.4989**.

[5] Čarnogurská, M., Příhoda, M., Lázár, M., Jasminská, N., Gallik, R., Kubik, M. (2016). Measuring selected parameters of polypropylene fibre heat exchangers. *Strojniški vestnik - Journal of Mechanical Engineering*, vol. 62, no. 6, p. 381-388, **DOI:10.5545/sv-jme.2015.3202**.

[6] Yayla, S. (2013). Flow characteristic of staggered multiple slotted tubes in the passage of a fin tube heat exchanger. *Strojniški vestnik - Journal of Mechanical Engineering*, vol. 59, no. 7-8, p. 462-472, **DOI:10.5545/sv-jme.2012.902**.

[7] Fong, R.W.L., McRae, G.A., Coleman, C.E., Nitheanandan, T., Sanderson, D.B. (2001). Correlation between the critical heat flux and the fractal surface roughness of zirconium alloy tubes. *Journal of Enhanced Heat Transfer*, vol. 8, no. 2, p. 137-146, **DOI:10.1615/JEnhHeatTransf.v8.i2.60**.

[8] Chen, Y., Zhang, C., Shi, M., Peterson, G.P. (2009). Role of surface roughness characterized by fractal geometry on laminar flow in microchannels. *Physical Review E*, vol. 80, art. ID 026301, **DOI:10.1103/PhysRevE.80.026301**.

[9] Liu, J., Xue, Y., Zhang, Q., Wang, H., Wang, S. (2022). Coupled thermo-hydro-mechanical modelling for geothermal doublet system with 3D fractal fracture. *Applied Thermal Engineering*, vol. 200, art. ID 117716, **DOI:10.1016/j.applthermaleng.2021.117716**.

[10] Cai, W., Chen, W., Wang, F. (2017). Three-dimensional hausdorff derivative diffusion model for isotropic/anisotropic fractal porous media. *Thermal Science*, vol. 22, no. suppl. 1, p. s1-s6, **DOI:10.2298/TSCI170630265C**.

[11] Gao, Y., Gao, F., Dong, G., Yan, W., Yang, X. (2019). The mechanical properties and fractal characteristics of the coal under temperature-gas-confining pressure. *Thermal Science*, vol. 23, no. suppl. 3, p. 789-798, **DOI:10.2298/TSCI180610094G**.

[12] Wang, Q.-L., Li, Z.-B., Kong, H.-Y., He, J.-H. (2015). Fractal analysis of polar bear hairs. *Thermal Science*, vol. 19, no. suppl. 1, p. 143-144, **DOI:10.2298/TSCI15S1S43W**.

[13] Huang, Z., Hwang, Y., Aute, V., Radermacher, R. (2016). Review of Fractal Heat Exchangers. *International Refrigeration and Air Conditioning Conference*. Paper 1725.

[14] Ikegami, S., Umetani, K., Hiraki, E., Sakai, S., Higashino, S. (2018). Feasibility study of fractal-fin heat sink for improving cooling performance of switching power converters. *IEEE International Telecommunications Energy Conference*, p. 1-8, **DOI:10.1109/INTLEC.2018.8612377**.

[15] Xia, C., Fu, J., Lai, J., Yao, X., Chen, Z. (2015). Conjugate heat transfer in fractal tree-like channels network heat sink for high-speed motorized spindle cooling. *Applied Thermal Engineering*, vol. 90, p. 1032-1042, **DOI:10.1016/j.applthermaleng.2015.07.024**.

[16] Ahmed, H.E., Salman, B.H., Kherbeet, A.Sh., Ahmed, M.I. (2018). Optimization of thermal design of heat sinks: A review. *International Journal of Heat and Mass Transfer*, vol. 118, p. 129-153, **DOI:10.1016/j.ijheatmasstransfer.2017.10.099**.

[17] Xu, S., Wang, W., Fang, K., Wong, C.-N. (2015). Heat transfer performance of a fractal silicon microchannel heat sink subjected to pulsation flow. *International Journal of Heat and Mass Transfer*, vol. 81, p. 33-40, **DOI:10.1016/j.ijheatmasstransfer.2014.10.002**.

[18] He, Z., Yan, Y., Zhao, T., Zhang, L., Zhang, Z. (2021). Multi-objective optimization and multi-factors analysis of the thermal/hydraulic performance of the bionic y-shaped fractal heat sink. *Applied Thermal Engineering*, vol. 195, art. ID 117157, **DOI:10.1016/j.applthermaleng.2021.117157**.

[19] Zhang, S., Chen, X., Wu, Z., Zheng, Y. (2019). Numerical study on stagger koch fractal baffles micromixer. *International Journal of Heat and Mass Transfer*, vol. 133, p. 1065-1073, **DOI:10.1016/j.ijheatmasstransfer.2019.01.009**.

[20] Ramšak, M., Škerget, L. (1999). Mixed boundary elements for laminar flows. *International Journal for Numerical Methods in Fluids*, vol. 31, no. 5, p. 861-877, **DOI:10.1002/(SICI)1097-0363(19991115)31:5<861::AID-FLD900>3.0.CO;2-S**.

[21] Žagar, I., Škerget, L. (1995). The numerical simulation of non-linear separation columns by boundary-domain integral formulation. *Computers & Chemical Engineering*, vol. 19, Suppl. 1, p. 785-790, **DOI:10.1016/0098-1354(95)87130-6**.

[22] Ramšak, M., Škerget, L. (2000). Iterative least squares methods for solving over-determined matrix for mixed boundary elements. *ZAMM Berlin*, vol. 80, no. 3, p. 657.

[23] Ramšak, M. (2015). Conjugate heat transfer of backward-facing step flow: A benchmark problem revisited. *International Journal of Heat and Mass Transfer*, vol. 84, p. 791-799, **DOI:10.1016/j.ijheatmasstransfer.2015.01.067**.

[24] Ramšak, M., Škerget, L. (2014). A highly efficient multidomain bem for multimillion subdomains. *Engineering Analysis with Boundary Elements*, vol. 43, p. 76-85, **DOI:10.1016/j.enganabound.2014.03.009**.

[25] Ramšak, M. (2019). Multidomain bem for laminar flow in complex fractal geometry. *Engineering Analysis with Boundary Elements*, vol. 101, p. 310-317, **DOI:10.1016/j.enganabound.2019.01.003**.

[26] DeGarmo, E.P., Black, J.T., Kohser, R.A. (1979). Materials and processes in manufacturing, Macmillan, New York.

Strojniški vestnik - Journal of Mechanical Engineering 68(2022)9, 529-541

DOI:10.5545/sv-jme.2022.15
Original Scientific Paper
Received for review: 2022-01-17
Received revised form: 2022-07-07
Accepted for publication: 2022-08-26

MTPA- and MSM-based Vibration Transfer of 6-DOF Manipulator for Anchor Drilling

Youyu Liu[1,3] – Liteng Ma[1,3] – Siyang Yang[1,3] – Liang Yuan[2] – Bo Chen[1,3]
[1] Key Laboratory of Advanced Perception and Intelligent Control of High-end Equipment, Ministry of Education, China
[2] Technology Department, Wuhu Yongyu Automobile Industry Co., China
[3] School of Mechanical Engineering, Anhui Polytechnic University, China

An anchor drilling for a coal mine support system can liberate an operator from heavy work, but will cause serious vibration, which will be transmitted to the pedestal from the roof bolter along a manipulator. Based on the multi-level transfer path analysis (MTPA) and modal superposition method (MSM), a vibration transfer model for the subsystem composed of the joints of a manipulator with six degrees of freedom (DOF) was established. Moreover, its frequency response function matrix was also built. The 6-DOF excitation of the roof bolter was deduced. The exciting force on the roof bolter transmitted to the pedestal along the 6-DOF manipulator was analysed with a force Jacobian matrix, to identify the external loading on the pedestal. A case in engineering practice shows that the amplitude of each DOF of the pedestal from large to small is as follows: bending vibration (component 1), longitudinal vibration, torsional vibration, bending vibration (component 2), rotational vibration around z-axis, rotational vibration around y-axis. The pedestal is mainly in the form of bending vibration. The theory of vibration transfer along the 6-DOF manipulator for anchor drilling proposed in this article can provide a theoretical foundation for the development of vibration-damping techniques and the design of absorbers.
Keywords: manipulator, multi-level transfer path analysis, modal superposition method, vibration transfer, force Jacobian matrix

Highlights
- *Based on MTPA and MSM, a mathematical model of vibration transfer of a 6-DOF manipulator for anchor drilling is established.*
- *The external loading of the response point of the manipulator pedestal is analysed by using the force Jacobian matrix.*
- *The vibration responses on each DOF of the pedestal and the resonance frequency are obtained.*
- *The case studied in an engineering practice shows that the pedestal is mainly in the form of bending vibration.*

0 INTRODUCTION

Roof bolters are key mechanical equipment for a coal mine supporting system. In the past, drilling was done manually. Working in an area with high concentrations of dust for a long time, workers' physical and mental health will be seriously threatened. At present, the development of a coal mine tunnel support tends to be automatic and intelligent. The manual labour of roof bolters has been gradually replaced by mechanical clamping [1]. An operator can control the roof bolter to drill automatically by human-computer interaction, which can liberate the operator from heavy work, and improve the stability and safety of the coal mine support. Due to the comprehensive excitation of different geotechnical parameters, axial thrust, torque and other factors, there are complex vibrations on drill strings during construction. The main forms include bending vibration, longitudinal vibration, and torsional vibration, which interact with each other to form a nonlinear coupled vibration [2]. The excitation vibration of each degree of freedom (DOF) of the roof bolter is transmitted to the pedestal along a manipulator, which causes the manipulator to vibrate violently, shorten its service life, and then affect the support effect.

Transfer path analysis (TPA) is a tool to study vibration transfer [3] and [4]. There are several methods, such as operational transfer path analysis (OTPA) [5] and [6], global transmissibility direct transmissibility (GTDT) [7] and [8], inverse substructure TPA (ITPA) [9], multi-level transfer path analysis (MTPA) [10] and [11], and so on. Lee and Lee [5] proposed the OTPA method using an emerging deep neural network model, which can successfully predict the path contributions using only operational responses. Yoshida and Tanaka [6] attempted to calculate the vibration mode contribution by modifying OTPA, and then considered the relationship between the principal component and the vibration mode, as well as the associated the principal components with the vibration modes of a test structure. High contributing vibration modes to the response point have been found. It is easily disturbed by factors such as excitation coupling and noise employing this method when calculating the transfer matrix. Wang [7] developed further the prediction capabilities of the GTDT method, which can predict a new response using measured variables of an original system, even though operational

*Corr. Author's Address: Anhui Polytechnic University, Wuhu, China, ahpulyy@163.com

forces are unknown. Guasch [8] addressed some issues concerning the prediction capabilities of the GTDT method when blocking transfer paths in a mechanical system and outlined differences with the more standard force TPA. Wang [9] developed the SDD method further by considering the mass effect of resilient links, which can identify decoupled transfer functions accurately, whilst eliminating the mass effect of resilient links. However, its manoeuvrability is poor for a serial system with many substructures. Gao [11] used MTPA to find the critical paths of seat jitter caused by dynamic unbalance excitation of the drive shaft. The key technology of this method is to identify the external excitation loading, which has good operability for series system.

For the vibration problem of pedestal from manipulator caused by the excitation of a roof bolter, a response amplitude matrix in pedestal is established by the modal superposition method (MSM) in this article. According to the excitation of the roof bolter, the external loading of the response point of the manipulator pedestal is analysed using the force Jacobian matrix. The 6-DOF frequency response function of each subsystem of the manipulator is derived by MTPA, and then the frequency response matrix is constructed, which can solve the problem of Transfer path analysis with low accuracy and poor operability. It will provide a theoretical foundation for the development of vibration damping techniques and the design of absorbers.

1 MULTI-LEVEL TRANSFER PATH ANALYSIS

To reduce the influence of non-important factors while analysing the vibration transfer of manipulator for anchor drilling, some simplifications are made as follows. 1) Each linkage of the manipulator is equivalent to a bar with uniform mass; 2) some transfer mechanisms, such as belt driving and harmonic decelerator in the manipulator, are equivalent to linear massless springs; 3) the modal parameters of the manipulator are linear, namely, the output caused by any combined input are equal to the combination of respective outputs; 4) it satisfies the assumption of time-invariance [12], namely, the dynamic properties of the system are not vary with time. According to the above simplifications, a vibration transfer model of the manipulator for anchor drilling is established, as shown in Fig. 1.

This is a multi-input and multi-output system, in which the six joints of the manipulator are connected in series. The vibration source is the roof bolter that provides excitation; the vibration receiver is the pedestal. The manipulator can be divided into six subsystems by the rotating joint. The external loading of the J_6-subsystem is the excitation from the roof bolter; that of other subsystems is the output of the previous subsystem. The output (response point) of the subsystem is the input (exciting point) of the next subsystem. Nevertheless, the output of the J_1-subsystem acts on the pedestal. According to different excitations of spatial degrees of freedom, each subsystem has *m* inputs and *n* outputs.

According to MTPA, the transfer function of manipulator for anchor drilling can be expressed by the product of the transfer functions of all subsystems [11].

$$\mathbf{H} = \mathbf{H}_{J_1} \mathbf{H}_{J_2} \cdots \mathbf{H}_{J_6}. \tag{1}$$

The vibration response of the excitation from the roof bolter transmitted to the pedestal is expressed as follows.

$$\mathbf{S} = \mathbf{HF}. \tag{2}$$

2 MODAL SUPERPOSITION METHOD

2.1 Response Amplitude Matrix

The dynamic equation of the manipulator for anchor drilling is as follows.

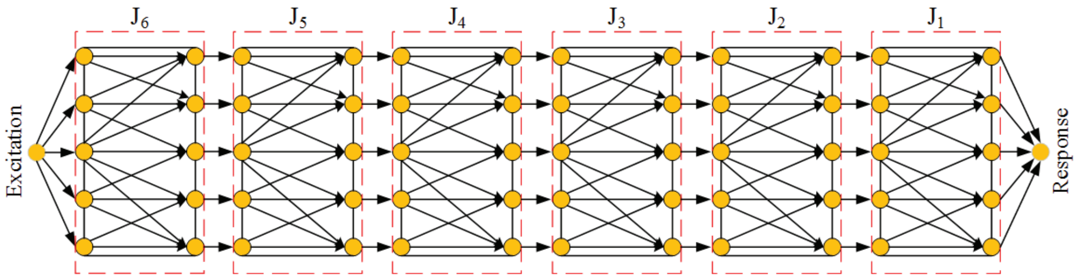

Fig. 1. *Vibration Transfer model of the manipulator*

$$\mathbf{M}\ddot{\mathbf{S}}+\mathbf{C}\dot{\mathbf{S}}+\mathbf{K}\mathbf{S}=\mathbf{F}. \quad (3)$$

According to the linear hypothesis [12], the displacement column vectors of each subsystem of the manipulator can be expressed as the linear addition of each order of modal shapes.

$$\mathbf{S}=\sum_{a=1}^{n} q_a \boldsymbol{\lambda}_a. \quad (4)$$

Substituting Eq. (4) into Eq. (3), then,

$$\mathbf{M}\sum_{a=1}^{n}\ddot{q}_a\boldsymbol{\lambda}_a+\mathbf{C}\sum_{a=1}^{n}\dot{q}_a\boldsymbol{\lambda}_a+\mathbf{K}\sum_{a=1}^{n}q_a\boldsymbol{\lambda}_a=F. \quad (5)$$

Both ends of Eq. (5) are multiplied by $\boldsymbol{\lambda}_b^{\mathrm{T}}$, then,

$$\boldsymbol{\lambda}_b^{\mathrm{T}}\mathbf{M}\left(\sum_{a=1}^{n}\ddot{q}_a\boldsymbol{\lambda}_a\right)+\boldsymbol{\lambda}_b^{\mathrm{T}}\mathbf{C}\left(\sum_{a=1}^{n}\dot{q}_a\boldsymbol{\lambda}_a\right)+\boldsymbol{\lambda}_b^{\mathrm{T}}\mathbf{K}\left(\sum_{a=1}^{n}q_a\boldsymbol{\lambda}_a\right)=\boldsymbol{\lambda}_b^{\mathrm{T}}\mathbf{F}. \quad (6)$$

According to the orthogonality of the main modal shape [13], Eq. (7) can be obtained from Eqs. (5) and (6).

$$\begin{cases}\boldsymbol{\lambda}_b^{\mathrm{T}}\mathbf{M}\boldsymbol{\lambda}_a\\ \boldsymbol{\lambda}_b^{\mathrm{T}}\mathbf{C}\boldsymbol{\lambda}_a\\ \boldsymbol{\lambda}_b^{\mathrm{T}}\mathbf{K}\boldsymbol{\lambda}_a\end{cases}=\begin{cases}M_a,\, a=b\\ C_a,\, a=b\\ K_a,\, a=b\\ 0,\, a\neq b\end{cases}. \quad (7)$$

Substituting Eq. (7) into Eq. (6), then,

$$M_a\ddot{q}_a+C_a\dot{q}_a+K_a q_a=\boldsymbol{\lambda}_a^{\mathrm{T}}\mathbf{F}=\boldsymbol{\lambda}_b^{\mathrm{T}}\mathbf{F}. \quad (8)$$

The excitation loading and displacement response in Eq. (8) are expressed in complex form as follows.

$$\begin{cases}\mathbf{F}=\mathbf{f}e^{j\omega t}\\ q_a=Q_a e^{j\omega t}\end{cases}. \quad (9)$$

Substituting Eq. (9) into Eq. (8),

$$Q_a=\frac{\boldsymbol{\lambda}_a^{\mathrm{T}}\mathbf{f}}{-\omega^2 M_a+j\omega C_a+K_a}. \quad (10)$$

Substituting Eqs. (10) and (9) into Eq. (4), $\mathbf{S}^{\mathrm{T}}$ can be obtained as Eq. (11).

$$\mathbf{S}^{\mathrm{T}}=\sum_{a=1}^{n}\frac{\boldsymbol{\lambda}_a^{\mathrm{T}}\mathbf{f}e^{j\omega t}\boldsymbol{\lambda}_a}{-\omega^2 M_a+j\omega C_a+K_a}. \quad (11)$$

It is assumed that the system has two points: o and p, substitute Eqs. (11) and (9) into Eq. (4), the response amplitude of the point p can be expressed as follows.

$$S_p=\sum_{a=1}^{n}\frac{\lambda_{oa}F_o\lambda_{pa}}{K_a\left[2j\xi_a\left(\frac{M_a\omega\sqrt{K_a/M_a}}{K_a}\right)-\frac{\omega^2 M_a}{K_a}+1\right]}. \quad (12)$$

Their frequency response function (FRF) is as Eq. (13).

$$H_{po}=\frac{S_p}{F_o}=\sum_{a=1}^{n}\frac{\lambda_{oa}\lambda_{pa}}{K_a\left[2j\xi_a\left(\frac{M_a\omega\sqrt{K_a/M_a}}{K_a}\right)-\frac{\omega^2 M_a}{K_a}+1\right]}. \quad (13)$$

According to the linear superposition assumption [12], when $\mathbf{F}=\begin{bmatrix}F_1 & F_2 & \cdots & F_N\end{bmatrix}^{\mathrm{T}}$, the response amplitude of each point of the system is as Eq. (14).

$$\mathbf{S}=\begin{bmatrix}S_1\\ S_2\\ \vdots\\ S_N\end{bmatrix}=\begin{bmatrix}H_{11} & H_{12} & \cdots & H_{1N}\\ H_{21} & H_{22} & \cdots & H_{2N}\\ \vdots & \vdots & \ddots & \vdots\\ H_{N1} & H_{N2} & \cdots & H_{NN}\end{bmatrix}\begin{bmatrix}F_1\\ F_2\\ \vdots\\ F_N\end{bmatrix}. \quad (14)$$

2.2 Parameter Identification

Since the excitation of the roof bolter includes all DOF in space, and each subsystem has $m(6)$ inputs and $n(6)$ outputs, the frequency response of each subsystem of the manipulator is a 6×6$^{\mathrm{th}}$ order matrix, as follows.

$$\mathbf{H}_{\mathrm{J}_i}=\begin{bmatrix}H_{11}(\mathrm{J}_i) & H_{12}(\mathrm{J}_i) & \cdots & H_{16}(\mathrm{J}_i)\\ H_{21}(\mathrm{J}_i) & H_{22}(\mathrm{J}_i) & \cdots & H_{26}(\mathrm{J}_i)\\ \vdots & \vdots & \ddots & \vdots\\ H_{61}(\mathrm{J}_i) & H_{62}(\mathrm{J}_i) & \cdots & H_{66}(\mathrm{J}_i)\end{bmatrix}. \quad (15)$$

The parameters of the J_1 to J_6 frequency response curves are identified in the frequency domain [14] by the rational polynomial method [15]. Its mathematical model is a rational formula of frequency response function, as follows.

$$H_{\mathrm{mn}}(\mathrm{J}_i)=\frac{\alpha_1x^5+\alpha_2x^4+\alpha_3x^3+\alpha_4x^2+\alpha_5x+\alpha_6}{\beta_1x^5+\beta_2x^4+\beta_3x^3+\beta_4x^2+\beta_5x+\beta_6}. \quad (16)$$

3 EXTERNAL EXCITATION LOADING

3.1 Excitation from Roof Bolter

Force and moment on roof bolter: $\mathbf{F}_g$, $\mathbf{F}_a$, $\mathbf{F}_z$, $\mathbf{F}_c$, and $\mathbf{M}_d$. The direction of $\mathbf{F}_g$, $\mathbf{F}_a$ and $\mathbf{F}_z$ is along the shaft of the roof bolter, and their vector expressions is as follows.

$$\begin{cases} \mathbf{F}_g = \begin{bmatrix} F_g & 0 & 0 & 0 & 0 & 0 \end{bmatrix} \\ \mathbf{F}_z = \begin{bmatrix} F_z & 0 & 0 & 0 & 0 & 0 \end{bmatrix} \\ \mathbf{F}_a = \begin{bmatrix} F_a & 0 & 0 & 0 & 0 & 0 \end{bmatrix} \end{cases}. \tag{17}$$

The direction of $\mathbf{M}_d$ is along the shaft of the roof bolter, and its vector expression is as follows.

$$\mathbf{M}_d = \begin{bmatrix} 0 & 0 & 0 & M_d & 0 & 0 \end{bmatrix}. \tag{18}$$

While the lateral displacement of the roof bolter is greater than the distance of them, the roof bolter will collide with rock-soil. The collision force in the z and y axes is as following **[16]**, respectively.

$$\begin{cases} F_{cz} = \begin{cases} -k\left|v(t)\right| - \Omega \operatorname{sgn} v(t) & \left|v(t)\right| \geq \Omega \\ 0 & \text{else} \end{cases} \\ F_{cy} = \begin{cases} -k\left|w(t)\right| - \Omega \operatorname{sgn} w(t) & \left|w(t)\right| \geq \Omega \\ 0 & \text{else} \end{cases} \end{cases}. \tag{19}$$

Eq. (19) is expressed in matrix form as follows.

$$\mathbf{F}_c = \begin{bmatrix} 0 & F_{cz} & F_{cy} & 0 & \dfrac{F_{cz}D}{2} & \dfrac{-F_{cy}D}{2} \end{bmatrix}. \tag{20}$$

The excitation from the roof bolter at the tip of the manipulator is as Eq. (21).

$$\mathbf{F}_\eta = \begin{bmatrix} F_a + F_g - F_z & F_{cz} & F_{cy} & M_d & \dfrac{F_{cz}D}{2} & \dfrac{-F_{cy}D}{2} \end{bmatrix}. \tag{21}$$

3.2 Excitation to Pedestal

Force and torque on pedestal: $\mathbf{F}_{g2}$, $\boldsymbol{\tau}_1$. Each joint of the manipulator can rotate independently. To accurately describe the mechanical properties of the excitation transmitted to the pedestal through the joints of the manipulator, a force Jacobian matrix of the manipulator is introduced **[17]**. The transfer relationship between the excitation and the joint generalized driving force is as follows **[18]**.

$$\boldsymbol{\tau} = \mathbf{J}(q)^{\mathrm{T}} \mathbf{F} \tag{22}$$

The torques of each joint of the manipulator is as follows (Eq. (23)).

$$\boldsymbol{\tau} = \begin{bmatrix} \tau_1 \\ \tau_2 \\ \tau_3 \\ \tau_4 \\ \tau_5 \\ \tau_6 \end{bmatrix} = \begin{bmatrix} J_{1x} & J_{2x} & -d_4\left(c_4c_5c_6 - s_4s_6\right) + a_3\left(s_5c_6\right) & 0 & 0 & 0 \\ J_{1y} & J_{2y} & d_4\left(c_4c_5c_6 + s_4s_6\right) - a_3\left(s_5c_6\right) & 0 & 0 & 0 \\ J_{1z} & J_{2z} & d_4c_4s_5 + a_3c_6 & 0 & 0 & 0 \\ -s_{23}\left(c_4c_5c_6 - s_4s_6\right) - c_{23}s_5c_6 & -s_4c_5c_6 - c_4s_6 & -s_4c_5c_6 - c_4s_6 & s_5c_6 & -s_6 & 0 \\ s_{23}\left(c_4c_5c_6 - s_4s_6\right) + c_{23}s_5c_6 & s_4c_5s_6 - c_4c_6 & s_4c_5c_6 - c_4c_6 & -s_5s_6 & -c_6 & 0 \\ s_{23}c_4s_5 - c_{23}c_5 & s_4s_5 & s_4s_5 & c_5 & 0 & 1 \end{bmatrix} \begin{bmatrix} F_x \\ F_y \\ F_z \\ M_x \\ M_y \\ M_z \end{bmatrix}, \tag{23}$$

where $J_{1x} = -d_2\left[c_{23}\left(c_4c_5c_6 - s_4s_6\right) - s_{23}s_5c_6\right] - \left(a_2c_2 + a_3c_{23} - d_4s_{23}\right)\left(s_4c_5c_6 + c_4s_6\right)$; $c_i = \cos(\theta_i)$; $s_i = \sin(\theta_i)$;

$J_{1y} = -d_2\left[-c_{23}\left(c_4c_5c_6 + s_4s_6\right) + s_{23}s_5c_6\right] + \left(a_2c_2 + a_3c_{23} - d_4s_{23}\right)\left(s_4c_5c_6 - c_4s_6\right)$; $s_{23} = \sin(\theta_2 + \theta_3)$;

$c_{23} = \cos(\theta_2 + \theta_3)$; $J_{1z} = d_2\left(c_{23}c_4s_5 + s_{23}c_5\right) + \left(a_2c_2 + a_3c_{23} - d_4s_{23}\right)\left(s_4s_5\right)$;

$J_{2x} = a_3s_5c_6 - d_4\left(c_4c_5c_6 - s_4s_6\right) + a_2\left[s_3\left(c_4c_5c_6 - s_4s_6\right) + c_3s_5c_6\right]$;

$J_{2y} = -a_3s_5c_6 - d_4\left(-c_4c_5c_6 - s_4s_6\right) + a_2\left[s_3\left(-c_4c_5c_6 - s_4s_6\right) + c_3s_5c_6\right]$; $J_{2z} = a_3c_6 + d_4c_4s_5 + a_2\left(-s_3c_4s_5 + c_3c_6\right)$;

$F_x = F\sin\gamma\cos\varphi$; $F_y = F\sin\gamma\cos\varphi$; $F_z = F\cos\gamma$.

4 CASE IN ENGINEERING PRACTICE

4.1 Essential Parameters

A 6-DOF manipulator for anchor drilling in a coal mine in Huainan, China, is taken as the research object. The size of the two-wing drill adopted is ϕ32 mm; the length of drill string is 86 mm. The drilling object is sandstone, and its mechanical parameters [19] are as follows: ρ = 2600 kg/m^3; R = 38 MPa; R_m = 0.34 MPa; E = 12 GPa; μ = 0.25; F_a = 6000 N; M_d =130 N; Ω = 0 mm; $k = 10^9$ N·m^{-1}; self-weight of the roof bolter is 40 kg; self-weight of the manipulator is 550 kg. Moreover, the parameters of the linkages of the manipulator are shown in Table 1 [20].

The three-dimensional model of the manipulator is shown in Fig. 2. Some finite element models of the manipulator are established, as shown in Fig. 3. The rotating joints of the manipulator are divided into some subsystems, and its exciting points and response points are determined.

Based on MTPA and MSM, the computation flow chart of the vibration transfer of 6-DOF manipulator for anchor drilling is shown Fig. 4.

Table 1. *Parameters of the linkages of the manipulator*

Linkages	Angle variable	a_{i-1} [m]	d_i [m]	Angle range [rad]
1		0	0.56	–3.14 to 3.14
2		0.90	0	–2.27 to 1.22
3		0.16	0	–1.40 to 3.05
4		0	1.01	–6.28 to 6.28
5		0	0	–2.09 to 2.09
6		0	0.2	–6.28 to 6.28

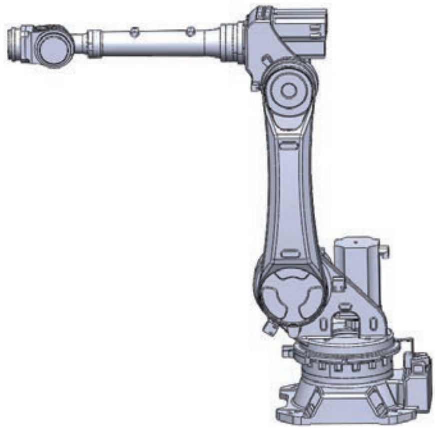

Fig. 2. *The three-dimensional model of the manipulator*

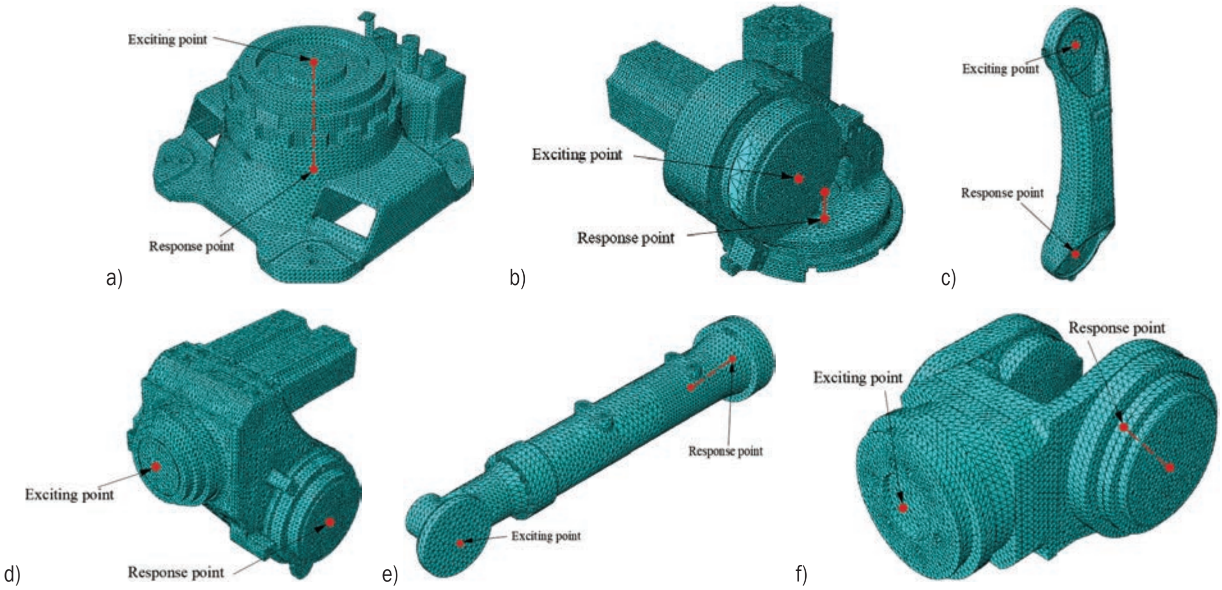

Fig. 3. *Grid division of subsystems and exciting points, response points; a)* J_1*, b)* J_2*, c)* J_3*, d)* J_4*, e)* J_5*, f)* J_6

4.2 Frequency Response Curves

The excitation of the roof bolter is high-frequency vibration; the frequency range in practice is 0 Hz to 200 Hz [21]. Substituting Eqs. (19) and (21) into Eq. (13), the frequency responses of subsystems are analysed using ABAQUS [22]. The acceleration frequency response curves of J_1 to J_6 are shown in Figs. 5 to 10.

According to Figs. 5 to 10, there are resonance peaks [23] in the frequency response curves of each subsystem of the manipulator for anchor drilling in the

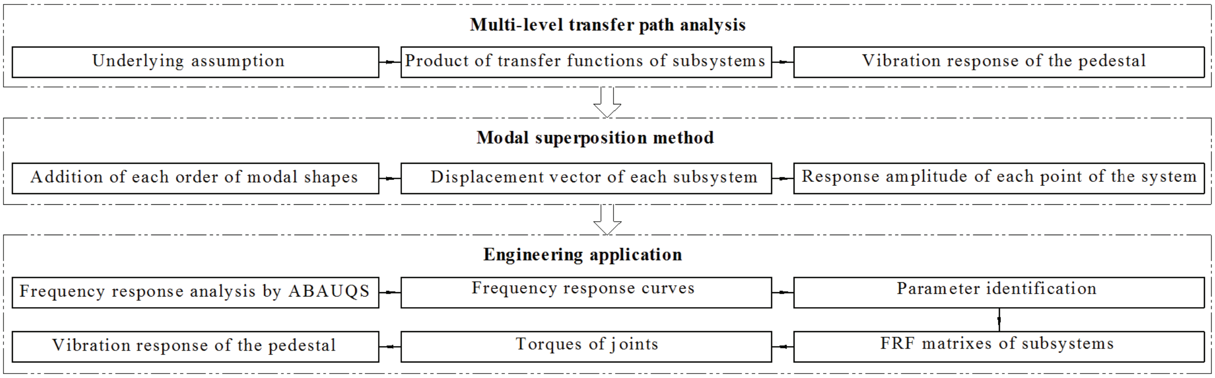

Fig. 4. *Computation flow chart*

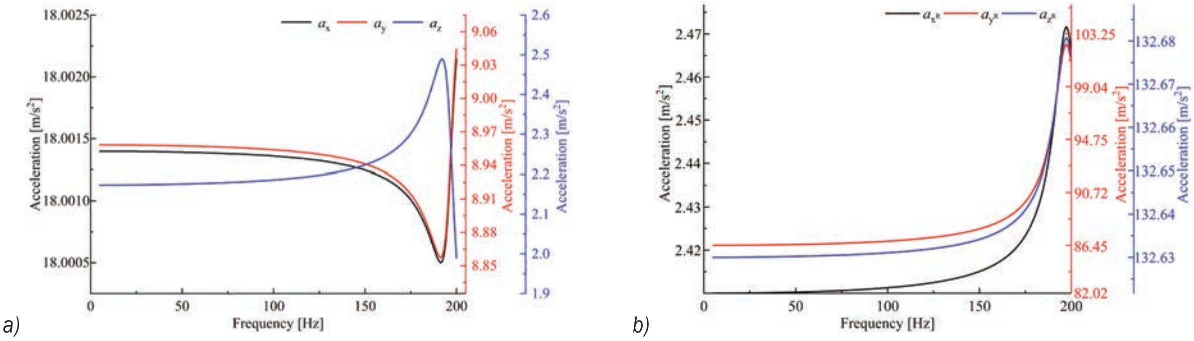

Fig. 5. *Frequency response curves of* J_1 *; a) translational acceleration, and b) rotational acceleration*

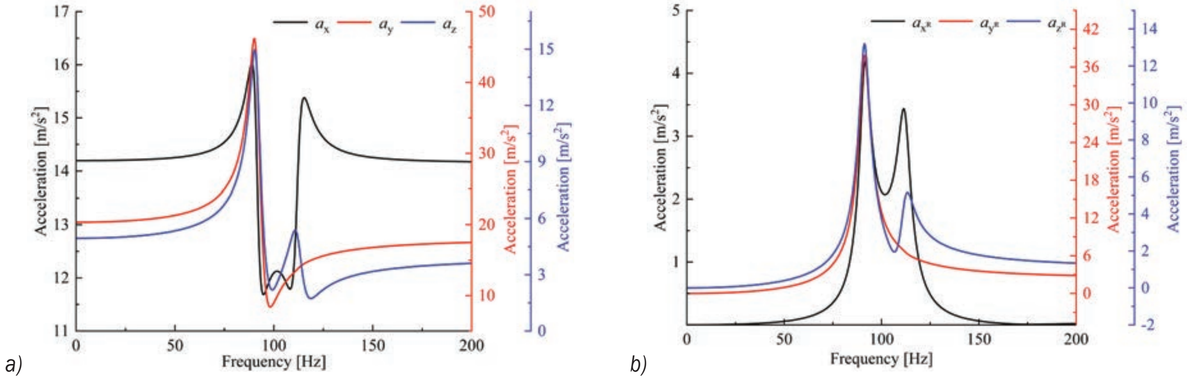

Fig. 6. *Frequency response curves of* J_2*; a) translational acceleration, and b) rotational acceleration*

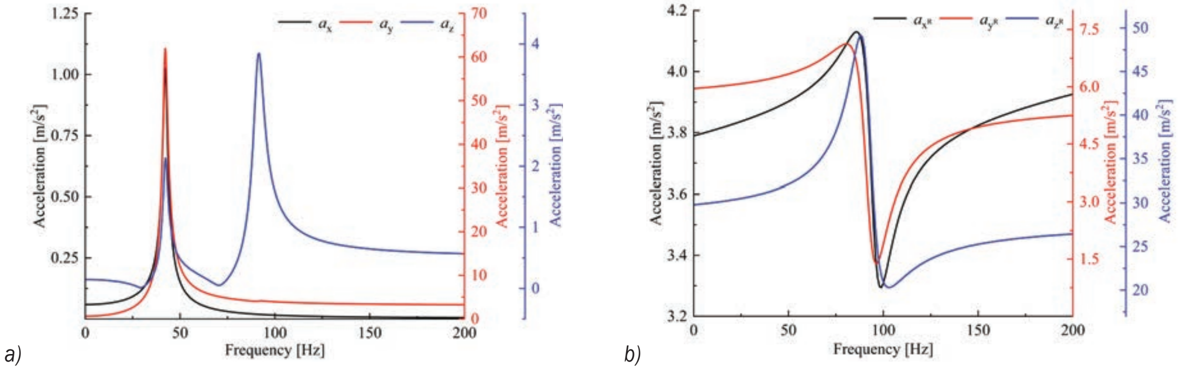

Fig. 7. *Frequency responses curve of* J_3*; a) translational acceleration, and b) rotational acceleration*

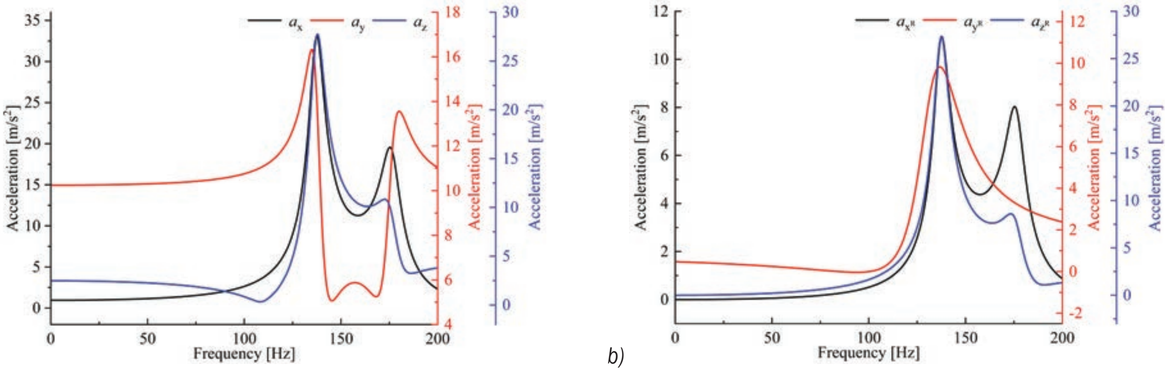

a) b)

Fig. 8. *Frequency response curves of* J_4*; a) translational acceleration, and b) rotational acceleration*

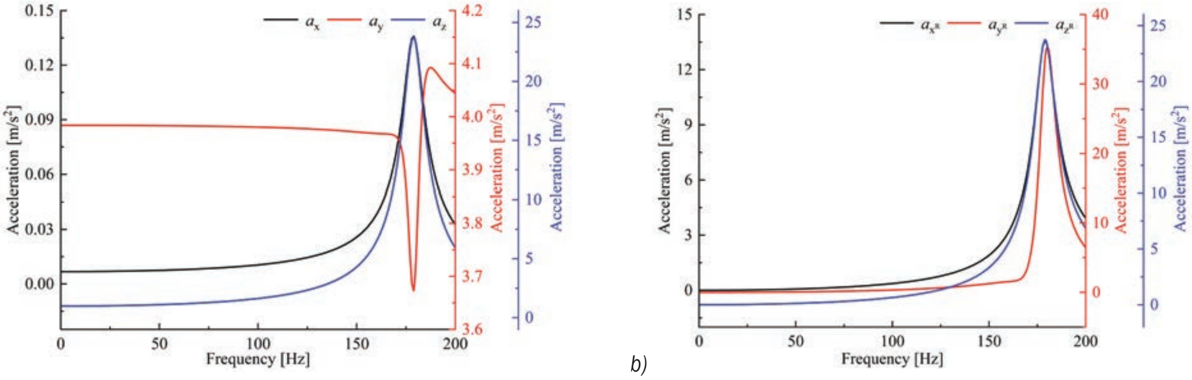

a) b)

Fig. 9. *Frequency response curves of* J_5*; a) translational acceleration, and b) rotational acceleration*

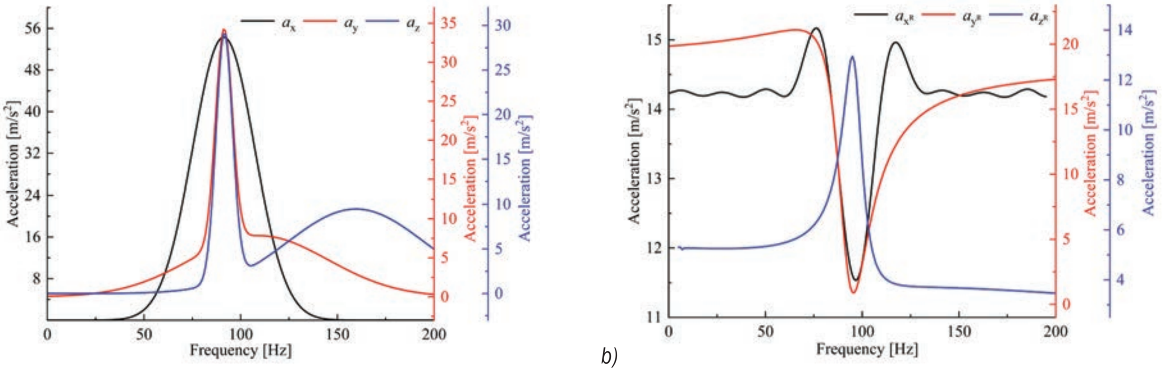

a) b)

Fig. 10. *Frequency response curves of* J_6*; a) translational acceleration, and b) rotational acceleration*

frequency range of 0 Hz to 200 Hz. The frequencies corresponding to the peak values of the 6-DOF frequency response curves is shown in Table 2.

Table 2. *Frequencies corresponding to peak values*

Joints	DOF Frequencies					
	x	y	z	x^R	y^R	z^R
J_1	191.3	191.3	192.2	197.3	197.4	197.2
J_2	88.95	90.32	90.32	91.55	91.34	91.24
J_3	42.19	42.19	91.77	86.2	82.9	88.1
J_4	137.5	135.2	137.9	135.3	137.8	137.8
J_5	178.8	187.4	178.8	187.4	178.7	178.8
J_6	91.27	91.34	91.54	81.66	73.24	95.54

4.3 FRF Matrixes of Subsystems

The frequency response curves of each subsystem are imported into MATLAB, which are fitted according to Eq. (16) with the "Curve Fitting Tool" toolbox [24]. The coefficients of each element in the frequency response matrixes are shown in Tables 3 to 8.

Table 3. *Coefficients of* $H_{mn}(\mathrm{J}_1)$

Coefficients	$H_{11}(\mathrm{J}_1)$	$H_{12}(\mathrm{J}_1)$	$H_{13}(\mathrm{J}_1)$	$H_{14}(\mathrm{J}_1)$	$H_{15}(\mathrm{J}_1)$	$H_{16}(\mathrm{J}_1)$
α_1	1.053×10^{-5}	-2.359×10^{-4}	0	–0.04122	–2.474	–3.082
α_2	18	7.91×10^{-4}	5.53×10^{-4}	9.311	569.6	708.6
α_3	–14.27	8.967	-2.796×10^{-3}	–99.29	–8613	-1.05×10^{4}
α_4	–6.116	–9.886	2.15	–988.8	18.74	–328.7
α_5	3.172	–0.2581	–3.32	–155.4	58.47	7.649
α_6	1.583	2.063	1.303	–22.72	11.5	3.809
β_1	0	0	0	1	1	1
β_2	1	0	0	–398.7	–398.8	–398.8
β_3	–0.793	1	0	3.98×10^{4}	3.983×10^{4}	3.982×10^{4}
β_4	–0.3398	–1.105	1	1979	376.4	1047
β_5	0.1762	-2.802×10^{-2}	–1.519	204.9	–200.2	–50.2
β_6	0.08792	0.2307	0.5861	30.14	–35.51	–10.31

Table 4. Coefficients of $H_{mn}(\mathrm{J}_2)$

Coefficients	$H_{11}(\mathrm{J}_2)$	$H_{12}(\mathrm{J}_2)$	$H_{13}(\mathrm{J}_2)$	$H_{14}(\mathrm{J}_2)$	$H_{15}(\mathrm{J}_2)$	$H_{16}(\mathrm{J}_2)$
α_1	14.37	0	0	0	0	0
α_2	–5269	18.7	1345	0	0.01195	8.488×10^{-3}
α_3	7.419×10^{5}	–4285	-2.042×10^{5}	0	–1.265	–1.264
α_4	-4.749×10^{7}	3.445×10^{5}	2.55×10^{6}	93.75	–30.33	28.8
α_5	1.163×10^{9}	-1.361×10^{7}	4.565×10^{8}	-1.865×10^{4}	5454	1803
α_6	4.135×10^{7}	3.364×10^{8}	-4.691×10^{8}	9.654×10^{5}	-2.66×10^{4}	–9660
β_1	1	0	1	0	0	0
β_2	–367.8	1	26.8	1	0	0
β_3	5.199×10^{4}	–221.8	-1.898×10^{4}	–406	1	1
β_4	-3.341×10^{6}	1.735×10^{4}	-2.815×10^{5}	6.166×10^{4}	–185.9	–185.8
β_5	8.21×10^{7}	-6.762×10^{5}	9.554×10^{7}	-4.15×10^{6}	9099	9093
β_6	3.09×10^{6}	1.654×10^{7}	-9.949×10^{7}	1.045×10^{8}	-4.014×10^{4}	-4.077×10^{4}

Table 5. Coefficients of $H_{mn}(\mathrm{J}_3)$

Coefficients	$H_{11}(\mathrm{J}_3)$	$H_{12}(\mathrm{J}_3)$	$H_{13}(\mathrm{J}_3)$	$H_{14}(\mathrm{J}_3)$	$H_{15}(\mathrm{J}_3)$	$H_{16}(\mathrm{J}_3)$
α_1	1.396×10^{-2}	2.342	0.4121	1.18×10^{-3}	8.639×10^{-7}	0.000374
α_2	–3.895	–276.7	–83.52	3.508	5.586	27.74
α_3	416.3	1.218×10^{4}	5613	–720	–1106	–5552
α_4	-1.863×10^{4}	-2.488×10^{5}	-1.427×10^{5}	3.802×10^{4}	5.885×10^{4}	3.039×10^{5}
α_5	2.958×10^{5}	2.244×10^{6}	1.487×10^{6}	-2.085×10^{5}	-4.029×10^{5}	-2.49×10^{6}
α_6	961	-1.232×10^{6}	–10.48	2.724×10^{5}	1.164×10^{6}	5.792×10^{6}
β_1	1	1	1	0	0	0
β_2	–183.2	–155.3	–242.3	1	1	1
β_3	1.311×10^{4}	9218	2.06×10^{4}	–194.5	–191.7	–193.6
β_4	-4.286×10^{5}	-2.496×10^{5}	-7.338×10^{5}	1.006×10^{4}	9927	1.028×10^{4}
β_5	5.332×10^{6}	2.666×10^{6}	1.026×10^{7}	-5.507×10^{4}	-6.78×10^{4}	-8.394×10^{4}
β_6	1.613×10^{4}	-1.849×10^{6}	–74.75	7.189×10^{4}	1.955×10^{5}	1.951×10^{5}

4.4 Torques of Joints

Substituting the data in Table 1 into Eq. (23), the values of τ_1 change with θ_i, γ and ϕ are obtained by MATLAB, as shown in Fig. 11. τ_1 is distributed symmetrically with the change of joint angle of the manipulator. When θ_2 is at the ultimate angle of –2.27 rad and θ_4 is at that of –6.28 rad, τ_1 is only –2209 N·m as θ_1 and θ_3 change. While $\theta_3 \in$ (–1.24 ~ 1.13) rad, τ_1 shows a trend of decay, when $\theta_3 \in$ (1.13 ~

Table 6. *Coefficients of* $H_{mn}(\mathrm{J}_4)$

Coefficients	$H_{11}(\mathrm{J}_4)$	$H_{12}(\mathrm{J}_4)$	$H_{13}(\mathrm{J}_4)$	$H_{14}(\mathrm{J}_4)$	$H_{15}(\mathrm{J}_4)$	$H_{16}(\mathrm{J}_4)$
α_1	0	0	0	0	0.9853	–2.179
α_2	1.452	10.87	3.019	1.283	–174.3	1054
α_3	–542.2	–3655	–729.4	15.19	6824	-1.6×10^{5}
α_4	8.655×10^{4}	3.114×10^{5}	4.697×10^{4}	-9.851×10^{4}	8.145×10^{4}	8.051×10^{6}
α_5	-7.894×10^{6}	-6.236×10^{5}	-2.925×10^{5}	1.105×10^{7}	-6.495×10^{5}	-1.18×10^{7}
α_6	3.419×10^{8}	3.929×10^{4}	3.765×10^{5}	-3.454×10^{4}	6.07×10^{5}	5.426×10^{4}
β_1	0	0	0	1	1	1
β_2	1	1	1	–624.9	–256.5	–627.4
β_3	–538.6	–341.5	–277.6	1.458×10^{5}	1.548×10^{4}	1.606×10^{5}
β_4	1.113×10^{5}	2.958×10^{4}	2.022×10^{4}	-1.506×10^{7}	1.606×10^{5}	-1.892×10^{7}
β_5	-1.044×10^{7}	-5.924×10^{4}	-1.247×10^{5}	5.81×10^{8}	-1.351×10^{6}	8.4×10^{8}
β_6	3.746×10^{8}	3828	1.529×10^{5}	-1.813×10^{6}	1.274×10^{6}	-3.868×10^{6}

Table 7. *Coefficients of* $H_{mn}(\mathrm{J}_5)$

Coefficients	$H_{11}(\mathrm{J}_5)$	$H_{12}(\mathrm{J}_5)$	$H_{13}(\mathrm{J}_5)$	$H_{14}(\mathrm{J}_5)$	$H_{15}(\mathrm{J}_5)$	$H_{16}(\mathrm{J}_5)$
α_1	0	0	0	2.245	9.23×10^{-3}	0.0141
α_2	1.223×10^{-2}	4.005	12.8	–661.9	–3.182	–5.048
α_3	–4.295	–1464	–3564	3.512×10^{4}	312.4	481
α_4	388.1	1.366×10^{5}	6.619×10^{4}	2.645×10^{6}	–6312	–3513
α_5	–31.56	-4.933×10^{5}	3.108×10^{7}	-8.582×10^{6}	5.686×10^{4}	-3.849×10^{4}
α_6	46.17	3.554×10^{5}	-2.391×10^{7}	2.1×10^{6}	436	1.514×10^{5}
β_1	0	0	0	1	0	0
β_2	1	1	1	–23.44	1	1
β_3	–346.4	–366.1	696.9	-8.757×10^{4}	–364.4	–369.2
β_4	2.834×10^{4}	3.423×10^{4}	-3.441×10^{5}	1.099×10^{7}	3.424×10^{4}	3.642×10^{4}
β_5	3.039×10^{5}	-1.237×10^{5}	3.376×10^{7}	-4.608×10^{7}	-1.834×10^{5}	-4.209×10^{5}
β_6	6662	8.921×10^{4}	-2.461×10^{7}	4.1×10^{7}	-3.878×10^{4}	1.139×10^{6}

Table 8. *Coefficients of* $H_{mn}(\mathrm{J}_6)$

Coefficients	$H_{11}(\mathrm{J}_6)$	$H_{12}(\mathrm{J}_6)$	$H_{13}(\mathrm{J}_6)$	$H_{14}(\mathrm{J}_6)$	$H_{15}(\mathrm{J}_6)$	$H_{16}(\mathrm{J}_6)$
α_1	2.102×10^{-3}	–3.807	0.06361	-7.357×10^{-6}	-1.485×10^{-5}	4.141
α_2	–0.1981	1476	–14.32	3.304×10^{-3}	18.62	–834.1
α_3	–153.7	-1.796×10^{5}	1087	13.72	–3857	4.244×10^{4}
α_4	2.772×10^{4}	7.604×10^{6}	-3.055×10^{4}	–2855	2.287×10^{5}	7347
α_5	-1.185×10^{6}	-5.151×10^{7}	2.653×10^{5}	1.522×10^{5}	-2.966×10^{6}	–450.4
α_6	1.48×10^{7}	4.774×10^{7}	-4.187×10^{5}	-5.962×10^{5}	8.696×10^{6}	–211.3
β_1	0	1	0	0	0	1
β_2	1	–413.3	1	0	1	–195.1
β_3	–354.4	6.999×10^{4}	–162.5	1	–200.1	9678
β_4	4.741×10^{4}	-5.504×10^{6}	4823	–202.7	1.16×10^{4}	-1.156×10^{4}
β_5	-2.837×10^{6}	1.66×10^{8}	1.585×10^{5}	1.072×10^{4}	-1.497×10^{5}	5793
β_6	6.444×10^{7}	-1.577×10^{8}	-3.222×10^{5}	-4.198×10^{4}	4.382×10^{5}	1667

2.30) rad, τ_1 shows a steady trend; and $\theta_3 \in (2.30 \sim 3.04)$ rad, τ_1 showed a slight upward trend. When θ_6 is at the ultimate angle of –6.28 rad, τ_1 is distributed symmetrically with the change of θ_5; and $\tau_{1\,\max}=6018$ N·m. As γ and φ change, τ_1 is symmetrically distributed obviously; and $\tau_{1\,\max}=9117$ N·m. The maximum of τ_1 applied to the pedestal is 9117 N·m, which is transmitted along the 6-DOF manipulator with any position and posture in space.

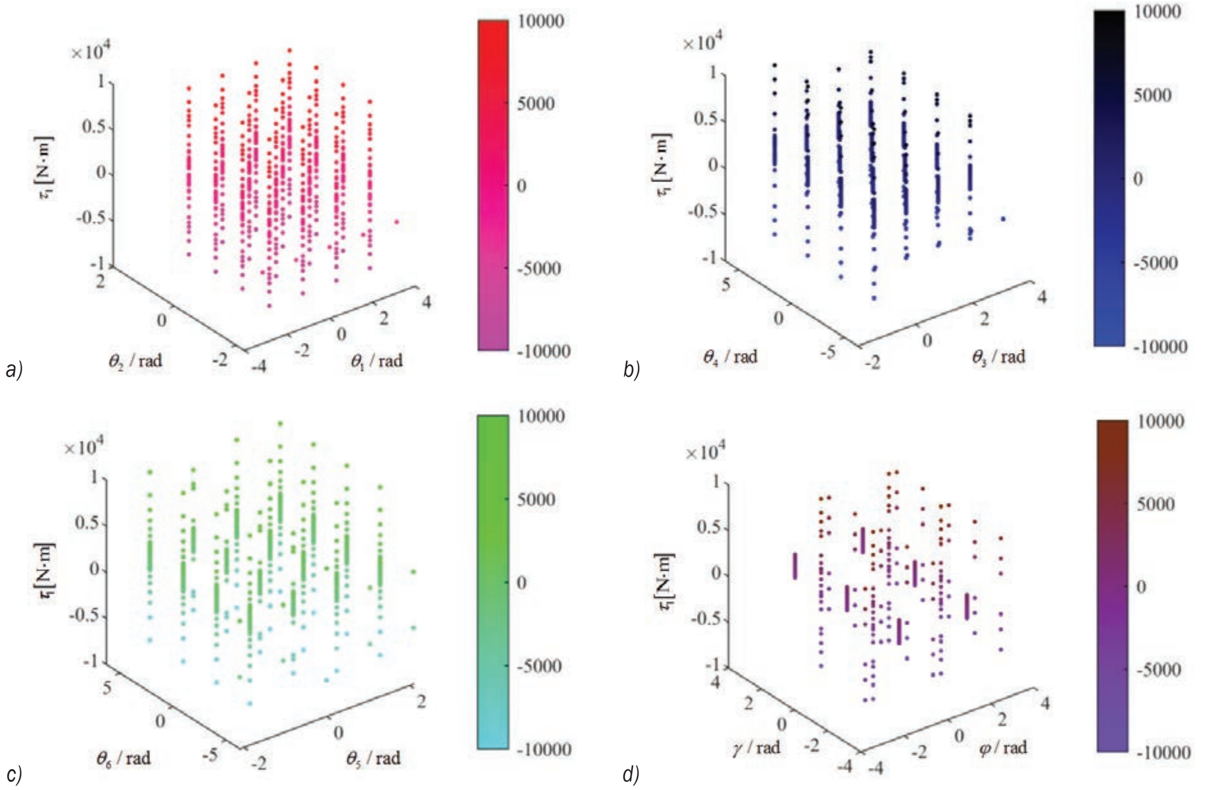

Fig. 11. *τ_1 changes with θ_i (i =1 to 6), γ and φ;*
a) τ_1 change with θ_1, θ_2, b) τ_1 change with θ_3 θ_4, c) τ_1 change with θ_5, θ_6, d) τ_1 change with γ, φ

4.5 Vibration Response of the Pedestal

Substituting the frequency response matrix of each subsystem into Eq. (1) and substituting Eqs. (1) and (24) into Eq. (2), the vibration responses on each DOF of the pedestal are shown in Fig. 12, in which the positive and negative values of the vibration response only represent the direction.

As shown in Fig. 12a, the response of the longitudinal vibration (S_x) of the pedestal reaches the maximum, being 1.65×10^{-2} m, when the frequency is 45 Hz. While the frequencies are 90 Hz and 180 Hz, the responses of the two components (S_y and S_z) of the bending vibration of the pedestal reach the maximum, being 2.12×10^{-2} m and 8.06×10^{-3} m, respectively. At this time, the frequencies corresponding to the peaks are integer multiples of each other, so the phenomenon of resonance will happen.

As shown in Fig. 12b, the response of the torsional vibration (S_{x^R}) of the pedestal reaches the maximum, being 9×10^{-3} m, when the frequency is 190 Hz. The two components (S_{y^R} and S_{z^R}) of rotational vibration

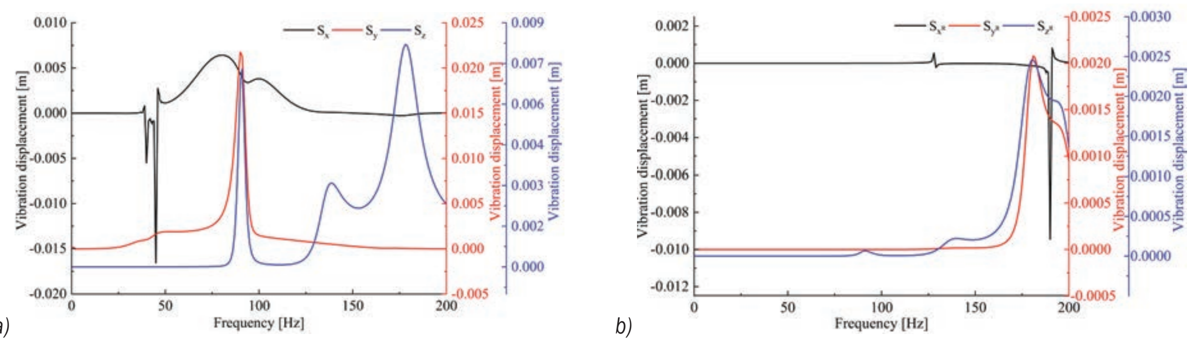

Fig. 12. *Vibration responses on each DOF of the pedestal; a) vibration responses of S_x, S_y, S_z, and b) vibration responses of S_{x^R}, S_{y^R}, S_{z^R}*

around y and z axes sharply increase in the frequency interval [166-181] Hz and [151-180] Hz, and reach the maximum, being 2.08×10^{-4} m and 2.46×10^{-4} m respectively, at the frequencies of 180 Hz and 181 Hz. At this time, the frequencies corresponding to the peaks are very similar, which is easy to induce a resonance. The amplitude of each DOF of the pedestal is from large to small is as follows: bending vibration (component 1) S_y, longitudinal vibration S_x, torsional vibration S_{x^R}, bending vibration (component 2) S_z, rotational vibration around z-axis S_{z^R}, rotational vibration around y-axis S_{y^R}.

5 CONCLUSIONS

(1) Based on MTPA and MSM, a mathematical model of vibration transfer of 6-DOF manipulator for anchor drilling is established. The frequency response matrix of subsystems is derived under multi-DOF excitations. When the external excitation loading is determined, the frequency response function of each DOF at the response point can be calculated by the mathematical model, which is universal for series systems.

(2) Within the frequency range (0 Hz to 200 Hz) of the excitation of the roof bolter, the corresponding frequency ranges of the peak values in the 6-DOF vibration direction of each subsystem are [191.3, 197.4] Hz, [88.95, 91.55] Hz, [42.19, 91.77] Hz, [135.2, 137.8] Hz, [178.8, 187.4] Hz and [73.24, 95.54] Hz, respectively. In the above frequency ranges, the vibration response will be the largest, and the resonance can be avoided by changing the excitation frequency of the roof bolter.

(3) A case in engineering practice shows that the amplitude of each DOF of the pedestal is from large to small is as follows: bending vibration (component 1) S_y (2.12×10^{-2} m) at 90 Hz, longitudinal vibration S_x (1.65×10^{-2} m) at 45 Hz, torsional vibration S_{x^R} (9×10^{-3} m) at 190 Hz, bending vibration (component 2) S_z (8.06×10^{-3} m) at 180 Hz, rotational vibration around z-axis S_{z^R} (2.46×10^{-4} m) at 180 Hz, rotational vibration around y-axis S_{y^R} (2.08×10^{-4} m) at 180 Hz. Obviously, the pedestal is mainly in the form of bending vibration.

(4) The case also shows that a resonance will occur among the two components of the bending vibration at the frequencies of 90 Hz and 180 Hz; a resonance among the two components of rotational vibration around the y and z axes is highly likely to occur at the frequencies of 180 Hz and 181 Hz.

The theory of vibration Transfer along the 6-DOF manipulator for anchor drilling proposed in this article can provide a theoretical foundation for the development of vibration damping techniques and the design of absorbers.

6 NOMENCLATURES

$\boldsymbol{\lambda}_a$	the ath order modal shape
$\boldsymbol{\lambda}_b^{\mathrm{T}}$	the bth order modal shape
λ_{oa}	modal shape of the oth DOF of the ath modal vector
λ_{pa}	modal shape of the pth DOF of the ath modal vector
q_a	modal participation factors
o	exciting point
p	response point
n	modal order
M_a	modal mass coefficient
C_a	modal damping coefficient
K_a	modal stiffness coefficient
$\mathbf{M}$	mass matrix
$\mathbf{C}$	damping matrix
$\mathbf{K}$	stiffness matrix
$\mathbf{S}$	vibration displacement
$\dot{\mathbf{S}}$	vibration speed
$\ddot{\mathbf{S}}$	vibration acceleration
$\mathbf{J}(q)^{\mathrm{T}}$	force Jacobian matrix
J	joint
J	elements in Jacobian matrix
d_i	distance between two adjacent linkages along the common axis [m]
a_{i-1}	common perpendicular length between joint i–1 and joint i [m]
z	moving DOF of z-axis
x	moving DOF of x-axis
y	moving DOF of y-axis
z^R	rotational DOF of z-axis
x^R	rotational DOF of x-axis
y^R	rotational DOF of y-axis
S_y	bending vibration (component 1) [m]
S_x	longitudinal vibration [m]
S_z	bending vibration (component 2) [m]
S_{x^R}	rotational vibration around x-axis (torsional vibration) [m]
S_{y^R}	rotational vibration around y-axis [m]
S_{z^R}	rotational vibration around z-axis [m]
$\mathbf{F}$	external loading [N]
F_y	force projected on the y-axis [N]
F_o	loading at o point [N]
F_{J_i}	excitation force transmitted to joints [N]
F_z	force projected on the z-axis [N]
F_x	force projected on the x-axis [N]

$\mathbf{F}_{g2}$ gravity of manipulator [N]
$\mathbf{F}_g$ gravity [N]
$\mathbf{F}_a$ axial thrust [N]
$\mathbf{F}_z$ disturbing force [N]
$\mathbf{F}_c$ impact force [N]
$\mathbf{M}_d$ torque
M_x torque projected on the x-axis [Nm]
M_y torque projected on the y-axis [Nm]
M_y torque projected on the z-axis [Nm]
v bending vibration displacement (component 2) [m]
w bending vibration displacement (component 1) [m]
μ Poisson's ratio
D outer diameter of drill string [m]
ρ material density [$kg \cdot m^{-3}$]
R compressive strength [MPa]
R_m tensile strength [MPa]
E elastic modulus [GPa]
k elastic coefficient of impact force [$N \cdot m^{-1}$]
γ angle between force and z-axis [rad]
φ angle between force and x-axis [rad]
θ_i joint angle [rad]
Ω clearance between drill string and rock-soil [mm]
ξ_a damping ratio
$\boldsymbol{\tau}$ torque matrix
$\boldsymbol{\tau}_1$ torque from the J_1-axis
α_i molecular coefficients, $i = 1$ to 6
β_i denominator coefficients, $i = 1$ to 6

7 ACKNOWLEDGEMENTS

This work was supported in part by Special Fund for Collaborative Innovation of Anhui Polytechnic University & Jiujiang District under Grant No. 2021CYXTB3, and by and by Natural Science Research Project of Higher Education of Anhui Province of China under Grant No. KJ2020A0357.

8 REFERENCES

[1] Kang, Y.S., Liu, Q.S., Xi, H.L., Gong, G.Q. (2018). Improved compound support system for coal mine tunnels in densely faulted zones: A case study of China's Huainan coal field. *Engineering Geology*, vol. 240, p. 10-20, **DOI:10.1016/j.enggeo.2018.04.006**.

[2] Liu, C.C., Zheng, X.G., Arif, A., Xu, M.B. (2020). Measurement and analysis of penetration rate and vibration on a roof bolter for identification rock interface of roadway roof. *Energy Sources, Part A: Recovery, Utilization, and Environmental Effects*, vol. 42, no. 22, p. 2751-2763, **DOI:10.1080/15567036.2019.1618987**.

[3] Shu, J.C., He E.M. (2020). Review on vibration transfer path analysis methods in frequency domain. *Mechanical Science and Technology for Aerospace Engineering*, vol. 39, no. 11, p. 1647-1655, **DOI:10.13433/j.cnki.1003-8728.20200270**.

[4] van der Seijs, M. V., de Klerk, D., Rixen, D.J. (2016). General framework for transfer path analysis: History, theory and classification of techniques. *Mechanical Systems and Signal Processing*, vol. 68-69, p. 217-244, **DOI:10.1016/j.ymssp.2015.08.004**.

[5] Lee, D.H., Lee, J.W. (2020). Operational transfer path analysis based on deep neural network: Numerical validation. *Journal of Mechanical Science and Technology*, vol. 34, p. 1023-1033, **DOI:10.1007/s12206-020-0205-5**.

[6] Yoshida, J.J., Tanaka, K.K. (2016). Contribution analysis of vibration mode utilizing operational TPA. *Mechanical Engineering Journal*, vol. 3, no. 1, p. 574-589, **DOI:10.1299/mej.15-00589**.

[7] Wang, Z.W., Zhu, P., Zhao, J.X. (2017). Response prediction techniques and case studies of a path blocking system based on global transmissibility direct transmissibility method. *Journal of Sound and Vibration*, vol. 388, p. 363-388, **DOI:10.1016/j.jsv.2016.10.020**.

[8] Guasch, O. (2009). Direct transfer functions and path blocking in a discrete mechanical system. *Journal of Sound and Vibration*, vol. 321, no. 3-5, p. 854-874, **DOI:10.1016/j.jsv.2008.10.006**.

[9] Wang, Z.W., Peng, Z.K., Liu C., Shi, X. (2019). Virtual decoupling of mechanical systems considering the mass effect of resilient links: Theoretical and numerical studies. *Mechanical Systems and Signal Processing*, vol. 123, p. 443-454, **DOI:10.1016/j.ymssp.2019.01.028**.

[10] Sakhaei, B., Durali, M. (2014). Vibration transfer path analysis and path ranking for NVH optimization of a vehicle interior. *Shock and Vibration*, vol. 2014, art. ID 697450, **DOI:10.1155/2014/697450**.

[11] Gao F., Li Y.O., Zhang J. (2015). The control strategy rseearch and engineering application of seat vibration at high speed of fr vehicle. *Proceedings of the 2015 Annual Meeting of the Chinese Society of Automotive Engineering*, p.192-195.

[12] Shah, V-.N., Bohm, G.J., Nahavandi, A.N. (1979). Modal superposition method for computationally economical nonlinear structural analysis. *Journal of Pressure Vessel Technology*, vol. 101, no. 2, p. 134-141, **DOI:10.1115/1.3454612**.

[13] Fu, Z.F., He, J.M. (2001). *Modal Analysis*. Elsevier, Woburn.

[14] Karaağaçlı T., Özgüven H.N. (2020). A frequency domain nonparametric identification method for nonlinear structures: Describing surface method. *Mechanical Systems and Signal Processing*, vol. 144, art. ID. 106872, **DOI:10.1016/j.ymssp.2020.106872**.

[15] Dong, X.G., Guo, X.Y., Wang, Y.X. (2020). Local polynomial method for frequency response function identification. *Systems Science & Control Engineering*, vol. 8, no. 1, p. 534-540, **DOI:10.1080/21642583.2020.1833784**.

[16] Piovan, M.T., Sampaio, R. (2006). Non linear model for coupled vibrations of drill-strings. *Mecanica Computacional*, p. 1751-1766.

[17] Turkovic, K., Car, M., Orsag, M.(2019). End-effector force estimation method for an unmanned aerial manipulator. *2019 Workshop on Research, Education and Development*

of Unmanned Aerial Systems, p. 96-99, **DOI:10.1109/REDUAS47371.2019.8999670**.

[18] Ding, W.H., Deng, H., Zhang, Y., Ren, Y.Q. (2012). Optimum design of the jaw clamping mechanism of forging manipulators based on force transmissibility. *Applied Mechanics and Materials*, vol. 157-158, p. 737-742, **DOI:10.4028/www.scientific.net/AMM.157-158.737**.

[19] Liu, S.W., Fu, M.X., Zhang, H. (2016). Vibration mechanism and characteristics analysis of drill rod when drilling roof bolt hole. *Journal of China University of Mining & Technology*, vol. 45, no. 5, p. 893-900, **DOI:10.13247/j.cnki.jcumt.000562**.

[20] EFORT (2019). Robot Products, from *https://www.efort.com.cn/product/prodetail/44.html*, accessed on 2019-05-09.

[21] Mendil C., Kidouche M., Doghmane M.Z., Benammar,, S., Tee, K.F. (2021). Rock-bit interaction effects on high-frequency stick-slip vibration severity in rotary drilling systems. *Multidiscipline Modeling in Materials and Structures*, vol. 17, no. 5, p. 1007-1023, **DOI:10.1108/MMMS-10-2020-0256**.

[22] Weeger O., Wever U., Simeon B. (2014). Nonlinear frequency response analysis of structural vibrations. *Computational Mechanics*, vol. 54, p. 1477-1495, **DOI:10.1007/s00466-014-1070-9**.

[23] Li, C.S., Luo, S.H., Ma, W.H. (2013). Vibration isolation performance analysis of a HXN3 diesel locomotive cab based on frequency response functions. *Journal of Vibration and Shock*, vol. 32, no. 19, p. 210-215, **DOI:10.13465/j.cnki.jvs.2013.19.025**.

[24] Grauer, J.A. (2015). An interactive MATLAB program for fitting transfer functions to frequency responses. *AIAA Scitech 2021 Forum*, p, 1-14, **DOI:10.2514/6.2021-1426**.

Strojniški vestnik - Journal of Mechanical Engineering 68(2022)9, 542-551

DOI:10.5545/sv-jme.2022.147
Original Scientific Paper
Received for review: 2022-04-05
Received revised form: 2022-08-02
Accepted for publication: 2022-08-10

Functional Surface Layer Strengthening and Wear Resistance Increasing of a Low Carbon Steel by Electrolytic-Plasma Processing

Kuat Kombayev[1] – Murat Muzdybayev[1] – Alfiya Muzdybayeva[1] –
Dinara Myrzabekova[1] – Wojciech Wieleba[2] – Tadeusz Leśniewski[2,*]

[1] East Kazakhstan State Technical University, Technological Machines and Transport Department, Republic of Kazakhstan
[2] Wrocław University of Science and Technology, Faculty of Mechanical Engineering, Poland

The modified technology for strengthening the surface layer of low-carbon steel for machine components by electroplasma processing is proposed. This technology is to be used as an alternative carburizing method with subsequent hardening. The developed technology of strengthening by the proposed method is based on the author's invention. The parameters of this process are given, resulting in a thickness of the reinforced surface layer of 1000 µm to 1700 µm. An increase in microhardness of 1.5 to 2 times (compared to the initial state) was observed. With hardening, chemical modification of the material's surface layer occurs. The microstructure of the treated surface of the steel samples is characterised by a dark modified surface layer: a fine needle-like structure of martensitic origin under the dark layer transforms into an initial perlite-ferritic structure. The advantage of strengthening based on the electrolytic plasma processing consists of low energy consumption at high hardening speeds and the possibility of local processing of surface areas, especially large parts of complex shapes. In addition, the proposed surface treatment method using electrolytic plasma processing (EPP) not only achieves a smooth surface but also improves the service qualities of the components, specifically wear resistance.

Keywords: low-carbon compound steel, strengthening, electrolytic plasma processing

Highlights

- *The author's technology of strengthening the surface layer of low-carbon compound steel for details of machines by electrolytic plasma processing is developed.*
- *This technology is proposed as an alternative method of carburizing with subsequent hardening; the total thickness of the strengthened surface layer is 1000 µm to 1700 µm, and the microhardness of the strengthened area of a martensitic structure is 6500 MPa to 7200 MPa.*
- *The microstructure of the processed surface of steel samples is characterized by a dark modified surface layer. A fine needle-like structure of martensitic origin under the dark layer changes into the initial pearlite-ferritic structure.*
- *It is stated that in the structure of 18CrNi3Mo-Sh steel sample after electrolytic plasma processing, particles of residual cementite Fe3C, a-phase based on Fe, Cr0.6 Fe1.4 - phase and Fe2.7 Mo0.8 Ni0.1 - phase appear, which confirms availability of martensite hardening.*
- *The advantage of strengthening based on the electrolytic plasma processing consists of low energy consumption at high hardening speeds and the possibility of local processing of surface areas, especially large parts of complex shapes.*

0 INTRODUCTION

Mechanical engineering development is largely related to solving the tasks of increasing machines' reliability. To increase the operational reliability of machines, it is necessary to increase the endurance and durability of their parts [1] and [2] and reduce the risk of their failures [3] and [4]. This is achieved by various methods, including strengthening the operating surfaces of component parts and creating new technological processes of highly wear-resistant materials manufacturing [5] to [7]. Toughening the requirements concerning the microstructure and properties of the surface layers of machines' component parts requires new methods for their modification and strengthening [8]. Techniques involving the influence of concentrated energy flows on the surface of component parts appeared to be widely used [9]. The most promising technology for surface strengthening of component parts is electrolytic plasma processing (EPP) [10]. EPP is an electrochemical heat treatment process and mass transfer (coating) on a component part (product) surface using a plasma jet. A plasma jet is a partially or fully ionized gas in combination with electric discharged phenomena at the boundary of the main electrode-water electrolyte solution at high capacities up to 1000 V [11].

With a gradual increase in the applied constant voltage, salt electrolysis occurs. According to Ohm's law, the current increases (section from 0 to A, Fig. 1). This area is characterized by scaling up the current with voltage increasing. Doing this, the electrolyte temperature also increases. This is a consequence of

*Corr. Author's Address: Wrocław University of Science and Technology, Wybrzeże Wyspiańskiego 27, 50-370 Wrocław, Poland, tadeusz.lesniewski@pwr.edu.pl

the current passing through the electrolyte. When a certain voltage value is reached (from 100 V to 176 V), the electrolyte starts boiling on the surface of the cathode, and an active release of bubbles near the surface occurs (bubble boiling). At bubble boiling, the temperature of the component part is close to the steam point. When bubble boiling occurs around the active electrode, large current pulsations can be observed. Their amplitude is significantly reduced when the component part is heated above 470 °C.

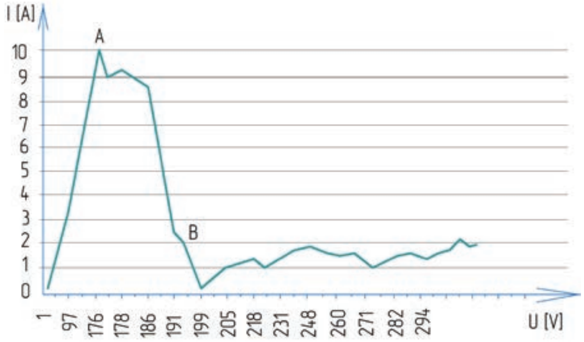

Fig. 1. *Volt-ampere characteristic of electrolyte plasma processing*

Over a further increase in rectified voltage, film boiling appears (point A, Fig. 1), which is characterized by the disappearance of bubble boiling and a sharp drop in current because the resulting gas-steam jacket has a higher electrical resistance than a liquid electrolyte (section from A to B, Fig. 1). Since the gas-steam jacket is less electrically conductive, the main voltage drop occurs precisely where more heat is generated. The low-temperature plasma of a specific blue glow around the component part is formed due to a gas-steam jacket forming an electric current passing through it. The brighter the blue colour of plasma burning, the more ions it contains, including ion modifiers. An abnormal discharge is observed when increasing the voltage [12]. The principle of the technological process of strengthening based on the method of EPP is as follows. The cathode is made of 18CrNi3Mo-Sh steel (which corresponds to the standard 18HN3MA-Ш TU 3-850-80) for manufacturing roller cones. It is immersed in the electrolyte (10 % water solution Na2CO3) to 4 mm to 6 mm depth. The anode is stainless X10 CrNiTi 18-10 (corresponding to the standard 12X18H10T GOST 5949-75 Steel). It is in the form of a disk with a diameter of 50 mm and a thickness of 2 mm; 4 mm holes are drilled in the disk. Plasma arises between the cathode and liquid electrolyte. Negative ions ease excess electrons when passing through the holes of the anode of stainless X10 CrNiTi 18-10 steel. The cations are entrained by the hydrodynamic flow of electrolyte and recombine at the cathode (the surface of the sample material of the drill bit). The conversion of electrical energy into heat occurs mainly in the plasma layer on the heated cathode surface. When being processed, cathode surfaces are cemented with carbon ions and hardened in an electrolyte in a short time.

The modification of the surfaces of machines' component parts with the EPP method contributes to the compositional restructuring of a surface layer that increases strengthening properties and wear resistance due to physical input (ions of high-temperature plasma, electrical discharge). The EPP method is currently used when modifying the surfaces of component parts of bent shafts, iron cylinders of diesel engines, circular saws [13], and others. The main advantages of the EPP method are the following: a complex profile strengthening, internal surfaces and cavities; no need for special preparation of surfaces before strengthening; ecological safety (use of special treatment facilities is not required). Analysis of existing technologies for low-carbon compound steel products hardening suggested that electrolytic plasma strengthening could be the most appropriate technology for the thermal hardening of component parts. The aim of this research is to identify experimentally the values of parameters for the technological process of electrolyte-plasma hardening of 18CrNi3Mo-Sh steel. The article presents the research methodology description, the obtained results, their discussion, conclusions, and acknowledgements.

1 METHODS AND EXPERIMENTAL APPROACH

A multiple-factor experiment has been fully implemented to select optimal electrolyte plasma processing conditions. Experiments of this type can localize the area necessary and present all possible independent variables' values. Heating a sample of a component part in depth is associated with an inhomogeneous temperature distribution in the volume of the material of a component part [14].

A drill bit (Fig. 2) provided by JSC Vostokmashzavod (VKMZ JSC) was selected to study the effectiveness of various methods of strengthening. Contact durability, abrasive and shock-abrasive wear resistance of the drill bit's component parts are provided by gas carburizing followed by hardening. Deformation, low carbon steel cracking, and high labour and energy intensity are the disadvantages of that heat processing. In order to eliminate the disadvantages of the above treatment method, for EPP, the following samples from drill bit's component parts were used: 18CrNi3Mo-Sh (0.16 % to 0.18 % C; 3.3 % Ni; 0.9 % Cr; 0.51 % Mo; 0.44 % Mn; 0.34 % Si; 0.05 % Al; 0.008 % S; 0.012 % P; 0.015 % N; 0.01 % O; 0.01 % H) NSS 4543-71 **[13]**. Low-carbon, compound, heat-resistant steel of electroslag remelting can be used at –70 ºC to +450 ºC. Carbon, chromium, molybdenum, manganese, and silicon are alloying constituents, increasing strengthening properties. Nickel provides strength and good toughness; molybdenum provides heat resistance to steel. Samples of 10 mm × 10 mm × 20 mm were cut out of roller cones with a diamond blade with a thickness of 1 mm, which was immersed in cooling fluid. The samples were made from roller cones in the initial condition and compared after thermal processing on the JSC "VKMZ" base. Two series of samples (3 repetitions in each) hardened according to the method given by JSC "VKMZ" and processed using the EPP method were examined.

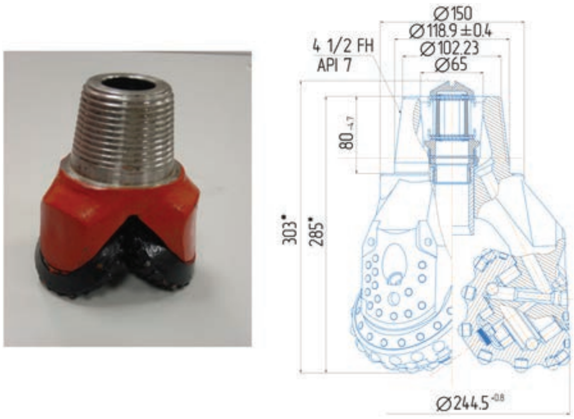

Fig. 2. *Roller cone*

At low cutting speeds (n = 350 rpm) and low load (m = 250 g), the sample does not experience significant deformations and thermal effects. The samples were first polished with chromium dioxide cement and then etched with 5 % alcoholic nitric acid solution to do a metallographic microanalysis.

Application investigations and mechanical testing were carried out in the Regional University Engineering Laboratory Irgetas and the research and manufacturing complex Machine industry of D. Serikbayev East Kazakhstan State Technical University **[15]**. Metallographic analysis was carried out using an Axioscop-2MAT microscope equipped with a Sony digital camera. Qualitative and quantitative phase analysis of the steel samples' structure was carried out using an X'Pert PRO X-ray diffractometer of the PAN analytical firm, applying Cu-Kα radiation. The electron images were made with the following equipment: a raster electron microscope JSM-6390LV "JEOL Ltd." (Japan) with an energy dispersive microanalysis system INCA Energy Penta FET X3 "OXFORD Instruments Analytical Limited". Microhardness measurements were carried out using a PMT-3 device, equipped with a diamond pyramid, with a load on the 2H indenter by 9450-76 GOST. The wear resistance of the samples was estimated by the loss of mass per unit time when the sample was being tested by attrition on the abrasive disc when sliding rubbing without lubricant **[16]**. To measure the mass of the samples, an electronic weighing unit of the VL-120 model with an accuracy of 0.1 mg was used.

2 RESULTS

The influence of technological and electrical parameter changes during electrolyte (10 % water solution of Na_2CO_3 calcined soda) on the strengthening quality was studied. It was experimentally proved that the considered factors of EPP modes affect the quality of the steel surface, which is strengthened. It should be noted that the main technological parameters, such as the thickness of strengthening, microhardness, and wear resistance of steel depend on the heating time, hardening time, the number of strengthening cycles by the EPP method and the electric current voltage **[14]**. Fig. 3 shows the initial microstructure of the material of the sample of a strengthened component part of 18CrNi3Mo-Sh steel. It is seen that a coarse-grained pearlite-ferritic microstructure characterizes the material of the sample.

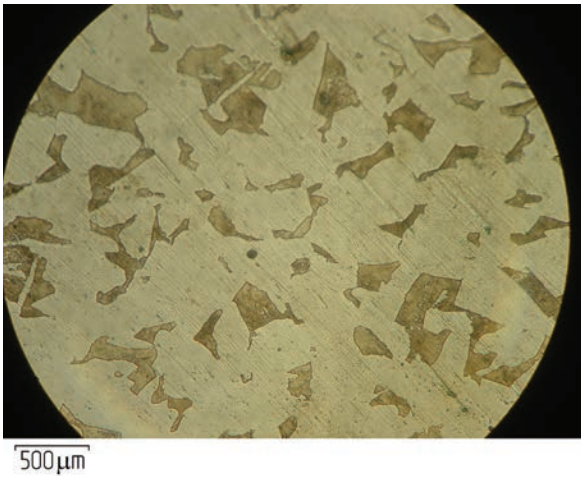

Fig. 3. *The initial structure of the sample material of a component part of 18CrNi3Mo-Sh steel*

In the course of the study, a series of searching experiments were carried out, involving EPP testing for sample processing to identify the logical modes of the process. The ranges of the numerical values of the parameters studied are presented in Table 1.

Table 1. *Technological parameters for hardening of 18CrNi3Mo-Sh steel by the EPP method*

Terms in the program of the experiment	Physical factors	Factor levels	
		min	max
X1	The heating time of a work piece from the plasma temperature [s]	1	15
X2	The hardening time in the flow of electrolyte [s]	1	10
X3	DC voltage [V]	180	260
X4	Number of cycles [-]	20	40

It was decided to switch to a three-factor experiment model and settle the number of processing cycles at 30 to conduct a comparative analysis of technological modes' influence on the material of the component part strengthening. To systematize the assessment of the EPP modes' effect on the quality indicators of steel of drill bits strengthening, depending on such main parameters as heating time T_{heatig} from ionized plasma and hardening time $T_{hard\ in\ g}$ in the electrolyte flow, taking into account the direct current (DC) voltage U between the electrodes, we converted micrographs of material microstructure into a tabular form (Table 2). In one case, the images located along the edges lack the modes for optimal hardening of the material of a sample (left). In another case, the sample matrix burns out (right), transforming the hardening process in EPP into the process of ion transfer of metal from the anode to the strengthened cathode.

Table 2. *EPP modes while steel drill bit strengthening*

Parameters	Modes EPP processing		
	A	B	C
Heating time t_{heatig} [s]	2	4	15
Hardening time $t_{hard\ in\ g}$ [s]	2	4	15
DC voltage U [V]	190	200	250

Fig. 4 shows the microsections of electrolyte-plasma processed steel to the depth of the hardened layer (cross-section). A comparison of microsections (cross-sectional cuts to the deep from left to right), presented in Fig. 4, makes it possible to note the features of the microstructure of the material obtained at different modes of EPP processing: when processing at mode A, the influence of high-temperature plasma is observed (Fig. 4a, the dark area from left to right). The layer of coarse needle-like martensite smoothly transfers into the initial structure as it deepens into the material. When processing at mode B, there is also an area of high-temperature plasma exposure. Its depth is comparatively larger than at mode A and is approximately 200 µm deep (Fig. 4b, dark area from left to right). The availability of fine needle-like martensite with a smooth transition to the initial structure of the sample material is noted.

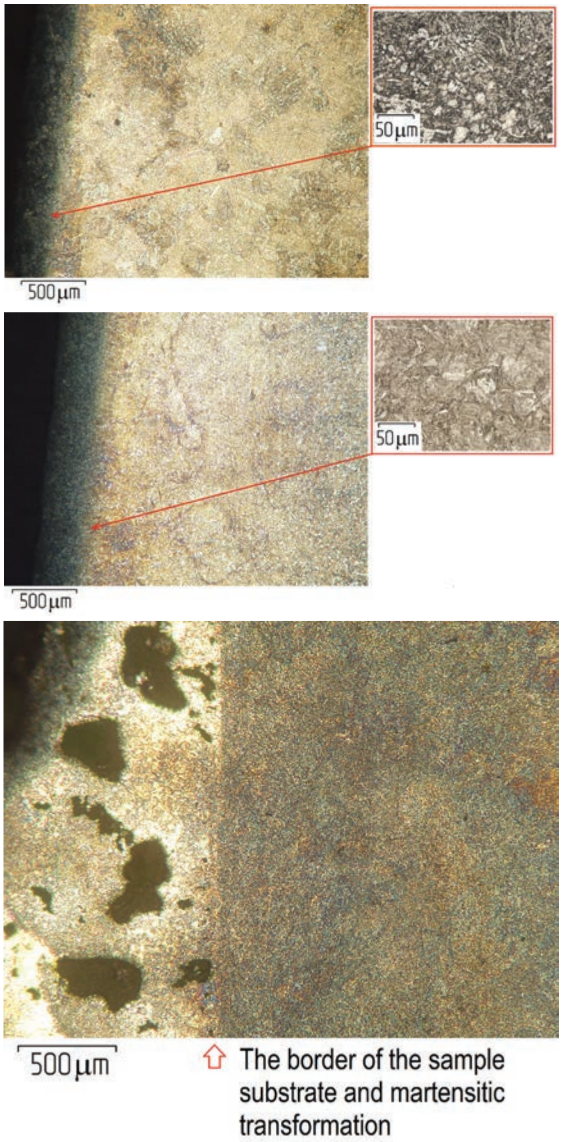

a)
b)
c)

Fig. 4. *Micro sections of the cross-section (to the depth of material) of electrolytic plasma processed steel*

After 15 s of EPP processing (at mode C), a deposited layer of anode material (steel X10 CrNiTi

18-10) on the microsection occurs. The sample substrate's border and martensitic transformation are clearly visible (Fig. 4c, to the depth from left to right). Thus, images of microsections reveal:

- mode A lacks parameter values of EPP processing for the optimal hardening of the sample material (Fig. 4a),
- mode B burns out the material of a sample while EPP processing (Fig. 4b), transforming the hardening process into the process of ion transfer of metal from the anode to the strengthened cathode.

It is stated that electrolyte-plasma processing requires low power (within 3 kWh) when rapid motion occurs. The obtained data are used in [17].

In actual practice, a thermal exchange is a complex process. To facilitate its study and simplify the correlations obtained, the concept of elementary types of thermal exchange is introduced: experimentally determined thermocouples made by a natusral thermal junction. Two thermocouples are installed in two layers of the sample workpiece at a depth of *h1* and *h2* from the heated surface (Fig. 5). Thermocouples are installed to control the temperature mode of the process to prevent the material's melting from being strengthened.

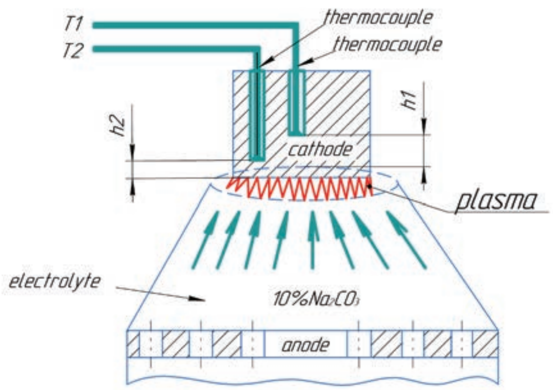

Fig. 5. *The layout of thermal junctions in the surface layer of the sample when measuring the temperature in the process of electrolytic plasma heating*

A 10 mm × 10 mm × 20 mm steel sample acts as a cathode. The temperature is measured by a thermocouple mounted in the cathode body. The thermocouple is a thermoelectric converter of the TXA type, conditional designation XA (K) according to GOST 3044-84. The measurement range is from minus 200 ºC to plus 1000 ºC. Admission class 1. The limits of permissible deviations are ±0,004×T when a measurement is in the range above plus 375 ºC to plus 1350 ºC. The sensitivity of the thermocouple is 40 μV/ºC. The range of measured temperatures corresponds to the temperature of phase transformations from plus 840 ºC to plus 860 ºC.

Heating temperature is the main parameter of phase transformations for 18CrNi3Mo-Sh steel and is 860 °C [18]. At EPP, the bulk temperature increases to the hardening temperature of 860 °C, and the temperature of the ionized plasma overheats the surface. Its temperature exceeds 1100 °C. When ionized plasma is excited (plasma temperature ranging from 6000 K to 30000 K), a gas-vapor layer appears on the sample surface due to electrolyte dissociation [19]. The gas-vapor layer prevents the ingress of electrolyte on the overheated surface. It reduces the cooling rate, eliminating the formation of thermal (hardening) cracks. As a result, the operating durability of steel increases. Thus, the main factors determining the quality of steel strengthening at EPP have been experimentally stated. They are heating time, hardening time, and electric current voltage.

A mathematical model is developed to describe the change in the key parameter of the technological process of steel strengthening at the EPP method: the heating temperature *T*. The following regression equation expresses the logarithmic dependence of the temperature *T* on the main factors:

$$\ln(T) = C \cdot a \cdot \ln(t_{heating}) + D \cdot b \cdot \ln(U) + E \cdot d \cdot \ln(t_{cooling}), \tag{1}$$

where T is steel heating time [s], t_{heatig} heating time [s], t_{coolig} cooling time in the electrolyte flow [s], U voltage [V], and $C = 4.5$, $D = 4.8$, $E = 18$, $a = 2$, $b = 1$, $c = 1$ the coefficients for Eq. (1) were found by using logarithm in the Deductor Studio Academic software.

Then Eq. (1), which describes the dependence of the heating temperature on the heating time, cooling time and voltage, was transformed to Eq. (2):

$$T = 4.5 \cdot t_{heating}^2 + 4.8 \cdot U - 18 \cdot t_{cooling}, \tag{2}$$

where T is steel heating time [s], t_{heatig} heating time [s], t_{coolig} cooling time in the electrolyte flow [s], and U voltage [V] [20].

Experimentally determined optimal modes of steel hardening by the EPP method (t_{heatig} = 4 s, t_{coolig} = 4 s, U = 200 V) have a good correlation with the established dependence, see Eq. (2).

A raster elemental analysis of the processed surface (Fig. 6) revealed chemical modification of the surface layer of the metal happening along with hardening during the electrolytic plasma heating of the sample [21].

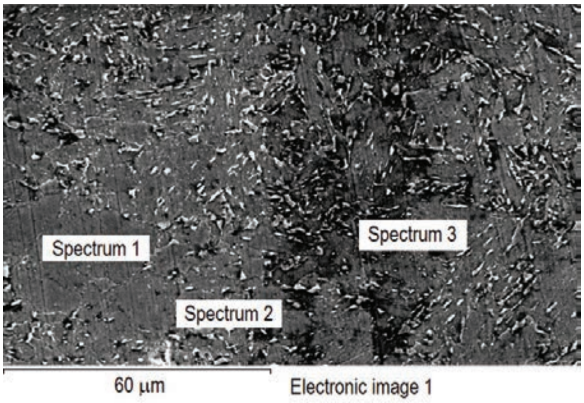

Fig. 6. *Raster elemental analysis of the 18CrNi3Mo-Sh steel surface after EPP strengthening*

Table 3. *Qualitative and quantitative analysis of the sample processed* **[23]**

No. of spectrum	Spectrum 1	Spectrum 2	Spectrum 3
C	0.56	0.69	0.71
Na	–	0.38	–
Si	–	–	0.31
Cr	0.66	0.66	0.54
Mn	0.48	–	0.54
Fe	95.73	95.75	95.48
Ni	2.57	2.52	2.42
Total	100.00	100.00	100.00

Temper increasing (Table 3), relative to the initial state, is because charged carbon ions **[22]**, saturating the surface of the sample, are generated in the plasma layer of electrical gas discharge from the water solution of soda ash Na_2CO_3 when electric current flows. In water solution Na_2CO_3, such ions as $2Na^+$, $CO_3{}^{2-}$, OH^-, H^+ occur. When passing through the holes in the anode, anions ease away excess electrons. The

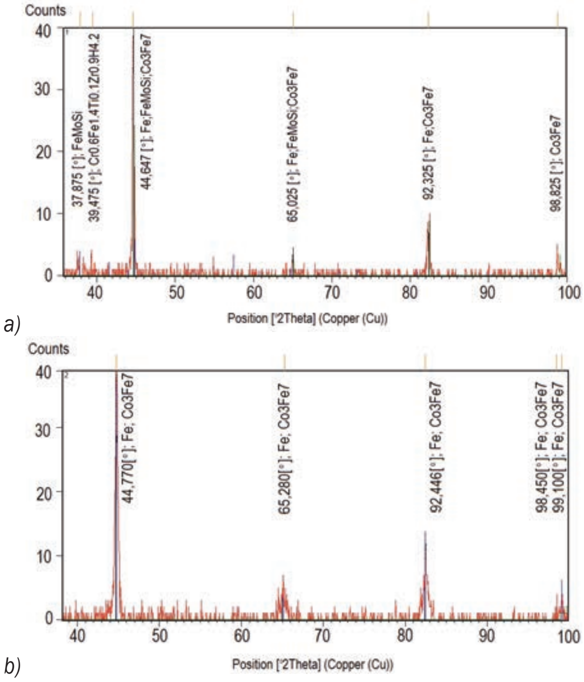

Fig. 7. *X-ray diffraction pattern of 18CrNi3Mo-Sh steel; a) in the initial state, b) after EPP strengthening*

cations are entrained by the hydrodynamic electrolyte flow and recombine on the cathode (the product's surface).

All the results in Table 3 are presented in weight fractions and expressed in percentage terms. X-ray structural analysis of 18CrNi3Mo-Sh steel samples in the state, as received (Fig. 7a), and after EPP strengthening according to mode B (Fig. 7b) revealed the α phase line, based on Fe, line $Cr_{0.6}$ $Fe_{1.4}$ phase, and also the line $Fe_{2.7}$ $Mo_{0.8}$ $Ni_{0.1}$ phases.

Table 4. *The phase composition of 18CrNi3Mo-Sh steel samples*

Processing type		Phase composition	2Theta [deg]	*d* [A]	*h*	*k*	*l*	*l* [%]
After EPP	Initial	a-phase	44.677	2.0267	1	1	0	100
			65.028	1.4331	2	0	0	11.5
			82.344	1.1701	2	1	1	17.4
		$Cr_{0.6}$ $Fe_{1.4}$	63.845	1.456730	3	0	2	17
			67.048	1.3947	2	0	5	13
			61.739	1.5013	2	1	3	21
		$Fe_{2.7}$ $Mo_{0.8}$ $Ni_{0.1}$	96.981	1.0286	4	0	0	6
			98.149	1.0195	4	0	1	1
			99.472	1.0094	2	2	4	20
		Fe_3C	44.750	2.0235	1	1	0	10.8
			65.108	1.4315	2	0	0	10
			82.444	1.1689	2	1	1	37
			99.064	1.0125	2	2	0	14

3 DISCUSSION

After EPP, an expansion of intensity acceleration and diffraction lines can be observed (Fig. 7b) relative to the initial state (Fig. 7a). This indicates a stress state due to thermal exposure. The phase composition of samples of 18CrNi3Mo steel is presented in Table 4.

As is known from [24], while hardening, the martensitic (A → M) transformation is not fully completed, and the decay products are left in steel. Lines after EPP, a phase of Fe_3C residual cementite and α-phase based on Fe, line $Cr_{0.6}$ $Fe_{1.4}$ phase, line $Fe_{2.7}$ $Mo_{0.8}$ $Ni_{0.1}$ phase indicate martensitic hardening. According to the Kurdjumow-Sachs theory [25], a martensitic crystal appears on the forming shear area. Stresses play a very important role. Sources of stress are heat gradients along the cross-section, the heterogeneity of chemical composition, structural imperfections, different spatial crystal orientations, the specific volumes of austenite and martensite, and various coefficients of phase linear extension. There is a fine-grained lamellar structure of a fine needle-like martensitic class on the cross-section cut of the electrolytic plasma-processed sample (Fig. 8). The microstructure to the processed surface (left) is characterized by a dark layer, which is the structural phase transformation formed under the influence of an ionized high plasma temperature [23]. The methods and methodology relating to Fig. 8 are mentioned in the patent specification [24].

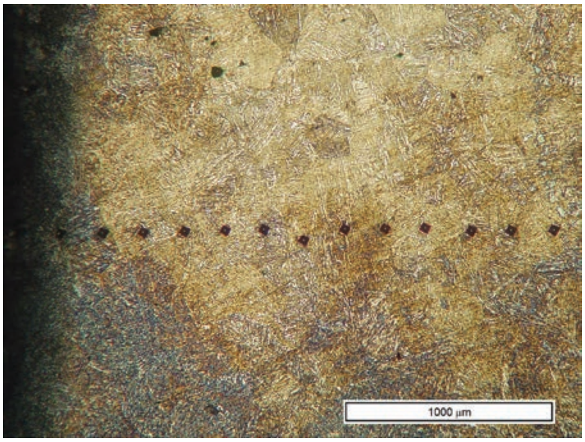

Fig. 8. *The microstructure of the cross section of 18CrNi3Mo-Sh steel after EPP strengthening (100 times increase)*

It is established that electrolytic plasma processing makes it possible to obtain a strengthened layer of thickness from 1000 µm to 1700 µm (Fig. 9). Microhardness at the cross-section of the strengthened area (martensitic structure) ranged from 6500 MPa to 7200 MPa.

The results of microhardness measurements on the surface of a heat-treated sample in a plant (VKMZ JSC) averaged 7000 MPa (Fig. 9). Microhardness decreases to the initial state and averages 3000 MPa when moving away from the processed surface [26]. The microrelief on the worn EPP surface of the steel sample after wear testing (Fig. 10a) indicates the least abrasive wear. With fine-grained martensite, a strong surface structure is formed that cannot be broken even when worn (during the experiment) by severe forms of abrasive wear, thereby preventing large areas of destruction.

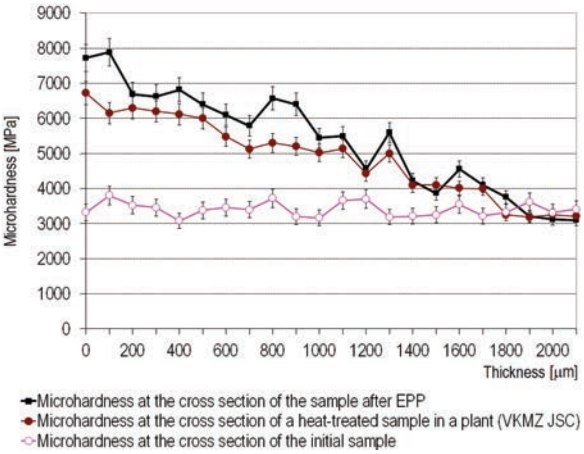

Fig. 9. *The value of the microhardness of 18CrNi3Mo-Sh steel after EPP strengthening*

The worst wear can be observed on the initial untreated steel sample (Fig. 10c). The pearlite-ferritic structure is easily abraded by abrasion, confirming the low wear resistance of thermally unprocessed steel. A steel sample that was thermally treated at JSC "VKMZ" wears out less than the initial sample (Fig. 10b). However, in terms of wear resistance, it is significantly inferior to the sample strengthened with the EPP method.

A sample after EPP strengthening has better wear resistance. As can be seen from Table 5, the steel resistance to abrasion increased significantly after EPP strengthening.

Table 5. *Value of wear of 18CrNi3Mo-Sh steel samples*

Processing type	Hv [MPa]	Wear [mg/h]
EPP strengthening	6817	54.4
Thermo processed at JSC "VKMZ"	6298	100.4
State as received	3271	150.0

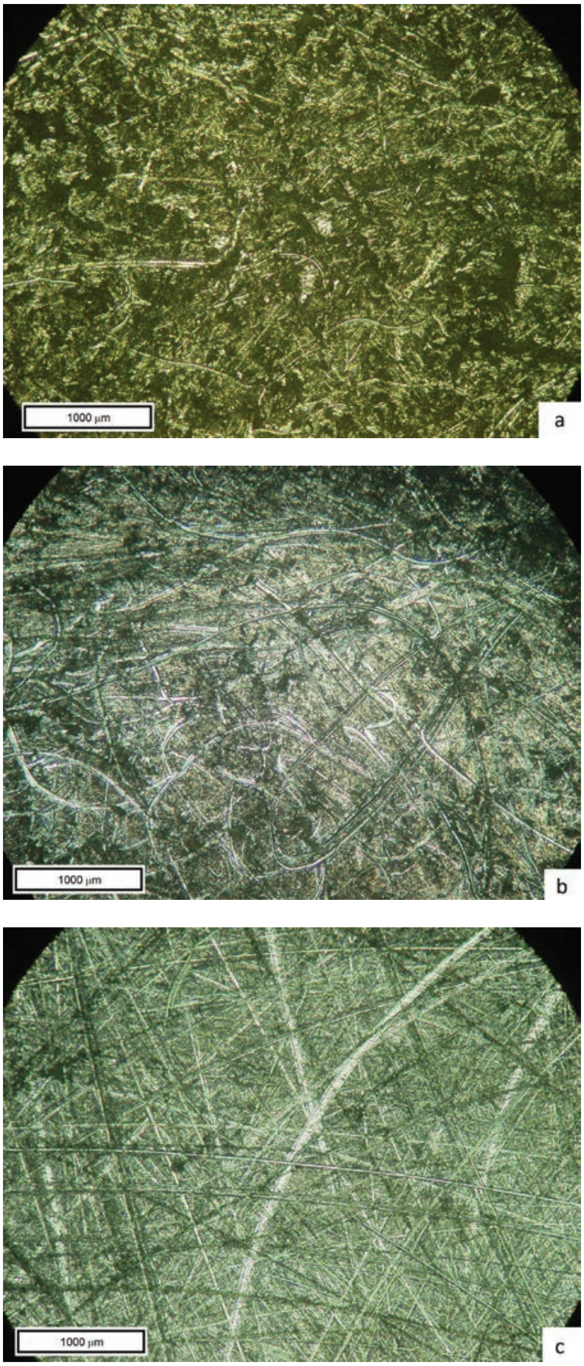

Fig. 10. *Microrelief of 18CrNi3Mo-Sh steel samples after testing for abrasive wear resistance, 100 times increase; a) after EPP strengthening, b) thermo processed at VKMZ JSC, and c) initial state*

Based on the data obtained, it can be concluded that electrolytic plasma processing significantly increases the wear resistance of drill bit component parts at low labour intensity, which reduces the cost of the product as a whole [27].

The practical significance of the obtained results of scientific research in the field of working surface hardening by the EPP method means that the developed technology applies to a wider range of parts. In particular, they include the vast majority of the articulated elements of machines that work as friction pairs. A special feature of the operating modes of articulated joints is the intense relative movement of the mated working surfaces, high contact load, unsatisfactory lubrication conditions of the friction surfaces due to the extrusion of the lubricant, the ingress of corrosive media into the mating zone, as well as abrasive particles. Such conditions are typical for loading and delivering vehicles when working in underground mines and open pit mining.

The experimental research was conducted to ensure the operability of parts on the example of the rotary mechanism hinge assembly of the underground loader Caterpillar R1300G confirmed the possibility of effective use of the developed technology to strengthen the surface parts based on the EPP method.

Thus, it has been stated by experiments that controlling EPP modes makes it possible to affect the quality of steel strengthening and obtain wear-resistant surfaces and significantly improve EPP productivity. This fact suggests the controllability of the EPP technological process and the possibility of practical implementation of the developed technology in the production

4 CONCLUSIONS

The effect of electrolytic plasma processing on phase transformations and structural changes and the properties of low-carbon and compound steels has been theoretically and experimentally studied. The microstructure of the processed surface of steel samples is characterized by a dark modified surface layer. A fine needle-like structure of martensitic origin under the dark layer changes into the initial pearlite-ferritic structure. The total thickness of the strengthened surface layer is 1000 μm to 1700 μm. The microhardness of the strengthened area of a martensitic structure is 6500 MPa to 7200 MPa. The structure of 18CrNi3Mo-Sh steel sample in the initial state is composed of particles of α–phase based on Fe, $Cr_{0.6}$ $Fe_{1.4}$ phase, as well as $Fe_{2.7}$ $Mo_{0.8}$ $Ni_{0.1}$ phase after electrolytic plasma processing in the structure of 18CrNi3Mo-Sh steel samples there appear particles of residual cementite Fe_3C, α-phase based on Fe, $Cr_{0.6}$ $Fe_{1.4}$ phase, $Fe_{2.7}$ $Mo_{0.8}$ $Ni_{0.1}$ phase, that testifies availability of martensite hardening. The most effective surface strengthening method of drill bit parts is electrolytic plasma processing. The advantages of this method are low energy consumption at high speeds of hardening, the possibility of local surface processing of parts of complex shapes operating under conditions of intense loads and the simplicity of the process.

5 ACKNOWLEDGEMENTS

This research was funded by the Science Committee of the Ministry of Education and Science of the Republic of Kazakhstan within the framework of the grant project IRN AR09058518.

6 REFERENCES

[1] Rembeza, A.I. (ed.) (1986). *Reliability and Efficiency in Technology. Methodology. Organization*. Terminology. Maszynostroienie, Moscow. (in Russian)

[2] Sokolski, P., Smolnicki, T. (2021). A method for monitoring the technical condition of large-scale bearing nodes in the bodies of machines operating for extended periods of time. *Energies*, vol. 14, no. 20, art. ID 6637, **DOI:10.3390/en14206637**.

[3] Henli, A.J., Kumamoto, H. (1984). *Reliability of Technical Systems and Risk Assessment. Translated from English*. Syromjatnikova, V.S., Demina, G.S. (eds.): Machine Industry, Moscow. (in Russian)

[4] Gui, W., Lin, J., Hao, G., Qu, Y., Liang, Y., Zhang, H. (2017). Electrolytic plasma processing-an innovative treatment for surface modification of 304 stainless steel. *Scientific Reports*, vol. 7, art. ID 308, **DOI:10.1038/s41598-017-00204-w**.

[5] Davis, J.R. (ed.) (2002). *Surface Hardening of Steels: Understanding the Basics*. ASM International, Materials Park.

[6] Nestler, K., Böttger-Hiller, F., Adamitzki, W., Glowa, G., Zeidler, H., Schubert, A. (2016). Plasma electrolytic polishing - an overview of applied technologies and current challenges to extend the polishable material range. *Procedia CIRP*, vol. 42, p. 503-507, **DOI:10.1016/j.procir.2016.02.240**.

[7] Jumbad, V.R., Chel, A., Verma, U., Kaushik, G. (2020). Application of electrolytic plasma process in surface improvement of metals: a review. *Letters in Applied NanoBioScience*, vol. 9, no. 3, p. 1249-1262, **DOI:10.33263/LIANBS93.12491262**.

[8] Lachowicz, M., Leśniewski, T., & Lachowicz, M. (2022). Effect of Dual-stage Ageing and RRA Treatment on the Three-body Abrasive Wear of the AW7075 Alloy. *Strojniški vestnik - Journal of Mechanical Engineering*, vol. 68, no. 7-8, p. 493-505, **DOI:10.5545/sv-jme.2022.142**.

[9] Janicki, D., Musztyfaga, M. (2016). Direct Diode Laser Cladding of Inconel 625/WC Composite Coatings. *Strojniški vestnik - Journal of Mechanical Engineering*, vol. 62, no. 6, p. 363-372, **DOI:10.5545/sv-jme.2015.3194**.

[10] Rakhadilov, B.K., Kozhanova, R.S., Popova, N.A., Nugumanova, A.B., Kassymov, A.B. (2020). Structural-phase transformations in 0.34C-1Cr-1Ni-1Mo-Fe steel during plasma electrolytic hardening. *Material Science - Poland*, vol. 38, no. 4, p. 699-706, **DOI:10.2478/msp-2020-0073**.

[11] Kulikov, I.S., Vashhenko, S.V., Kamenev, A.J. (2010). *Electrolyte-Plasma Processing of Materials*. Biełaruskaja Navuka, Minsk. (in Russian)

[12] Pogrebnjak, A.D., Kul'ment'eva, O.P., Kobzev, A.P., Tyurin, Yu.N., Golovenko, S.I., Bojko, A.G. (2003). Mass transfer and alloying processes during electrolytic plasma processing of cast iron. *Letters to Technical Physics Journal*, vol. 29, no. 8, p. 8-15, **DOI:10.1134/1.1573301**.

[13] Rakhadilov, B., Zhurerova, L., Pavlov, A. (2016). Method of electrolyte-plasma surface hardening of 65G and 20GL low-alloy steels samples. *IOP Conference Series: Materials Science and Engineering*, vol. 142, art. ID 012028, **DOI:10.1088/1757-899X/142/1/012028**.

[14] Rakhadilov, B.K., Kurbanbekov, Sh.R., Kylyshkhanov, M.K., Kenesbekov, A.B. (2018). Changing the structure and phase states and the microhardness of the R6M5 steel surface layer after electrolytic plasma nitriding. *Eurasian Journal of Physics and Functional Materials*, vol. 2, no. 3, p. 259-266, **DOI:10.29317/EJPFM.2018020307**.

[15] Gorelik, S.S., Skakov, J.A., Rastorguev, L.N. (2002). *X-ray and electron-optical analysis, (edition 4, updated and revised)*. Moscow Institute of Steel and Alloys, Moscow. (in Russian)

[16] Geller, J.A., Rahshtat, A.G. (1989). *Materials Sciences, (edition 6, updated and revised).* Metallurgy, Moscow. (in Russian)

[17] Skakov, M., Zhurerova. L., Scheffler, M. (2012). Way of hardening surface coating of details from steel 30CrMnSi in electrolytic plasma. *Key Engineering Materials*, vol. 531-532, p. 178-181, **DOI:10.4028/www.scientific.net/KEM.531-532.178**.

[18] Skakov, M.K., Uazyrkhanova, G.K., Popova, N.A., Scheffler, M. (2012). Influence of heat treatment and deformation on the phase-structural state of steel 30CrMnSiA. *Key Engineering Materials*, vol. 531-532, p.13-17, **DOI:10.4028/www.scientific.net/KEM.531-532.13**.

[19] Skakov, M., Rakhadilov, B., Scheffler, M., Batyrbekov, E. (2015). Microstructure and tribological properties of electrolyte plasma nitrided high-speed steel. *Materials Testing*, vol. 4, no. 57, p. 360-364, **DOI:10.3139/120.110709**.

[20] Kombaev, K.K., Kylyshkanov, M.K., Lopuhov, J. (2009). Influence of electrolytic plasma processing of 18CN3MA-ShSh steel on the surface microstructure and hardness. *Journal of the Siberian Federal University, Engineering and Technology*, vol. 2, no. 4, p. 394-399, **handle/2311/1562**, accessed on 2022-08-29. (in Russian)

[21] Kozha, E., Smagulov, D.U., Ahmetova, G.E., Kombaev, K.K. (2017). Laboratory installation for electrolytic-plasma treatment of steel. *News of the National Academy of Science of the Republic of Kazakhstan*, vol. 4, no. 424, p. 219-224.

[22] Tjulenin, A.N., Tjurin, Ju.N., Gradnev, A.I. (1988). Hysteresis of current-voltage characteristic of power supplies. *MITOM*. Moscow, no. 1, p. 9-12.

[23] Kombaev, K.K., Kozha, E., Smagulov, D.U., Sadeh, B. (2016). Structural phase transitions of low-carbon alloy steels during electrolytic-plasma processing. *Proceedings of the 2nd International Conference on Artificial and Industrial Engineering*, p. 491-495, **DOI:10.2991/aiie-16.2016.114**.

[24] Kombaev, K.K., Skakov, M.K., Putrenko, N.F. (2010). *Patent #649, Republic of Kazakhstan. Test Stand for Testing*

Materials for Friction and Wear. Patent of the State Treasury Enterprise "Eastern Kazakhstan State Technical University named after D. Serikbayev "Ministry of Education and Science of the Republic of Kazakhstan" No. 2010 / 016.2. Kazakhstan, Nur-Sultan.

[25] Kylyshkanov, M.K., Kombaev, K.K., Pogrebnyak, A.D. (2009). Patent #23178, of Republic of Kazahstan. *Method of Electrolytic Plasma Strengthening of Drill Bit Component Parts*, Nur-Sultan.

[26] Kozha, E., Smagulov, D.U., Akhmetova, G.E., Kombaev, K.K. (2017). Laboratory installation for electrolytic plasma treatment of steel. News of National Academy of Sciences of the Republic of Kazakhstan, Almaty, vol. 4, no. 424, p. 219-225.

[27] Rahadilov, B.K., Satbayeva Z., Baizhan, D. (2019). Effect of electrolytic-plasma surface strengthening on the structure and properties of steel 40KHN. *Proceedings 28th International Conference on Mettallurgy and Materials*, p. 950-955, DOI:10.37904/metal.2019.739.

Strojniški vestnik - Journal of Mechanical Engineering 68(2022)9, 552-559

DOI:10.5545/sv-jme.2022.184
Original Scientific Paper
Received for review: 2022-05-04
Received revised form: 2022-07-05
Accepted for publication: 2022-08-17

Industrial Experimental Research as a Contribution to the Development of an Experimental Model of Rolling Bearing Vibrations

Mateusz Wrzochal[1,*] – Stanisław Adamczak[1] – Grzegorz Piotrowicz[2] – Sylwester Wnuk[2]
[1] Kielce University of Technology, Poland
[2] Fabryka Lozysk Tocznych-Krasnik S.A., Poland

The influence of rolling bearing contamination on the level of generated vibrations is ignored in many cases. The influence is clearly visible in the theoretical and experimental works on the mathematical modelling of rolling bearing vibration. The authors of the most recent works in this field use substantial simplifications, often ignoring the presence of solid particles between the rolling bearing mating surfaces. However, bearing in mind the continuous improvement of the rolling bearings production processes, a series of exploratory tests in industrial conditions should be carried out, taking into account the factors affecting the bearing vibrations that are crucial in terms of quality control of the manufactured bearings. The analysis presented in this paper show that the cleanliness of the bearings is a critical factor that determines whether the rolling bearings meet quality requirements.
Keywords: rolling bearings, vibrations, bearings cleanliness, quality control

Highlights

- *Bearing contamination is an important factor in deciding whether a manufactured bearing is positively evaluated during final vibration inspection.*
- *Ignoring the cleanliness condition in the mathematical models of bearings or experimental tests is not justifiable.*
- *Bearing manufacturers focused on the development of precision bearings should, in addition to investing in the manufacturing process, develop the process of ensuring technical purity in parallel.*
- *It is necessary to conduct detailed research on the analysis of the influence of the degree of rolling bearing contamination on its vibration and to study the degree of detectability of this type of incompatibility by applied instruments and measurement methods in the bearing industry.*

0 INTRODUCTION

Various mathematical models of rolling bearing vibrations can be found in the available publications. These models are oriented toward various applications important from the point of view of the model the authors present. The theoretical studies [1] carried out thus far on the mathematical models of rolling bearings enabled us to observe that the models are constructed with far-reaching simplifications and refer only to a few factors affecting the bearing level of vibrations [2] and [3]. There is no mathematical model that includes the vast majority of real factors, and the contamination of bearings and grease is one of the most commonly ignored factors in vibration analysis [4]. In addition, most analytical models focus on a bearing with an obvious defect that may appear only as a result of a prolonged operation or inappropriate conditions of operation [5] and [6]. Therefore, the models proposed in the latest literature on the subject are not universal and cannot be applied in industrial practice [7] and [8]. The analysis of the recently published studies shows that even if contamination is included in the experimental studies, they are mainly focused on grease contamination as a result of bearing operational use [9] and [10]. Therefore, the possible contamination in the process of production and its impact on the result of quality control is definitely a separate problem [11]. The construction of a model aimed at typical industrial applications is important because there are no reference bearings (which define the correct value of the vibration level of a bearing with specific characteristics), and even more so because there are no exact reference systems with which we could compare the results obtained on individual industrial systems for vibration measurement that differ (e.g., in design) [12] and [13]. Therefore, efforts should be made to create an experimental model for brand-new bearings. To create such a model, a series of tests should be performed, including all factors influencing the vibration level, with the use of multicriteria statistics. The desired model should consider not only the imperfections affecting discrete vibrations (deviations in shape, size and position, excessive waviness, micro waviness and roughness) but also and above all the presence of solid particles in the bearing, which is an inherent result of the production process [14] and [15].

*Corr. Author's Address: Kielce University of Technology, al. Tysiąclecia Państwa Polskiego 7, 25-314 Kielce, Poland, mwrzochal@tu.kielce.pl

The basic parameters determining the quality of rolling bearings include durability (operating time in given conditions), rotation accuracy (the amount of the momentary deviation of the bearing from the operating position), rolling friction moment (mainly determining the efficiency of the device the bearing is installed in, which affects its energy efficiency), noise level (important from the everyday operation), as well as the level of vibrations (which affects the behaviour of the entire structure) [16] and [17]. The mutual proportionality of the vibration level and other indicators defining the bearing quality allows, in a simplified form, to make the bearing quality dependent on the vibration level itself (slight vibrations:high quality; significant vibrations:low quality) [18] to [20]. This quality criterion means that every bearing (without exception) is subjected to vibration control in bearing production plants. Other parameters are checked randomly or at the customer's request [21]. It can also be noted that among the applied diagnostic methods, the measurement of vibrations gives the best results and is used much more often than, for example, acoustic- or temperature-based quality control [22]. Therefore, the importance studying the vibrations of rolling bearings is justified.

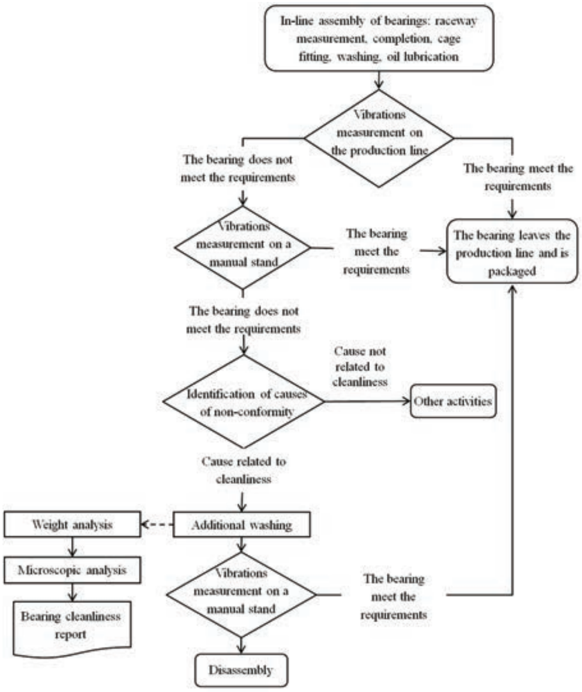

Fig. 1. *Identification and evaluation of rolling bearing contamination in the quality control process*

The study investigated the relevance of the initial bearing cleanliness in the quality control process. In order to understand the position of cleanliness control in the overall bearing acceptance inspection, a flow chart was prepared, as shown in Fig. 1.

1 VIBRATION MEASUREMENT ON THE PRODUCTION LINE

Two types of measuring devices are used to measure the level of vibrations generated by bearings in industrial conditions: automatic and semi-automatic measuring devices. Shown in Fig. 2a, automatic measuring devices are generally used in automatic assembly lines, while semi-automatic devices are used to control small series of dismantlable bearings (Fig. 2b).

The main components of such devices are a measuring unit with a vibration sensor, a measuring spindle (hydrodynamic, hydrostatic or pneumatic) and its drive, a pressure unit of the tested bearing, a bearing feeding system to the measuring stand (manual or automatic), a supporting structure with shock absorbers, and a control system.

The tested rolling bearing is mounted on a shaft rotating in the spindle (the spindle has a universal socket for shafts adapted to different types of bearings). The correct vibration measurement requires an axial load of the tested bearing. The load is introduced by pressing the outer ring with a force depending on the type of bearing. Usually, the clamps are adjustable, replaceable or, within certain limits, are universal to match the size of the tested bearing. Radial vibrations of the running and loaded bearing are recorded by an electrodynamic vibration velocity sensor with a direct contact with the stationary outer ring. The sensor is mounted in a holder and can be moved along two axes.

In the variant for measuring vibrations on a production line shown in Fig. 2b, the bearings move in turn through a trough where they are placed on the measuring shaft by a pneumatic pressure. In the case of the manual device shown in Fig. 2b, the operator places the bearing on the shaft by applying the pusher.

The above-mentioned measuring devices allow to measure the level of vibrations in three frequency bands: Low (50 Hz to 300 Hz), Medium (300 Hz to 1800 Hz) and High (1800 Hz to 10 000 Hz). The frequency bands listed above are related to the constant spindle rotational speed of 1800 min^{-1} at which all tests are carried out. This rotational speed is the reference speed and is determined by the standards for industrial measurement of bearing vibration levels (i.e., ISO 15242-1:2015 [23], ISO 15242-2:2015 [24], ISO 15242-3:2015 [25]). During the measurement, the effective value of the vibration velocity (RMS) and the maximum value (peak) are determined for each frequency band. The vibration level is expressed in different units, depending on the client's requirements: dB, μm/s, μm/s², A (anderon) or % (the conventional unit of one of the clients).

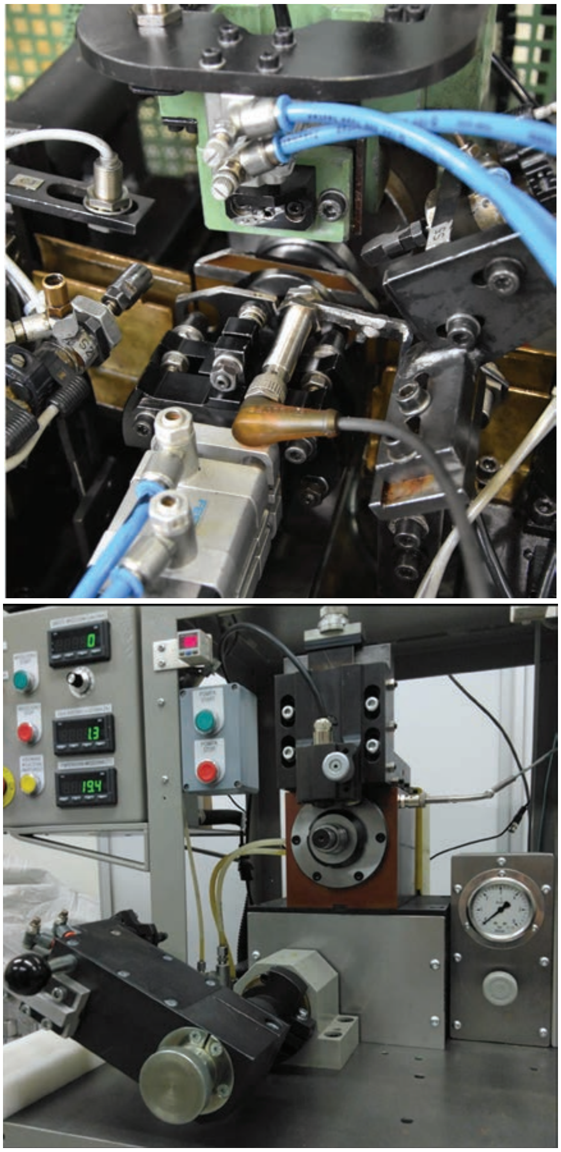

a)

b)

Fig. 2. *Industrial vibration measurement devices; a) in an automatic production cycle directly on the production line, and b) in a semi-automatic/manual production process*

In the automatic cycle, the bearing is measured twice, and the measurement is taken on both sides of the bearing; in the semi-automatic/manual cycle, the bearing is measured four times, with two measurements on each side of the bearing, every 90° in relation to the axis of measurement of the bearing. During semi-automatic/manual measurement, the bearing is additionally checked for sounds it emits. The bearing should emit a "hum" appropriate for a given bearing. Audible disturbances such as rattling, whistling, or crackling caused by contamination, damage to the race of the inner ring, outer ring, or rolling elements are unacceptable. If the device is not equipped with a vibration spectrum analyser, oscilloscopes are additionally used for measurements. The image of the vibration amplitude observed on the oscilloscope should be uniform and should not show peaks and irregularities of waves higher than one half of the baseband width for standard bearings and one third of the baseband width for bearings with a reduced level of vibrations (i.e., electric bearings (C66)). These bearings (C66) are 100 % vibration controlled, while for standard bearings, the measurement frequency is 3 % for each assembly lot but not less than 10 pieces.

The RMS value is displayed on the screen of the device in numerical form and additionally visualized in the form of bar graphs. For the bearing being measured, the RMS and "peak" limits for each band are entered before starting the measurements. The comparison of the four values obtained with the values set as the limit is decisive for the recognition of the bearing as meeting the quality requirements. Fig. 3 shows two different measurement results. Fig. 3a indicates the good quality of the tested rolling bearing: the vibration level does not exceed the assumed limits, and all bars are green). Fig. 3b shows the result of insufficient quality of the tested rolling bearing: the assumed limits are exceeded in the medium and high range (the second and third bars turn red).

The vibration level generated by the bearings is measured on open and empty bearings (without grease and seals). Such bearings are protected only with a thin film of oil. If the exposed bearing meets the quality requirements regarding the vibration level, then the closed (i.e., lubricated and sealed) bearing will meet such conditions all the more (the grease dampens vibrations in the bearing). The customer may wish to measure the vibration level in a closed bearing. In this case, the drive of the measuring device must be more powerful, and the contact pressure must be greater. The increase of these parameters (higher power of the drive and higher bearing pressure force) may accelerate the wear of the measuring device. This risk increases with the diameter and the weight of the tested bearing.

The result of the vibration level test proves its technical perfection. By making this measurement, we obtain information about potential defects of individual bearing components (outer ring, inner ring, rolling elements, cage) and possibly about impurities

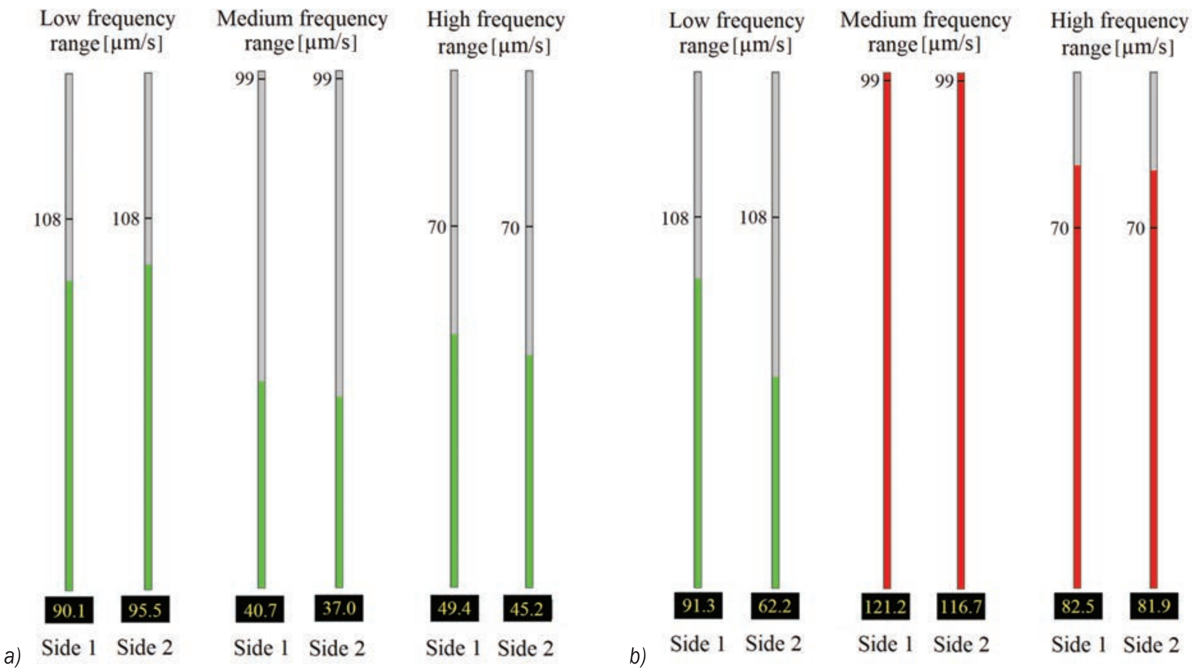

Fig. 3. *a) Bar graph that shows the vibration level measurement of a bearing in good technical condition, and b) bar graph that shows the vibration level measurement of a bearing that does not meet the assumed quality control limits*

in the bearing. The results of the vibration level measurement are subject to continuous analysis and, depending on the result, the quality controllers react in accordance with the procedures in place. Whether the defective bearings with exceeded vibration levels are isolated cases or there is an error in the process of production should be investigated.

Dirty bearings are rewashed. Bearings with exceeded vibration levels that do not show signs of significant damage, are reclassified as lower-class bearings and still offered for sale. Bearings with exceeded vibration levels that show symptoms of significant damage are dismantled. Bearing components to be dismantled: inner rings, outer rings, and rolling elements are subject to microscopic inspection. The results of this inspection have an impact on the next steps. If the problem is isolated, the production procedures should be analysed, but if more pieces are affected, the root cause of the problem should be identified and resolved. Defective bearing components are subject to regeneration if possible, and if not, they are scrapped. The detected deficiencies have an impact on the improvement of the technological process. Each improvement in the technological process upgrades the parameters of the manufactured bearing. All the improvements automatically influence the process of design and production of new, more and more accurate devices for measuring the vibration level.

2 MAIN CAUSES OF NON-CONFORMITIES FOUND BY THE QUALITY CONTROL

Contamination of the lubricating layer with solid particles is an important parameter affecting the durability of rolling bearings. The degree of life reduction caused by solid particles in the lubricating layer depends on the type, size, hardness, and quantity of particles, as well as the thickness of the lubricant layer (viscosity) and the size of the bearing. Durability tests, however, are destructive and time-consuming tests.

The level of vibration generated by a rolling bearing is a critical parameter and is inversely proportional to service life. Bearing vibration tests are much less time-consuming and do not damage the bearing. However, both in theoretical models of bearing vibrations and in experimental tests, the cleanliness of the bearing interior is largely ignored. This is due to the fact that, firstly, the contamination is very difficult to simulate mathematically, and, secondly, the experimental studies are focused on high-amplitude components in the low and medium frequency range initiated by damage or surface geometry.

To discover the most important causes of rejects, a six-month observation of the production process of rolling bearings of ten different types was performed. A total of 46,811 bearings were tested. Products that were rejected from the production process during the quality control involving the measurement of vibrations were thoroughly analysed. The causes of the defects of a given product were grouped into four categories:

- Defects in the rolling element related to an incorrect shape of one or more rolling elements, a significant surface defect, or an unsuitable size.
- Defects of the inner or outer ring related to the inadequate geometric structure of their surfaces or shape errors, less often to a local defect.
- Contamination was understood as residues left in the process of production. In most cases, after thorough washing, the bearing met the quality requirements.
- Other defects not related to the rolling element rings and contamination (i.e., cage defect or exceeding the limit of one of the three frequency bands) not related to any of the potential causes. The test results are presented in Table 1.

Table 1. *Percentage of specific causes of rejects of rolling bearings from the production line*

Type	Reject rate [%]			
	Ball defect	Outer/ inner ring defect	Contamination	Other
6016Z	53	16	31	0
63007-2RS	41	18	35	6
6311Z	64	21	12	3
6313P63	80	8	12	0
6317-2RS	52	18	20	9
6208Z	60	5	13	21
6211Z	84	16	0	0
6217-2RS	40	24	20	16
6219Z	66	21	12	2
6405	35	36	28	1

The data presented in Table 1 show that the main cause of the rejection due to the level of vibration was a ball defect. This is a special situation because this type of defect is a critical defect that, if occurs, disqualifies the bearing even though it does not exceed the limits on any of the analysed frequency bands. The reason for this situation was that the observation coincided with the delivery of defective balls deliveries from one of the suppliers. Therefore, further evaluation of the bearing vibration level was focused mainly on the detection of defective balls. After the defect was discovered, a complaint procedure was initiated in order to find the root cause, and the collected materials served as evidence confirming the scale of the problem. In addition to the defects of the balls in the observed production process, the contamination of the bearings was also a significant problem that significantly affected the level of vibration and made it difficult to assess the bearing, to capture single defects on the rings or the aforementioned defects on the balls. Therefore, when conducting research aimed at analyzing the vibrations of rolling bearings in the industrial environment, it is impossible to ignore the contamination, which constitutes a significant cause of all discrepancies. It is very important, especially for high-precision bearings designed for high-speed applications for which the evaluation of the vibration level is an important parameter determining the quality of the bearings.

3 TESTING CLEANLINESS OF BEARINGS IN INDUSTRIAL CONDITIONS

As shown by the presented long-term tests on several types of bearings, contamination is a significant cause of discrepancies discovered during quality control in bearing production plants. Bearings that are suspected of not meeting the cleanliness conditions set for them are re-washed in accordance with the procedure in place. Bearing samples, both contaminated and clean, are sent to the laboratory. There, the degree of pollution and its structure is determined. The test is performed using weight analysis and microscopic analysis.

The weight analysis consists of washing the bearing parts in extraction naphtha using ultrasound. The liquid after washing and rinsing the bearing parts is filtered through a previously soaked (in extraction naphtha), dried, and weighed nylon membrane with a mesh side of 0.8 µm. The filtrate with the bearing residue is dried and then weighed to the nearest 0.1 mg. The difference in weight of the filter after and before filtration represents the weight of the contaminations. The resulting contaminant mass is compared to the requirements.

Table 2. *The result of the weight analysis of the contaminants found in the bearings*

Bearing number	Bearing type, quantity	Mass of contaminants [mg/kg]		Contaminants above 300 μm Quantity (max. Dimension)	
		Requirements	Result	Requirements	Result
1.	6208Z	max 5 mg/kg	6.6	max 300 μm	0
2.	6208Z		4.8		1 (420)
3.	6208Z		3.7		0

After weight analysis, the filters are examined using a microscope. Microscopic analysis involves the computerized counting of particle sizes divided into five ranges: 25 µm to 50 µm, 50 µm to 100 µm, 100 µm to 150 µm, 150 µm to 200 µm, and 200 µm to 300 µm. Contaminants below 25 µm are disregarded, while those above 300 µm are not acceptable. The counting of contaminants on the surface of the dried nylon membrane is carried out at a zoom of ×100. The test allows a specific cleanliness class to be assigned according to the standards described in ISO 16232:2018 **[26]**.

Examples of the results of the weight analysis are given in Table 2. Table 3 presents an example of the result of the microscopic analysis of the tested bearings contaminants, while Fig. 4 shows the filters and the captured foreign bodies.

Table 3. *The result of the microscopic analysis of the contaminants found in the bearings*

Size ranges of contaminants [µm]		Amount of metallic contaminants [pcs]						class
		25-50	50-100	100-150	150-200	200-300	>300 (max. dimension)	
Bearing 6208Z no.	1	217	78	15	4	4	0	8
	2	93	30	13	4	1	1 (420)	ofc
	3	62	30	11	4	0	0	7

ofc - out of class

In order to ensure the appropriate cleanliness class of the bearings, modern devices with extensive filtration systems are increasingly designed for washing individual bearing elements, as well as assembled bearings. Thus, thanks to accurate systems used for measuring the level of vibration generated by bearings, we are able to determine the cause of the increased vibration level. We can also determine the reason for the problem and which stages of the technological process of bearing production can be improved.

4 CONCLUSIONS

Contamination of the lubricating layer with solid particles is a critical problem that reduces the life of rolling bearings. The degree of reduction in service life caused by solid particles in the lubricant layer depends on the type, size, hardness, and quantity of the particles, the thickness of the lubricant layer (viscosity) and the size of the bearing **[27]** and **[28]**. However, durability tests are destructive tests and are very time-consuming.

The level of vibration generated by a rolling bearing is a critical parameter that is inversely proportional to service life. Bearing vibration tests, however, are significantly less time-consuming and do not damage the bearing. However, both in theoretical models of bearing vibration and in experimental studies, bearing cleanliness is largely neglected. This is due to the fact that, firstly, the contamination is very difficult to simulate mathematically, and, secondly, the experimental studies are generally focused on high-amplitude components in the low and medium frequency range due to the damage or the geometric structure of the surface.

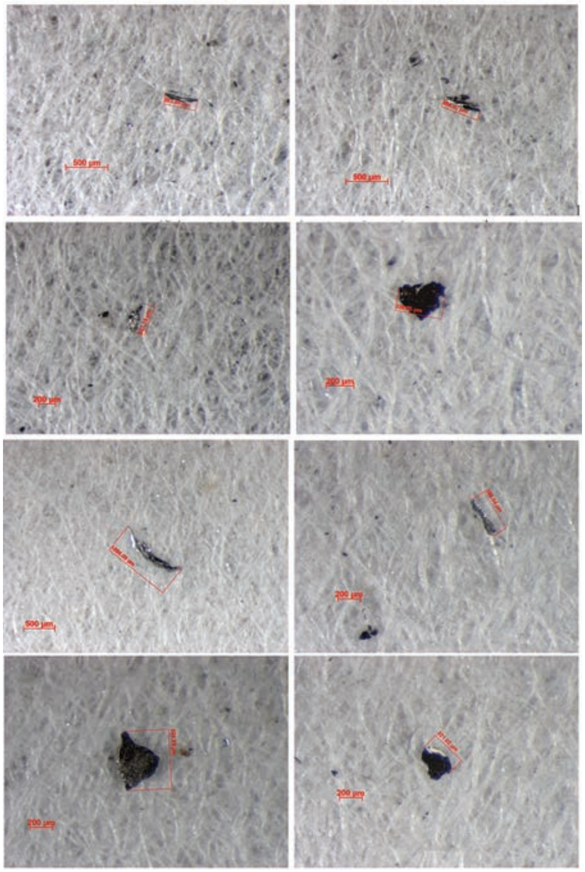

Fig. 4. *Examples of microscopic photos of the filters showing contamination of the rolling bearings*

The most important conclusion from the descriptions given in the paper is that the contamination in bearings is a very important factor that determines the positive assessment of the manufactured bearing during the final control of the vibration level. Therefore, ignoring this factor in mathematical models or experimental research is unjustified, especially since the industry trends in downsizing and striving for ever-higher operating performance make rolling bearings operate in increasingly difficult conditions with greater precision of rotation, high operating speed, minimizing noise, vibrations, and heat.

Therefore, bearing companies focused on the development of precision bearings, in addition to investing in the production process, should simultaneously develop the process of ensuring technical cleanliness. Providing and maintaining perfect cleanliness in the production process is a real challenge.

In companies producing parts for the automotive industry, the technical cleanliness of components in accordance with the requirements of ISO 16232 and VDA19 is one of the most important issues.

Due to the requirements, not only the production process and the washing process affect the final level of technical cleanliness of the components that are delivered to the final assembly. Of key importance will also be the level of cleanliness of the rooms in which the bearing production and assembly operations are performed, as well as the packaging and measures to prevent re-contamination.

In the future, the authors of this paper plan to conduct detailed research on the analysis of the impact of the degree of contamination of the rolling bearing on its vibrations and to test the degree of detection of this type of non-compliance by the instruments and measurement methods used in the bearing industry; as a result of the planned tests, it will be possible to predict the importance of bearing cleanliness to limit the level of vibrations. In turn, the planned research will be part of the preliminary research for broader studies related to an attempt to develop a model based on multi-criteria statistics that could be used to forecast vibrations of a newly manufactured bearing in the industrial environment. A model built on the basis of real data collected in a rolling bearings production plant will undoubtedly have great practical significance.

8 REFERENCES

[1] Wrzochal, M., Adamczak, S. (2020). The problems of mathematical modelling of rolling bearing vibrations. *Bulletin of the Polish Academy of Sciences: Technical Sciences*, vol. 68, no. 6, p. 1363-1372, **DOI:10.24425/bpasts.2020.135398**.

[2] Shi, P., Su, X., Han, D. (2016). Nonlinear dynamic model and vibration response of faulty outer and inner race rolling element bearings. *Journal of Vibroengineering*, vol. 18, no. 6, p. 3654-3667, **DOI:10.21595/jve.2016.16944**.

[3] Deák, K., Mankovits, T., Kocsis, I. (2017). Optimal wavelet selection for the size estimation of manufacturing defects of tapered roller bearings with vibration measurement using Shannon entropy criteria. *Strojniški vestnik - Journal of Mechanical Engineering*, vol. 63, no. 1, p. 3-14, **DOI:10.5545/sv-jme.2016.3989**.

[4] Liu, J., Shao, Y. (2015). Vibration modelling of nonuniform surface waviness in a lubricated roller bearing. *Journal of Vibration and Control*, vol. 23, no.7, p. 1115-1132, **DOI:10.1177/107754631 5589675**.

[5] Do, V.T., Nguyen, L.C. (2016). Adaptive empirical mode decomposition for bearing fault detection. *Strojniški vestnik - Journal of Mechanical Engineering*, vol. 62, no. 5, p. 281-290, **DOI:10.5545/sv-jme.2015.3079**.

[6] Kong, F., Huang, W., Jiang, Y., Wang, W., Zhao, X. (2019). Research on effect of damping variation on vibration response of defective bearings. *Advances in Mechanical Engineering*, vol. 11, no. 3, p. 1-12, **DOI:10.1177/1687814 019827733**.

[7] Soni, A., Pateriya, A., Dewada, S. (2018). Study the effects of solid and liquid contamination in ball bearing through vibration analysis. *International Research Journal of Engineering and Technology*, vol. 5, no. 5, p. 4397-4401.

[8] Jamaludin, N., Mba, D., Bannister, R.H. (2001). Condition monitoring of slow-speed rolling element bearings using stress waves. *Proceedings of the Institution of Mechanical Engineers, Part E: Journal of Process Mechanical Engineering*, vol. 215, no. 4, p. 245-271, **DOI:10.1177/095440890121500401**.

[9] Malla, C., Panigrahi, I. (2019). Review of condition monitoring of rolling element bearing using vibration analysis and other techniques. *Journal of Vibration Engineering & Technologies*, vol. 7, p. 407-414, **DOI:10.1007/s42417-019-00119-y**.

[10] Dadouche, A., Conlon M.J. (2016). Operational performance of textured journal bearings lubricated with a contaminated fluid. *Tribology International*, vol. 93, p. 377-389, **DOI:10.1016/j.triboint.2015.09.022**.

[11] Maru, M.M., Castillo, R.S., Padovese, L.R. (2007). Study of solid contamination in ball bearings through vibration and wear analyses. *Tribology International*, vol. 40, no. 3, p. 433-440, **DOI:10.1016/j.triboint.2006.04.007**.

[12] Shah, D.S., Patel V.N. (2014) A review of dynamic modeling and fault identifications methods for rolling element bearing. *Procedia Technology*, vol. 14, p. 447-456, **DOI:10.1016/j.protcy.2014.08.057**.

[13] Boškoski, P., Petrovčič, J., Musizza, B., Juričić, Đ. (2010). Detection of lubrication starved bearings in electrical motors by means of vibration analysis. *Tribology International*, vol. 43, no. 9, p. 1683-1692, **DOI:10.1016/j.triboint.2010.03.018**.

[14] Xiong, Q., Zhang, W., Xu Y., Peng, Y., Deng, P. (2018). Alpha-stable distribution and multifractal detrended fluctuation analysis-based fault diagnosis method application for axle box bearings. *Shock and Vibration*, vol. 2018, art. ID 1737219, **DOI:10.1155/2018/1737219**.

[15] Ouadine, A., Mjahed, M., Ayad H., El Kari, A. (2018). Aircraft air compressor bearing diagnosis using discriminant analysis and cooperative genetic algorithm and neural network approaches. *Applied Sciences*, vol. 8, no. 11, art. ID 2243, **DOI:10.3390/app8112243**.

[16] Kahaei, M.H., Torbatian, M., Poshtan, J. (2007). Bearing-fault detection using the meyer-wavelet-packets algorithm. *Strojniški vestnik - Journal of Mechanical Engineering*, vol. 53, no. 3, p. 186-192.

[17] Li, J., Li, M., Zhang, J., Jiang, G. (2019). Frequency-shift multiscale noise tuning stochastic resonance method for fault diagnosis of generator bearing in wind turbine. *Measurement*, vol. 133, p. 421-432, **DOI:10.1016/j.measurement.2018.10.054**.

[18] Adams, M.L. (2018). *Bearings: Bearings Basic Concepts and Design Applications*. 1st ed., CRC Press, Boca Raton, p. 92-123, p. 212-231, **DOI:10.1201/b22177**.

[19] Harris, T.A., Kotzalas, M.N. (2006). *Rolling Bearing Analysis Essential Concepts of Bearing Technology*, 5th ed., CRC Press, Boca Raton, p. 329-348, **DOI:10.1201/9781420006582**.

[20] Taylor, J.I. (2003). *The Vibration Analysis Handbook*, 2nd ed. VCI, p. 167-221.

[21] Pan, H., He, X., Tang, S., Meng, F. (2018). An improved bearing fault diagnosis method using one-dimensional CNN and LSTM. *Strojniški vestnik - Journal of Mechanical Engineering*, vol. 64, no. 7-8, p. 443-452, **DOI:10.5545/sv-jme.2018.5249**.

[22] Delgado-Arredondo, P.A., Moríñigo-Sotelo, D., Osornio-Rios, R.A., Avina-Cervantes, G.J., Rostro-Gonzales, H., Romero-Troncoso R.J. (2017). Methodology for fault detection in induction motors via sound and vibration signals. *Mechanical Systems and Signal Processing*, vol. 83, p. 568-589, **DOI:10.1016/j.ymssp.2016.06.032**.

[23] ISO 15242-1:2015. *Rolling bearings - Measuring methods for vibration - Part 1: Fundamentals*. International Organization for Standardization, Geneve.

[24] ISO 15242-2:2015. *Rolling bearings - Measuring methods for vibration - Part 2: Radial ball bearings with cylindrical bore and outside surface*, International Organization for Standardization, Geneve.

[25] ISO 15242-3:2006. *Rolling bearings - Measuring methods for vibration - Part 3: Radial spherical and tapered roller bearings with cylindrical bore and outside surface*. International Organization for Standardization, Geneve.

[26] ISO 16232:2018. *Road vehicles - Cleanliness of components and systems*. International Organization for Standardization, Geneve.

[27] Espejel, G. M., Gabelli A., Ioannides S. (2010). Lubrication and Contamination effects on bearing life. *Evolution*, vol. 2, p. 25-30, *from https://evolution.skf.com/wp-content/uploads/2013/02/EN_lubrication0.pdf*, accessed on 2022-07-28.

[28] Espejel, G. M., Gabelli A., Ioannides S. (2010). Lubrication and Contamination effects on bearing life, part 2. *Evolution*, vol. 3, p. 25-31, from *https://evolution.skf.com/wp-content/uploads/2014/10/EN_lubrication_part_2.pdf*, accessed on 2022-07-28.

Strojniški vestnik - Journal of Mechanical Engineering 68(2022)9, 560-570
DOI:10.5545/sv-jme.2022.69
Original Scientific Paper
Received for review: 2022-02-21
Received revised form: 2022-07-01
Accepted for publication: 2022-07-11

Limit-protection Method for the Workspace of a Parallel Power Head

Yanbing Ni[1,*] – Wenliang Lu[2] – Shilei Jia[2] – Chenghao Lu[2] – Ling Zhang[2] – Yang Wen[1]
[1] Tianjin University, School of Mechanical Engineering, China
[2] Key Laboratory of Mechanism Theory and Equipment Design of Ministry of Education, China

The end pose of a one-translation two-rotation (1T2R) parallel mechanism is a mapping of the servo motor action in the joint space. Because it is difficult to obtain information about the end attitude state, we have designed and implemented a simplified algorithm for determining the attitude of such a mechanism. The kinematic inverse solution of the robot and the modelling analysis of the workspace are carried out. From this, it is deduced that the length transformation of the three branch chains of the mechanism reflects the position and attitude of the end-motion platform. Based on this algorithm, the limit protection of a parallel power head under arbitrary configuration is realized. The correctness of the calculation method is verified by simulation. Finally, based on the software and hardware conditions of an existing control system, experimental verification is carried out. The experimental results show that the simplified algorithm can implement limit protection for this type of machine.

Keywords: parallel power head, modelling, workspace analysis, position and pose judgment, limit-protection

Highlights
- *The kinematics of the 1T2R head are analysed, and the workspace of the mechanism is obtained.*
- *A new simplified algorithm for position and attitude judgment is proposed.*
- *The new simplified algorithm of position and attitude judgment is combined with the mechanism control system to realize a fast limit.*
- *The algorithm is verified with simulation and experimental data.*

0 INTRODUCTION

Due to its compact structure, high stiffness to mass ratio, high precision, and good dynamic characteristics [1] and [2], the parallel power head has been of interest to both academia and the manufacturing industry and has been widely used in high-end manufacturing fields, such as large aircraft structural parts [3].

The working space is the key index for evaluating the performance of parallel power heads. Unlike tandem robots, which are driven by a series of connecting rods and rotating joints in series, parallel power heads are connected by at least two independent kinematic chains. Although the working space is relatively small, their structure is precise and compact with high repetitive positioning accuracy [4] and [5]. Workspaces can be partitioned in a number of ways, depending on performance requirements and selected parameters [6]. The factors influencing the size and shape of the workspace include the constraints of the length of the branch chain, the rotation angle, and the size of the revolute joint [7] and [8]. The methods used for the analysis of the workspace include the geometric, numerical [5], and discretization methods [9] and [10]. Gui et al. [11] proposed a reliability mathematical model based on random probability and presented a measurement and calculation method for the evaluation of the reliability level of mechanism motion. Shao et al. [12] analysed the new spatial-planer parallel mechanism using geometric methods and verified that it has good accuracy and efficiency. Kaloorazi et al. [13] used the structural geometry method to determine the maximum non-singularity workspace of a 3-degree of freedom (3-DOF) parallel mechanism, and Huang et al. [9] obtained the workspace of the Stewart-Gough manipulator by a discrete method. The scientific community has also made many achievements in numerical method research. Zhang [14] et al. used the fast search method to calculate the workspace volume and took it as the optimization objective function. In addition, Gao and Zhang [15] and Zhu et al. [16] used the modified boundary search method to obtain the workspace of a parallel mechanism. Farzaneh-Kaloorazi et al. [17] used an interval analysis approach for the barrier-free working space of a parallel mechanism. Majid [18] et al. analysed the workspace of a three-prismatic-prismatic-spheric-revolute (3-PPSR) manipulator using the numerical method and found that three regions in the workspace corresponded to the postures of a type of manipulator.

In order to make more reasonable and effective use of the existing working space and ensure the safe and reliable operation of the parallel power

*Corr. Author's Address: Tianjin University, School of Mechanical Engineering, China, niyb5812@tju.edu.cn

head, the method of trajectory planning and space limitation is often adopted [19] and [20]. Khoukhi et al. [21] proposed a multi-objective dynamic trajectory planning method for the parallel mechanism under the constraints of task, workspace, and mechanism with the help of the discrete augmented Lagrangian technique. Reveles et al. [22] proposed a kinematic redundant parallel robot joint trajectory planning method using a feasibility map, which plans the joint trajectory while avoiding parallel singularities through the graphical evaluation of the robot pose related to four working modes. Dash et al. [23] proposed a numerical path planning method to avoid the singularity of the mechanism in the accessible workspace of a parallel robot by clustering the singularities and using the local routing method based on Grassmann line geometry to avoid the singularities. Iqbal et al. [24] discussed two complex control strategies: computational torque control (CTC) and variable structure control (VSC) and improved the trajectory-tracking performance of the robot. Manzoor et al. [25] integrated the functions of mechanical computer-aided design (CAD) and robot CAD into the same platform and achieved the accurate control of the robot through various three-dimensional models in the platform. Alam et al. [26] considered two different methods based on sliding mode control (SMC) to achieve the nonlinear control of an elastic joint robot. This control method enables the robot to obtain a locally stable closed-loop system.

Because the pose of the end of the one-translation two-rotation (1T2R) parallel mechanism in the operation space is a nonlinear mapping of the motion of the servo motor in the joint space, the modelling and calculation process is complicated, the motion controller takes a long time. It is therefore impossible to realize the real-time operation to prevent exceeding the limit during the operation of the mechanism. The purpose of this paper is to propose a simplified algorithm for position and attitude judgment, which can greatly reduce the calculation amount of limit, and realize the limit protection of the 1T2R parallel power head through a combination of software and hardware. Firstly, the inverse kinematics analysis was carried out, and the mapping relationship between the terminal pose of the mechanism and each input value was constructed based on the inverse kinematics model. Then, according to the mechanism structure, scale parameters, range of motion of each pair, interference and other constraints, the working space of 1T2R power head was determined. By analysing and summarizing the motion rules of 1T2R power head, a simplified algorithm for judging the position and pose of 1T2R power head was obtained, which was used to realize the limit protection of the 1T2R head. Finally, the algorithm was verified via experimentation.

1 KINEMATIC ANALYSIS

The position inverse solution of the 1T2R head is to solve the rod length quantity of each branch chain motion joint by knowing the positional parameters of the end reference point of the tool providing the theoretical model for mechanism error analysis and control.

1.1 Machine Tool Profile

As shown in Fig. 1, a 1T2R mechanism is a parallel mechanism with one translational and two rotational degrees of freedom. A 1T2R power head is composed of a moving platform, a static platform, and three RPS branch chains, in which R, P, and S represent revolute joints, active prismatic pairs and spherical joints, respectively. One end of each RPS branch chain is connected to the moving platform through a spherical joint, and the other end is connected to the static platform through a revolute joint. The motorized spindle is installed on the moving platform and the active prismatic pair is driven by a servo motor.

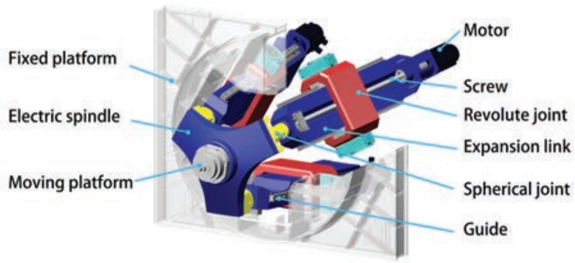

Fig. 1. *Model of 1T2R spindle head*

1.2 Inverse Kinematic Solution

The power head of the 1T2R mechanism diagram is shown in Fig. 2, A_i and B_i represent the centres of the spherical joint and the revolute joint, respectively; $\Delta A_1A_2A_3$ and $\Delta B_1B_2B_3$ are equilateral triangles; points O' and O are the geometric centres of the two triangles; the moving platform is represented by $\Delta A_1A_2A_3$; the static platform is represented by the plane of $\Delta B_1B_2B_3$; point P is the tip at the end of the mechanism; e is the distance from P to the plane of the moving platform; a,b are the circumcircle radii of the moving and static platform, respectively; l represents the initial branch length.

The fixed and moving coordinate systems $O-xyz$ and $O'-x'y'z'$ are established at the centre O and O' of the fixed and moving platforms, respectively. In the initial position, the z' axis and z axis are perpendicular to the planes $A_1A_2A_3$ and$B_1B_2B_3$, respectively, as shown in Fig. 2. The x' axis and x axis are along the $\overrightarrow{A_3A_2}$ direction and $\overrightarrow{B_3B_2}$, respectively. The y' axis and y axis are determined according to the right-hand rule. α and β represent rotation about the x axis and y axis, respectively.'

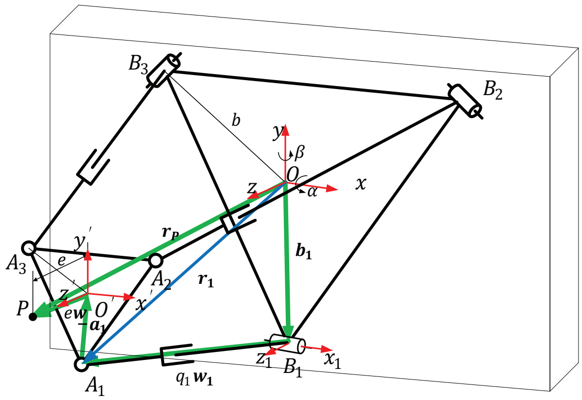

Fig. 2. *Mechanism sketch of 1T2R mechanism*

The attitude transformation matrix of $O'-x'y'z'$ in the connected body coordinate system of a moving platform relative to $O-xyz$ in the static platform coordinate system is R:

$$\begin{aligned}\mathbf{R} &= \mathrm{Rot}(z,\psi)\mathrm{Rot}(x,\theta)\mathrm{Rot}(z,\phi) \\ &= \begin{bmatrix} c\psi\, c\phi - s\psi\, c\theta\, s\phi & -c\psi\, s\phi - s\psi\, c\theta\, c\phi & s\psi\, s\theta \\ s\psi\, c\phi + c\psi\, c\theta\, s\phi & -s\psi\, s\phi + c\psi\, c\theta\, c\phi & -c\psi\, s\theta \\ s\theta\, s\phi & s\theta\, c\phi & c\theta \end{bmatrix} \\ &= [\mathbf{u} \quad \mathbf{v} \quad \mathbf{w}], \end{aligned} \tag{1}$$

where s=sin, c=cos, $\mathbf{u}$, $\mathbf{v}$, $\mathbf{w}$ represent the measurement of three coordinate axes of $O'-x'y'z'$ in the static platform coordinate system $O-xyz$, respectively, and $\mathbf{w}$ can be used to represent the tool attitude vector.

ψ, θ, ϕ are the precession angle, nutation angle and spin angle, respectively, which are related to α and β:

$$\begin{cases} \theta = \arccos(\cos\alpha\cos\beta) \\ \psi = \mathrm{atan2}\left(\dfrac{\cos\alpha\sin\beta}{\sin\theta}, \dfrac{\sin\alpha}{\sin\theta}\right) \end{cases}. \tag{2}$$

As shown in Fig. 2, the position vector of the tool point P at the end of the mechanism in the static platform coordinate system $O-xyz$ is:

$$\mathbf{r}_P = [x_P \quad y_P \quad z_P]^{\mathrm{T}}. \tag{3}$$

The following vector equation can be obtained:

$$\mathbf{r}_P = \mathbf{b}_i + q_i\mathbf{w}_i - \mathbf{a}_i + e\mathbf{w} \quad i = 1,2,3, \tag{4}$$

where $\mathbf{a}_i$, $\mathbf{b}_i$ is the position vector of A_i, B_i; $\mathbf{a}_i = \mathbf{R}\mathbf{a}_{i0}$; $\mathbf{b}_i = b[\cos\varphi_i \quad \sin\varphi_i \quad 0]^{\mathrm{T}}$; $\mathbf{a}_{i0}$ is the measurement of A_i in the connected coordinate system of moving platform, $\mathbf{a}_{i0} = a[\cos\varphi_i \quad \sin\varphi_i \quad 0]^{\mathrm{T}}$; φ_i is the structural angle of $\overrightarrow{O'A_i}$ and $\overrightarrow{OB_i}$ relative to x' axis and x axis respectively, $\varphi_i = 2\pi(i-1)/3 - \pi/2$; q_i and $\mathbf{w}_i$ are the length of the branch chain and the unit vector, respectively.

Since the revolute joint will restrict the branch chain from moving along the x_i axis, dot product x axis direction unit vector $\boldsymbol{u}_{ix} = [cos\varphi_i \quad sin\varphi_i \quad 0]^{\mathrm{T}}$ at both ends of Eq. (4):

$$(\mathbf{r}_P + \mathbf{a}_i - e\mathbf{w})^{\mathrm{T}} \cdot \mathbf{u}_{ix} = 0. \tag{5}$$

Solve Eq. (5) to obtain

$$\begin{aligned} x_P &= \frac{a}{2}\sin(2\psi)(1-\cos\theta) + e\sin\psi\sin\theta, \\ y_P &= \frac{a}{2}\cos(2\psi)(1-\cos\theta) - e\cos\psi\sin\theta, \\ \phi &= -\psi. \end{aligned} \tag{6}$$

From Eq. (6)

$$\begin{cases} q_i = \|\mathbf{r}_P - \mathbf{b}_i + \mathbf{a}_i - e\mathbf{w}\| = \|\mathbf{r}_P - \mathbf{b}_i - \mathbf{s}_i\| \\ \mathbf{w}_i = {\mathbf{r}_P - \mathbf{b}_i - \mathbf{s}_i} \big/ {q_i} \quad i = 1,2,3 \end{cases}, \tag{7}$$

where $\mathbf{s}_i$ is the vector of the geometric centre of the spherical pairs pointing to the tool reference point in the static coordinate system, and $\mathbf{s}$ is the vector of the geometric centre of the spherical pairs pointing to the tool reference point in the moving coordinate system.

$$\mathbf{s}_i = \mathbf{R}\mathbf{R}_i\mathbf{s}, \mathbf{s} = [0 \quad a \quad e]^{\mathrm{T}}, \tag{8}$$

$$\mathbf{R}_i = \begin{bmatrix} \cos(\varphi_i + \pi/2) & -\sin(\varphi_i + \pi/2) & 0 \\ \sin(\varphi_i + \pi/2) & \cos(\varphi_i + \pi/2) & 0 \\ 0 & 0 & 1 \end{bmatrix}, \quad i = 1,2,3. \tag{9}$$

2 WORKSPACE ANALYSIS

The constraints of the 1T2R head include its structure, scale parameters (a, b, l, e), motion range of each prismatic pair and interference. Workspace analysis

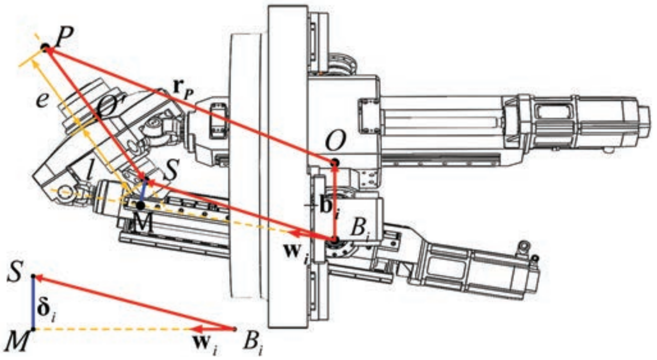

Fig. 3. *Interference position of 1T2R spindle head*

is used to determine the set of all reachable space position points of the tool reference point under the above constraints.

2.1 Constraint Analysis

The 1T2R power head is restricted by its own mechanical structure and other conditions and can only work within a certain space range. After analysing the structure of the 1T2R head, the constraint conditions are as listed in Table 1.

Table 1. *Restrictions of 1T2R mechanism*

Constraint type	Constraint value
Active prismatic pair length constraint	$0.4\text{ m} \leq q_i \leq 0.915\text{ m}$
Rotation angle constraint of revolute joint	$-12° \leq \theta_i \leq 3°$
Angle constraint of spherical joint	$\lvert\alpha_i\rvert \leq 45°$, $\lvert\beta_i\rvert \leq 90°$
Interference between principal axis and branched chain	$\delta_i \geq 0.15\text{ m}$
Interference between tool point and table	$z_P \leq 1.250\text{ m}$

$q_{i\min}$ and $q_{i\max}$ are the maximum and minimum lengths of the active prismatic pairs, respectively; $\theta_{i\min}$ and $\theta_{i\max}$ are the maximum and minimum values of each revolute joint angle, respectively; $\alpha_{i\min}$ and $\beta_{i\max}$ are the maximum values of angles α and β of each spherical joint, respectively; δ_i is the linear distance from point S of the spindle end to the branch chain; $\delta_{i\min}$ is the minimum allowable actual linear distance between the spindle end and the branch chain. As shown in Fig. 3, δ_i can be obtained as follows:

$$\delta_i = \left|\mathbf{w}_i \times \mathbf{r}_{B_iS}\right| = \left|\mathbf{w}_i \times \left(\mathbf{r}_P - e\mathbf{w} - l\mathbf{w} - \mathbf{b}_i\right)\right|. \quad (10)$$

2.2 Workspace Description

A hierarchical processing approach can be used to divide the workspace into multiple subspaces. The boundary region of the subspace is then determined by means of the quasi-spherical coordinate search method [27], and the envelope surface and the stereogram of the workspace are described，defining the accessible working space for 1T2R heads as shown in Fig. 4. It can be seen from the calculation results that 1T2R head can realize the attitude space range with a maximum of $\theta \in [0° \quad 40°]$, $\psi \in [0° \quad 360°]$. As we can see from the reachable workspace, not all regions can achieve the maximum nutation angle.

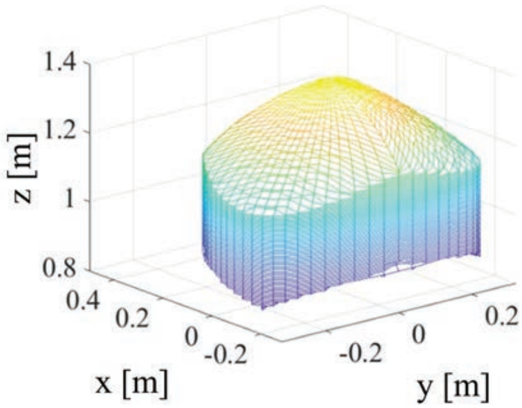

Fig. 4. *Reachable workspace of 1T2R*

3 POSE DETERMINATION AND SIMPLIFICATION ALGORITHM

By analysing and summarizing the motion rules of 1T2R head, a simplified algorithm for judging the position and pose of 1T2R parallel power head is derived. This algorithm can realize the fast response of the limit protection function under the existing hardware configuration and is used to realize the limit protection of the 1T2R head.

To facilitate calculation, the relationship between the coordinates of the tool reference point in the z and the coordinates $z_{O'}$ of the geometric centre point of the moving platform in the direction of z is:

$$z = z_{O'} + e\cos\theta. \quad (11)$$

Thus, the input parameters of the inverse kinematics model of the 1T2R head are replaced by the coordinates of the geometric centre point O' of the moving platform in the z direction, the process angle ψ and the nutation angle θ.

Q is defined as the kinematic chain length of the branch chain movement; Q' is the difference between the kinematic chain lengths of any two branch chains.

3.1 Position Constraint Condition

As shown in Fig. 2, let the vector from the geometric centre point O of the static platform to the geometric centre point O' of the moving platform be $\mathbf{o}$. $\mathbf{r}_P$ can be expressed as

$$\mathbf{r}_P = \mathbf{o} + e\mathbf{w}. \quad (12)$$

Substituting Eq. (12) into Eq. (3), we obtain:

$$q_i\mathbf{w}_i = \mathbf{a}_i - \mathbf{b}_i + \mathbf{o} \quad i = 1,2,3\,. \quad (13)$$

By summing the above equation in order of i, and taking into account the geometric relation of the prototype $\mathbf{a}_1+\mathbf{a}_2+\mathbf{a}_3=\mathbf{b}_1+\mathbf{b}_2+\mathbf{b}_3=\mathbf{0}$, we obtain:

$$\left|q_1\mathbf{w}_1+q_2\mathbf{w}_2+q_3\mathbf{w}_3\right| = 3\left|\mathbf{o}\right|. \quad (14)$$

According to Eq. (13), the left side of the above equation is equal to $\mathbf{a}_1+\mathbf{a}_2+\mathbf{a}_3=\mathbf{b}_1+\mathbf{b}_2+\mathbf{b}_3=\mathbf{0}$; therefore:

$$\left|q_1\mathbf{w}_1\right|+\left|q_2\mathbf{w}_2\right|+\left|q_3\mathbf{w}_3\right| \le 3\left|\mathbf{o}\right|+\left|\mathbf{a}_1-\mathbf{b}_1\right|+\left|\mathbf{a}_2-\mathbf{b}_2\right|+\left|\mathbf{a}_3-\mathbf{b}_3\right|. \quad (15)$$

Because $|\mathbf{a}_1-\mathbf{b}_1|+|\mathbf{a}_2-\mathbf{b}_2|+|\mathbf{a}_3-\mathbf{b}_3|$ has a maximum value of $6a\sin(\theta_{\max}/2)$ at the maximum nutation angle, the following can be obtained by sorting:

$$\left(\left|\mathbf{a}_1-\mathbf{b}_1\right|+\left|\mathbf{a}_2-\mathbf{b}_2\right|+\left|\mathbf{a}_3-\mathbf{b}_3\right|\right)_{\max} = 6a\sin\left(\theta_{\max}/2\right). \quad (16)$$

By combining Eq. (15) and Eq. (15), and substituting $|q_1\mathbf{w}_1|+|q_2\mathbf{w}_2|+|q_3\mathbf{w}_3|=Q$, the following is obtained:

$$3\left|\mathbf{o}\right| \le Q \le 3\left|\mathbf{o}\right| + 6a\sin\left(\theta_{\max}/2\right). \quad (17)$$

It can be seen from Eq. (17) that, theoretically, the sum of kinematic chains of the 1T2R power head branch prismatic pair is always approximately three times the distance from the geometric centre point of the static platform to the geometric centre point of the moving platform.

3.2 Pose Constraint Condition

A similar calculation is used for the difference of length between any two branch chains. The length difference between branched chains 1 and 2 is used as an example, which can be determined from Eq. (13):

$$q_1\mathbf{w}_1 - q_2\mathbf{w}_2 = \mathbf{a}_1 - \mathbf{a}_2 - \mathbf{b}_1 + \mathbf{b}_2. \quad (18)$$

The difference between the two sides of a triangle is less than the third:

$$\left\|q_1\mathbf{w}_1\right| - \left|q_2\mathbf{w}_2\right\| \le \left|q_1\mathbf{w}_1 - q_2\mathbf{w}_2\right|. \quad (19)$$

Substitute Eq. (23) into, and we obtain:

$$\left\|q_1\mathbf{w}_1\right| - \left|q_2\mathbf{w}_2\right\| \le \left|\mathbf{a}_1 - \mathbf{a}_2 - \mathbf{b}_1 + \mathbf{b}_2\right|, \quad (20)$$

because $\mathbf{a}_1=a\mathbf{RV}_1$, $\mathbf{a}_2=a\mathbf{RV}_2$, $\mathbf{b}_1=b\mathbf{V}_1$, $\mathbf{b}_2=b\mathbf{V}_2$, $\mathbf{V}_i = [\cos\varphi_i \quad \sin\varphi_i \quad 0]^{\mathrm{T}}$, $i=1,2$.

According to the actual parameters of the mechanism, $a = b$ is substituted, and then:

$$\begin{aligned}&\left|\mathbf{a}_1 - \mathbf{a}_2 - \mathbf{b}_1 + \mathbf{b}_2\right| = \\ &= a\left|(\mathbf{R}-\mathbf{E})\mathbf{T}\right| \le 2a\left(1-\cos\left(\varphi_1-\varphi_2\right)\right)\left|\mathbf{R}-\mathbf{E}\right|,\end{aligned} \quad (21)$$

where, $\mathbf{E}$ is identity matrix,
$\mathrm{T}=[\cos\varphi_1-\cos\varphi_2 \quad \sin\varphi_1-\sin\varphi_2 \quad 0]^{\mathrm{T}}$.

According to Eq. (1), the matrix $\mathbf{R}$ is related to the precession angle ψ, nutation angle θ and spin angle ϕ, and further:

$$\left|\mathbf{a}_1 - \mathbf{a}_2 - \mathbf{b}_1 + \mathbf{b}_2\right| = 2a\left(1-\cos\left(2\pi/3\right)\right) f\left(\psi,\theta\right). \quad (22)$$

Substituting Eq. (22) into Eq. (21), we obtain:

$$\left\|q_1\mathbf{w}_1\right| - \left|q_2\mathbf{w}_2\right\| \le 2a\left(1-\cos\left(2\pi/3\right)\right) f\left(\psi,\theta\right). \quad (23)$$

According to Eq. (26), we then obtain:

$$\left|Q'\right| \le 2a\left(1-\cos\left(2\pi/3\right)\right) f\left(\psi,\theta\right). \quad (24)$$

It can be seen from Eq. (24) that, theoretically, the upper bound of the length difference between any two branching chains of the 1T2R head is a function of ψ and θ.

3.3 Simulation

The form of motion in which the tool makes an arc trajectory parallel to the plane of the static platform is relatively simple and easy to describe. Therefore, under this motion, the above conclusions are verified by combining the existing 1T2R parallel mechanism data. When the values of $z_{O'}$ and θ remain unchanged at $\psi \in [0° \quad 360°]$, the length of 1T2R head branch chain prismatic pair is calculated as shown in Fig. 5.

Since the leg length data q_1, q_2 and q_3 satisfy the symmetric three-phase sine quantity. The values of $z_{O'}$ and θ can be changed and the leg length data summed to obtain Table 2. The difference of the leg length data is taken to obtain Table 3.

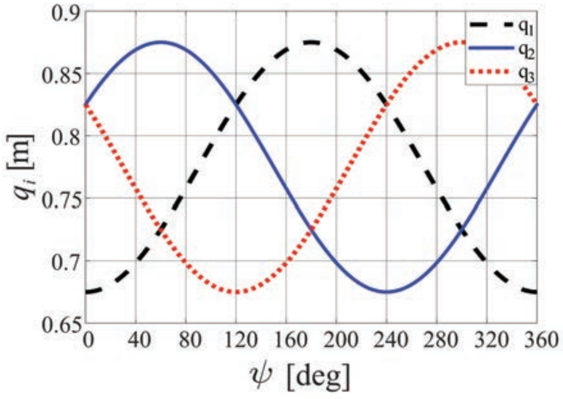

Fig. 5. *Data distribution type of 1T2R branches' length*

Table 2. *Summation of 1T2R head branches' length*

		$\theta=39$	$\theta=29°$	$\theta=19°$	$\theta=9°$	$\theta=0°$	max/min
1.8720	Q_{max}	1.879424	1.874194	1.872384	1.872018	1.872000	1.879424
	Q_{min}	1.876457	1.873482	1.872296	1.872016	1.872000	1.872000
1.9695	Q_{max}	1.976447	1.971561	1.969863	1.969517	1.969500	1.976447
	Q_{min}	1.973780	1.970920	1.969783	1.969515	1.969500	1.969500
2.0670	Q_{max}	2.073528	2.068943	2.067343	2.067016	2.067000	2.073528
	Q_{min}	2.071116	2.068363	2.067271	2.067015	2.067000	2.067000
2.1645	Q_{max}	2.170656	2.166338	2.164826	2.164516	2.164500	2.170656
	Q_{min}	2.168465	2.165811	2.164760	2.164514	2.164500	2.164500
2.2620	Q_{max}	2.267824	2.263744	2.262310	2.262015	2.262000	2.267824
	Q_{min}	2.265824	2.263262	2.262250	2.262013	2.262000	2.262000

Table 3. *Subtraction of any two 1T2R head branches' length*

$z_{O'}$		$\theta=39$	$\theta=29°$	$\theta=19°$	$\theta=9°$	$\theta=0°$
0.6240	Q'_{max}	0.271960	0.209725	0.140941	0.067737	0
	Q'_{min}	-0.271960	-0.209725	-0.140941	-0.067737	0
0.6565	Q'_{max}	0.272005	0.209745	0.140944	0.067737	0
	Q'_{min}	-0.272005	-0.209745	-0.140944	-0.067737	0
0.6890	Q'_{max}	0.272056	0.209763	0.140947	0.067737	0
	Q'_{min}	-0.272056	-0.209763	-0.140947	-0.067737	0
0.7215	Q'_{max}	0.272098	0.209779	0.140950	0.067737	0
	Q'_{min}	-0.272098	-0.209779	-0.140950	-0.067737	0
0.7540	Q'_{max}	0.272134	0.209793	0.140952	0.067737	0
	Q'_{min}	-0.272134	-0.209793	-0.140952	-0.067737	0
Average value	Q'_{max}	0.272051	0.209761	0.140947	0.067737	0
	Q'_{min}	-0.272051	-0.209761	-0.140947	-0.067737	0

According to the data of Fig. 5 and Table 2, the following relationship can be fit:

$$\underline{Q} \le Q \le \overline{Q}, \tag{25}$$

where, $\underline{Q}$ represents the lower bound of the length sum of the branch chain movement, $\underline{Q}=3z_{O'}$, $\overline{Q}$ represents the upper bound of the length sum of the branch chain movement

$$\overline{Q}=3z_{O'}-0.012251z_{O'}+0.015190.$$

From the data in Table 2 and the Eq. (25), it can be seen that the length of the 1T2R head branch chain prismatic pair is always approximately equal to three times of $z_{O'}$, which satisfies the Eq. (21). Therefore, the motion characteristic law of this form of motion can be extended.

By the same token, through Fig. 5 and Table 3, Q' and θ can be fitted as follows:

$$|Q'| \leq \overline{Q'}, \tag{26}$$

where, $\overline{Q'}$ represents the upper bound of the length difference $|Q'|$ of the auxiliary leg of the branch chain movement, $\overline{Q'} \leq 0.0069997\theta + 0.003748$.

It can be seen from Eq. (26) that in the case of the same nutation angle, the upper bound of the difference between the length of any two kinematic chains is almost the same, with only an error of orders of magnitude. This satisfies Eq. (24). Therefore, the motion characteristic law of this form of motion can be extended.

The above is the analysis of the motion characteristics of a 1T2R head and the simplified algorithm of pose judgment. The aim of the algorithm is to further divide the working space of the mechanism through the information of the three branch chains, so that the judgment of the attitude of the mechanism can be obtained without establishing a complex mapping model of the servo motor action. Within its workspace, the sum length of the 1T2R head branch chain prismatic pair is always approximately equal to three times the coordinate value of the geometric centre of the moving platform. The absolute value of the difference between the lengths of any two branch chains is always less than a specific value related to the nutation angle. Thus, the limit protection of 1T2R head can be realized simply, reliably, and efficiently.

4 LIMIT PROTECTION IMPLEMENTATION PROCESS

Based on the above analysis results of the movement characteristics of a 1T2R power head, the simplified algorithm of position and pose judgment, the limit protection method is designed in combination with the actual mechanical structure of the 1T2R power head servo feed system and its control system. This method will adopt two methods: proactive limit and preventive limit.

The active limits are all areas of the 1T2R power head dexterous workspace except the boundary. The preventive limits are to prevent the mechanism from exceeding the workspace boundary, i.e., the boundary area of the 1T2R power head dexterous workspace. Real-time data of the prismatic pair length of the branch chain can be obtained through the feedback signal of the encoder of the servo motor. The PLC program in the motion controller PMAC is used to sum the leg lengths of the three branches and calculate the difference between the lengths of any two branches. The results of the operation are fed into the motion controller register. Then, according to the above pose judgment algorithm, whether the limit area is exceeded can be determined. The specific realization method of the 1T2R power head limit is shown in Fig. 6.

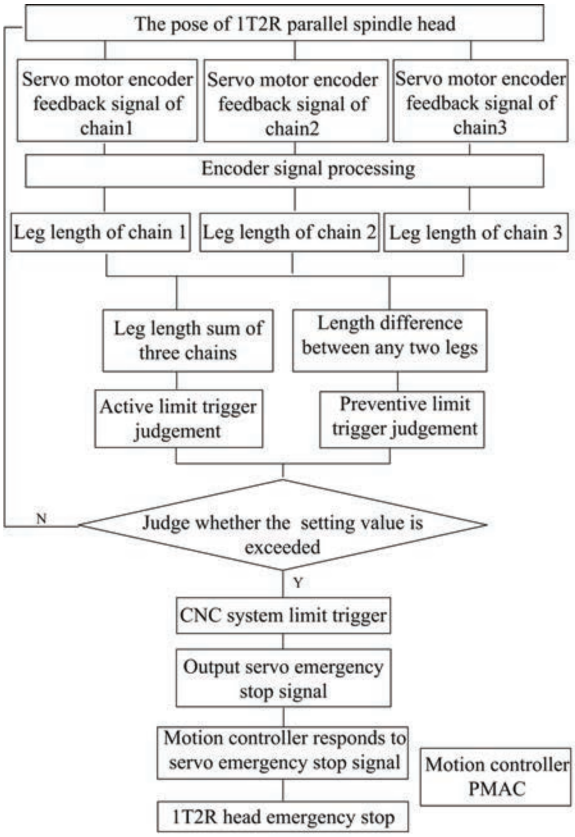

Fig. 6. *Schematic diagram of limit protection process*

For the active limit, according to Table 2, Q_{min} = 1.872000 is determined to be the lower trigger condition value of the active limit, and Q_{max} = 2.267824 is determined to be the upper trigger condition value of the active limit. For the preventive limit position, according to the data shown in Table 3, it is determined that Q'_{max} = 1.272134 is the upper limit trigger condition value of the preventive limit position, and Q'_{min} = –0.272134 is the lower limit trigger condition value of the preventive limit position.

5 EXPERIMENTAL ANALYSIS

The experimental platform is shown in Fig. 7, and the 1T2R parallel power head is driven by three chains. Fig. 8 shows the servo feed control system. The real-time length of three branches can be obtained through the code disk of the branch servo motor. The trajectory is an approximately circular trajectory parallel to the plane of the static platform, as shown in Fig. 9. According to the scale parameters (a, b, l, e) mentioned above, after consulting the machine tool operation manual, it is found that collision interference occurs easily when the nutation angle is 40°, so the nutation angle θ is selected as 30°. The motion position of the tool reference point P at the end of the mechanism in the z direction is 1.1687 m, the nutation angle θ is 30°, and the precession angle ψ is varied from 0° to 360°. The length data of each chain obtained during the experiment are shown in Table 4. Fig. 10 shows the variation rule of the length of the branch chain corresponding to the trajectory.

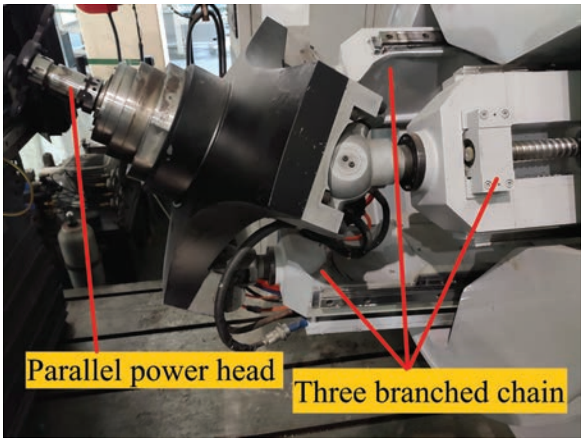

Fig. 7. *1T2R parallel power head*

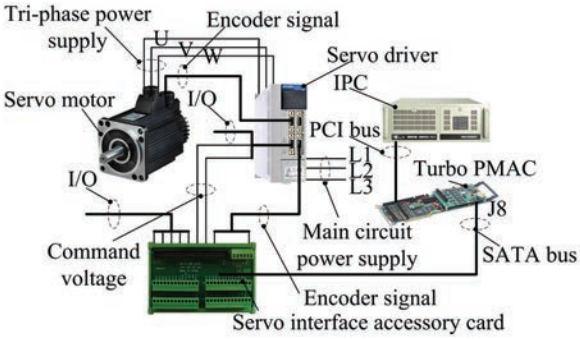

Fig. 8. *Servo feed control system*

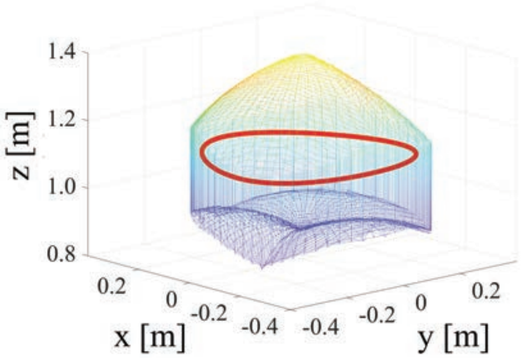

Fig. 9. *Schematic diagram of trajectory reachable workspace*

Fig. 11a shows the numerical distribution law after the summation of the length data of the motion track. It can be seen from the distribution of the summation result that the sum of the length is distributed within the interval range of 2.2514 m to 2.2521 m and has periodic data fluctuation with a small amplitude. As shown in Fig. 11b, in comparing the length of the data points and the result data with the threshold value of the over-limit setting, it is found that none of the data points in the trajectory exceed the limit.

Table 4. *Experimental kinematic chain length data*

t [s]	0.0000	0.0221	0.0443	0.0664	0.0885	0.1107	0.1328	0.1549
q_1 [m]	0.6269	0.627	0.627	0.627	0.627	0.627	0.627	0.6271
q_2 [m]	0.8121	0.8121	0.8118	0.8114	0.811	0.8106	0.8101	0.8097
q_3 [m]	0.8123	0.8128	0.8132	0.8136	0.814	0.8144	0.8149	0.8153
t [s]	0.1771	0.1992	0.2214	0.2435	0.2656	0.2878	0.3099	…
q_1 [m]	0.6271	0.6271	0.6271	0.6271	0.6271	0.6272	0.6272	…
q_2 [m]	0.8093	0.8089	0.8084	0.8080	0.8076	0.8071	0.8067	…
q_3 [m]	0.8157	0.8161	0.8165	0.8169	0.8173	0.8177	0.8181	…
t [s]	35.9922	36.0143	36.0365	36.0586	36.0807	36.1029	36.1250	36.1471
q_1 [m]	0.627	0.627	0.627	0.627	0.627	0.627	0.627	0.627
q_2 [m]	0.8129	0.8126	0.8125	0.8125	0.8125	0.8125	0.8125	0.8125
q_3 [m]	0.8121	0.8124	0.8125	0.8125	0.8125	0.8125	0.8125	0.8125

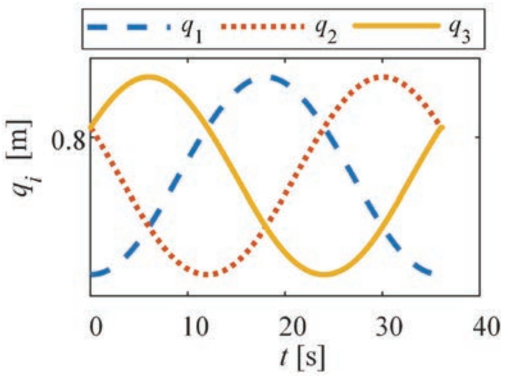

Fig. 10. *Branches' length variation law*

Fig. 12a shows the numerical distribution of the leg length difference of any two branch chains. It can be seen from the distribution of the difference results that the leg length has a periodic fluctuation with a fluctuation range of 0 m to 0.2164 m, and the distribution form of the difference results of different branch leg lengths is the same except for the phase differences. As shown in Fig. 12b, by comparing the result data of the leg length difference of data points with the threshold value of the over-limit setting, it can be seen that none of the data points in the trajectory exceed the limit.

Through the above simulation verification of the simplification algorithm of pose judgment, it is proved that the simplification algorithm of pose judgment can realize real-time judgment of the terminal pose state of the mechanism during the action process of a 1T2R power head. The result of pose judgment of this algorithm is found to be accurate. The active limit and preventive limit set according to the simplified algorithm of position and pose judgment can realize the limit protection function of 1T2R mechanism accurately and reliably and ensure the safe and reliable operation of the mechanism.

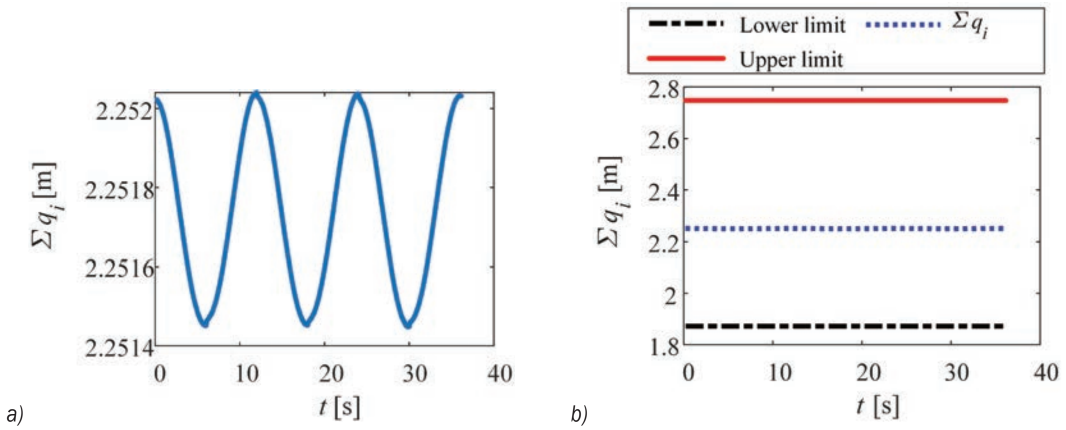

Fig. 11. *Branches' length summation distribution of data points; a) numerical distribution of the summation, and b) extra-limit judgment of summation*

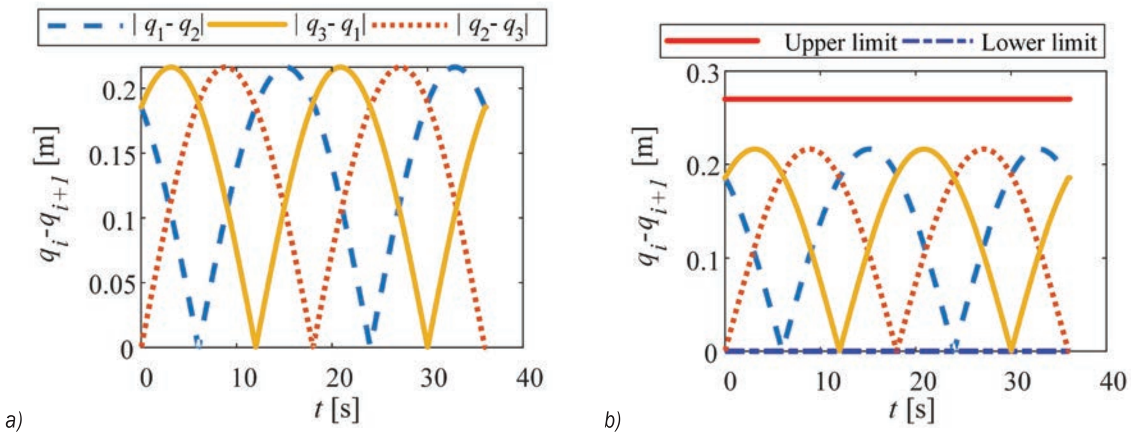

Fig. 12. *Distribution of branches' length difference; a) numerical distribution of the leg length difference, and b) extra-limit judgment of difference of leg length*

6 CONCLUSION

(1) This paper presents a simplified algorithm for the determination of the position and pose of 1T2R power head. Compared with the pose judgment method using the inverse solution model, it is estimated to be 99.42 % faster with no need to upgrade the original system. The simplified algorithm is easy to implement, efficient and reliable.
(2) The real-time limit protection of a 1T2R power head can be realized simply and reliably with the help of the simplification algorithm of position and pose judgment. Based on the software and hardware conditions of the existing numerical control system, this method can effectively solve the real-time limit protection problem of parallel machine tools by combining software and hardware and improve the operation safety of such topological machine tools.

7 ACKNOWLEDGEMENTS

The authors would like to acknowledge the financial supported from the National Natural Science Foundation of China (Grant No.51575385) and National Key Research and Development Program of China (Grant No.2019YFA0709004). The authors also acknowledge Key Laboratory of Mechanism Theory and Equipment Design of Ministry of Education and School of Mechanical Engineering the in Tianjin University for providing the experimental environment.

8 REFERENCES

[1] Guo, J.Z., Wang, D., Fan, R., Chen, W.Y. (2017). Design and workspace analysis of a 3-degree-of-freedom parallel swivel head with large tilting capacity. *Proceedings of the Institution of Mechanical Engineers, Part B: Journal of Engineering Manufacture*, vol. 231, no. 10, p. 1838-1849, **DOI:10.1177/0954405415607782**.
[2] Ni, Y., Zhou, H., Shao, C., Li, J. (2019). Research on the error averaging effect in a rolling guide pair. *Chinese Journal of Mechanical Engineering*, vol. 32, art. ID. 72, **DOI:10.1186/s10033-019-0386-y**.
[3] Cheng, G., Gu, W., Yu, J.-l., Tang, P. (2011). Overall structure calibration of 3-ucr parallel manipulator based on quaternion method. *Strojniški vestnik - Journal of Mechanical Engineering*, vol. 57, no. 10, p. 719-729, **DOI:10.5545/sv-jme.2010.167**.
[4] Ni, Y., Zhang, Y., Sun, K., Wang, H., Sun, Y. (2016). Interpolation control algorithm for a three-RPS parallel spindle head. *Proceedings of the Institution of Mechanical Engineers, Part I: Journal of Systems & Control Engineering*, vol. 230, no. 7, p. 661-671, **DOI:10.1177/0959651816645687**.
[5] Baizid, K., Ćukovic, S., Iqbal, J., Yousnadj, A., Chellali, R., Meddahi, A., Devedžić, G., Ghionea, I. (2016). IRoSim: Industrial robotics simulation design planning and optimization platform based on CAD and knowledgeware technologies. *Robotics and Computer-Integrated Manufacturing*, vol. 42, p. 121-134, **DOI:10.1016/j.rcim.2016.06.003**.
[6] Kumar, V. (1992). Characterization of workspaces of parallel manipulators. *Journal of Mechanical Design*, vol. 114, no. 3, p. 368-375, **DOI:10.1115/1.2926562**.
[7] Xu, P., Cheung, C.-F., Li, B., Ho, L.-T., Zhang, J.-F. (2017). Kinematics analysis of a hybrid manipulator for computer controlled ultra-precision freeform polishing. *Robotics and Computer-Integrated Manufacturing*, vol. 44, p. 44-56, **DOI:10.1016/j.rcim.2016.08.003**.
[8] Macho, E., Altuzarra, O., Amezua, E., Hernandez, A. (2009). Obtaining configuration space and singularity maps for parallel manipulators. *Mechanism & Machine Theory*, vol. 44, no. 11, p. 2110-2125, **DOI:10.1016/j.mechmachtheory.2009.06.003**.
[9] Huang, C.K., Tsai, K.Y. (2015). A general method to determine compatible orientation workspaces for different types of 6-DOF parallel manipulators. *Mechanism & Machine Theory*, vol. 85, no. p. 129-146, **DOI:10.1016/j.mechmachtheory.2014.11.011.**
[10] Zhang, D., Gao, Z. (2012). Optimal kinematic calibration of parallel manipulators with pseudoerror theory and cooperative coevolutionary network. *IEEE Transactions on Industrial Electronics*, vol. 59, no. 8, p. 3221-3231, **DOI:10.1109/TIE.2011.2166229**.
[11] Cui, G., Zhang, H., Zhang, D., Xu, F. (2015). Analysis of the kinematic accuracy reliability of a 3-DOF parallel robot manipulator. *International Journal of Advanced Robotic Systems*, vol. 12, no. 2, p. 15-26, **DOI:10.5772/60056**.
[12] Shao, J., Chen, W., Fu, X. (2015). Position, singularity and workspace analysis of 3-PSR-O spatial parallel manipulator. *Chinese Journal of Mechanical Engineering*, vol. 28, p. 437-450, **DOI:10.3901/CJME.2015.0122.018**.
[13] Kaloorazi, M.H.F., Masouleh, M.T., Caro, S. (2015). Determination of the maximal singularity-free workspace of 3-DOF parallel mechanisms with a constructive geometric approach. *Mechanism & Machine Theory*, vol. 84, p. 25-36, **DOI:10.1016/j.mechmachtheory.2014.10.003**.
[14] Zhang, D., Wei, B. (2017). Interactions and optimizations analysis between stiffness and workspace of 3-UPU robotic mechanism. *Measurement Science Review*, vol. 17, no. 2, p. 83-92, **DOI:10.1515/msr-2017-0011**.
[15] Gao, Z., Zhang, D. (2011). Workspace representation and optimization of a novel parallel mechanism with three-degrees-of-freedom. *Sustainability*, vol. 3, no. 11, p. 2217-2228, **DOI:10.3390/su3112217**.
[16] Zhu, C., Guan, L., Han, J., Wang, L. (2009). A new resolution of workspace problem of parallel machine tool. *IEEE International Conference on Automation and Logistics*, p. 1002-1007, **DOI:10.1109/ICAL.2009.5262566**.
[17] FarzanehKaloorazi, M.H., Masouleh, M.T., Caro, S. (2017). Collision-free workspace of parallel mechanisms based on an interval analysis approach. *Robotica*, vol. 35, no. 8, p. 1747-1760, **DOI:10.1017/S0263574716000497**.
[18] Majid, M.Z.A., Huang, Z., Yao, Y.L. (2000). Workspace analysis of a six-degrees of freedom, three-prismatic-prismatic-

spheric-revolute parallel manipulator. *International Journal of Advanced Manufacturing Technology*, vol. 16, p. 441-449, **DOI:10.1007/s001700050176**.

[19] Rouhani, E., Nategh, M.J. (2015). Workspace, dexterity and dimensional optimization of microhexapod. *Assembly Automation*, vol. 35, no. 4, p. 341-347, **DOI:10.1108/AA-03-2015-020**.

[20] Wan, J., Yao, J., Zhang, L., Wu, H. (2018). A weighted gradient projection method for inverse kinematics of redundant manipulators considering multiple performance criteria. *Strojniški vestnik - Journal of Mechanical Engineering*, vol. 64, no. 7-8, p. 475-487, **DOI:10.5545/sv-jme.2017.5182**.

[21] Khoukhi, A., Baron, L., Balazinski, M. (2009). Constrained multi-objective trajectory planning of parallel kinematic machines. *Robotics and Computer-Integrated Manufacturing*, vol. 25, no. 4-5, p. 756-769, **DOI:10.1016/j.rcim.2008.09.002**.

[22] Reveles, R.D., Pamanes, G.J.A., Wenger, P. (2016). Trajectory planning of kinematically redundant parallel manipulators by using multiple working modes. *Mechanism and Machine Theory*, vol. 98, p. 216-230, **DOI:10.1016/j.mechmachtheory.2015.09.011**.

[23] Dash, A.K., Chen, I.-M., Yeo, S.H., Yang, G. (2005). Workspace generation and planning singularity-free path for parallel manipulators. *Mechanism and Machine Theory*, vol. 40, no. 7, p. 776-805, **DOI:10.1016/j.mechmachtheory.2005.01.001**.

[24] Iqbal, J., Ullah, M.I., Khan, A.A., Irfan, M. (2015). Towards sophisticated control of robotic manipulators: An experimental study on a pseudo-industrial arm. *Strojniški vestnik - Journal of Mechanical Engineering*, vol. 61, no. 7, p. 465-470, **DOI:10.5545/sv-jme.2015.2511**.

[25] Manzoor, S., Islam, R.U., Khalid, A., Samad, A., Iqbal, J. (2014). An open-source multi-DOF articulated robotic educational platform for autonomous object manipulation. *Robotics and Computer-Integrated Manufacturing*, vol. 30, no. 3, p. 351-362, **DOI:10.1016/j.rcim.2013.11.003**.

[26] Alam, W., Mehmood, A., Ali, K., Javaid, U., Alharbi, S., Iqbal, J. (2018). Nonlinear control of a flexible joint robotic manipulator with experimental validation. *Strojniški vestnik - Journal of Mechanical Engineering*, vol. 64, no. 1, p. 47-55, **DOI:10.5545/sv-jme.2017.4786**.

[27] Mahmoodi, A., Sayadi, A.. (2015). Six-Dimensional space expression of workspace of six-DoF parallel manipulators using hyper spherical coordinates (HSC). *Advanced Robotics,* vol. 29, no. 23, p. 1527-1537, **DOI:10.1080/01691864.2015.1076345**.

Strojniški vestnik - Journal of Mechanical Engineering 68(2022)9, 571-582
DOI:10.5545/sv-jme.2022.274
Original Scientific Paper
Received for review: 2022-07-08
Received revised form: 2022-09-02
Accepted for publication: 2022-09-07

Nonlinear Vibration Analysis of Functionally Graded Porous Plates Reinforced by Graphene Platelets on Nonlinear Elastic Foundations

Xiaolin Huang* – Chengzhe Wang – Jiaheng Wang – Nengguo Wei
Guilin University of Electronic Technology, School of Architecture and Transportation Engineering, China

This paper presents a nonlinear vibration analysis of functionally graded graphene platelet (GPL) reinforced plates on nonlinear elastic foundations. Uniformly or non-uniformly distributed internal pores were present in the plates. Based on the modified Halpin-Tsai micromechanics model and the extended rule of mixture, the material properties were evaluated. The governing equations, coupled with the effect of nonlinear foundations, were derived by using the higher-order plate theory and general von Kármán-type equations. A two-step perturbation technique was employed to obtain the nonlinear frequency and transient response. After the present method was verified, the effects of pores, GPLs, and elastic foundations were investigated in detail. A new finding is that the influence of the porosity coefficient on the natural frequency and dynamic response is relevant to foundation parameters. Moreover, the influence of the nonlinear foundation parameter can be negligible.
Keywords: functionally graded porous nanocomposites, graphene platelets, pores, nonlinear elastic foundation, nonlinear vibration, transient response

Highlights
- *The material properties model of functionally graded (FG) graphene platelets reinforced plates is modified.*
- *A two-step perturbation technique for the nonlinear vibration of porous plates on nonlinear elastic foundations is presented.*
- *Some interesting conclusions about the effects of pores and nonlinear elastic foundations are drawn.*

0 INTRODUCTION

Due to the excellent load-carrying capacity with stronger bonding between the matrix and carbonaceous nanofillers [1] and [2], nano graphene platelets (GPL) are now increasingly used in many engineering fields, including aerospace, automobile, and civil engineering. It is necessary to study the dynamic characteristics of GPL-reinforced composite structures.

In recent years, few results about the dynamic behaviour for functionally graded (FG) plates reinforced with GPL have been reported [3]. Song et al. [4] employed the first-order shear deformation plate theory to study the free and forced vibrations of FG multilayer GPL/polymer plates. Their results illustrated that a small amount of GPL can lead to higher natural frequency and lower dynamic response. By using the finite element method, Zhao et al. [5] studied investigated the bending and free vibration behaviours of FG trapezoidal plates. Their results also illustrated that the transient deflection was decreased by using a small number of graphene platelets. Gholami and Ansari [6] investigated the nonlinear harmonically excited vibration of FG graphene-reinforced composite plates. They found that the nonlinear buckling was increased with the rise of GPLs weight fraction. Moreover, Wu et al. [7] studied the dynamic stability of FG nanocomposite plates subjected to thermal and mechanical loads.

Recently, a novel kind of graphene-reinforced nanocomposite was made by dispersing GPL into metal foams [8] to [10]. Due to the excellent mechanical and thermal properties, the novel composite materials have attracted some attention. Kittipornchai et al. [11] proposed a micromechanical model to estimate the typical properties of FG graphene reinforced nanocomposite, in which both GPL and internal pores are uniformly dispersed within each layer. Later, the model was employed to study the dynamic behaviour of graphene-reinforced nano-composite plates [12] and [13]. In these papers, the effect of internal pores has been discussed in detail, and the results showed that both pore volume fraction and the distribution of pores can affect the dynamic characteristics of porous structures.

In practical engineering, plates are sometimes rested on elastic foundations. Thus, a suitable model is needed to evaluate foundation interaction. The simplest is the Winkler model, in which a series of springs are used to calculate the tensile and compressed forces of elastic foundations. This model was later developed into the Pasternak model, in which a shear spring is added to estimate the shear forces of

*Corr. Author's Address: Guilin University of Electronic Technology, Jinji Road 1#, Guilin, China, xlhuang@guet.edu.cn

the Winkler foundations. Thereafter, the Pasternak model has been widely used to study the static and dynamic behaviours of plates on elastic foundations **[14]** to **[16]**. To estimate the nonlinear interaction between foundations and plates, some researchers recently presented a nonlinear foundation model. For example, Nath et al. **[17]**, Civalek **[18]** and Najafi et al. **[19]** studied the nonlinear dynamic behaviour of composite plates by using a nonlinear foundation model. Their results revealed that the nonlinear foundation parameter had a distinct influence on the dynamic characteristics.

As mentioned above, the number of studies focused on the dynamic behaviour of FG porous plates reinforced with GPL is still rather scarce. According to the authors' knowledge, no previous work has been done to study the nonlinear dynamic behaviour of FG graphene platelets reinforced porous plates on nonlinear elastic foundations. Hence, this paper attempts to study the nonlinear vibration of the plates. A modified material properties model is proposed, and the effects of internal pores and a nonlinear elastic foundation are discussed.

1 A POROUS NANO-COMPOSITE PLATE

As depicted in Fig. 1, a functionally graded graphene-reinforced porous plate (length a, width b, thickness h) on a nonlinear elastic foundation is taken into account. The origin of the coordinate system (X, Y, Z) is located at one corner of the middle plane of the plate. The Z-axis is perpendicular to the X-Y plane and points upwards. Three types of porosity distributions are considered (Fig. 2). "P-1" indicates that the largest-size pores are distributed in the middle. In contrast, "P-2" indicates that the largest-size pores are on the bottom and top surfaces. The symbol of even distribution is "P-3".

Unlike the material properties model presented by Kittipornchai et al. **[11]**, the present model is based on the volume fraction of pores, which are assumed to be:

$$V_P(Z) = \begin{cases} e_0 \cos(\pi Z / h), (P-1) \\ e_0^* \left[1 - \cos(\pi Z / h)\right], (P-2). \\ 1-\alpha, (P-3) \end{cases} \tag{1}$$

In the above equation, e_0, e_0^* $(0 \leq e_0(e_0^*) < 1$ and α denote the porosity coefficients for P−1, P−2, and P−3 distributions, respectively.

Yang's elastic modulus $E(Z)$ and shear elastic modulus $G(Z)$ of the porous plate can be expressed by using the rule of mixture:

$$E(Z) = E_0(1 - V_P),$$
$$G(Z) = G_0(1 - V_P), \tag{2}$$

where E_0 and G_0 are the corresponding variations of the graphene-reinforced nanocomposites without internal pores.

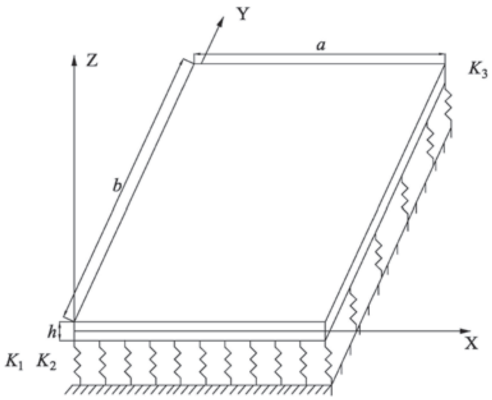

Fig. 1. *A functionally graded GPL-reinforced porous plate on a nonlinear elastic foundation*

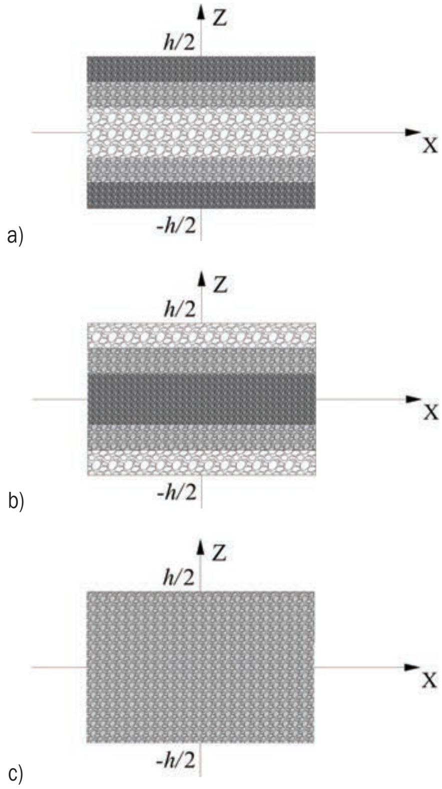

Fig. 2. *Three types of porosity distributions; a) P−1, b) P−2, and c) P−3*

Because the mass density $\rho(Z)$ cannot be calculated by using the rule of mixture **[11]**, it is assumed to be

$$\rho(Z)=\begin{cases}\rho_0\left[1-e_1\cos\left(\pi Z/h\right)\right],\left(P-1\right)\\ \rho_0\left[1-e_1^*(1-\cos\left(\pi Z/h\right)\right],\left(P-2\right),\\ \rho_0\alpha^{'},\left(P-3\right)\end{cases}\quad(3)$$

where ρ_0 is the mass density of the nanocomposites without pores. Coefficients e_1, e_1^* and α' are the mass density coefficients for the three types of porosity distributions.

For open-cell metal foams, the relationship between Yang's elastic modulus and mass density is $\frac{E(z)}{E_0}=\left(\frac{\rho(Z)}{\rho_0}\right)^2$ **[12]**. Hence, the coefficients e_1, e_1^* and α' can be estimated as

$$\begin{cases}1-e_1\cos\left(\frac{\pi Z}{h}\right)=\sqrt{1-e_0\cos\left(\frac{\pi Z}{h}\right)},\left(P-1\right)\\ 1-e_1^*\left(1-\cos\left(\frac{\pi Z}{h}\right)\right)=\sqrt{1-e_0^*\left(1-\cos\left(\frac{\pi Z}{h}\right)\right)},\left(P-2\right),\\ \alpha'=\sqrt{\alpha},\left(P-3\right)\end{cases}\quad(4)$$

It is assumed that the masses of all plates with different porosity distributions are equivalent. Hence, e_0^* and α can be calculated by

$$\begin{cases}\int_{-h/2}^{h/2}\sqrt{1-e_0^*(1-\cos\left(\frac{\pi Z}{h}\right)}dZ=\int_{-h/2}^{h/2}\sqrt{1-e_0\cos\left(\frac{\pi Z}{h}\right)}dZ\\ \int_{-h/2}^{h/2}\sqrt{\alpha}=\int_{-h/2}^{h/2}\sqrt{1-e_0\cos\left(\frac{\pi Z}{h}\right)}dZ\end{cases},\quad(5)$$

Based on the Halpin-Tsai micro-mechanical mode, the effective Young's elastic modulus E_0 can be expressed by

$$E_0=\frac{3}{8}\left(\frac{1+\xi_L\eta_L V_{GPL}}{1-\eta_L V_{GPL}}\right)E_m+\frac{5}{8}\left(\frac{1+\xi_W\eta_W V_{GPL}}{1-\eta_W V_{GPL}}\right)E_m,\quad(6)$$

where E_m and V_{GPL} are Young's elastic modulus of matrix and GPL volume fraction, respectively. The coefficients ξ_L, ξ_W, η_L and η_W are defined by

$$\eta_L=\frac{2a_{GPL}}{h_{GPL}},\quad \eta_L=\frac{2b_{GPL}}{h_{GPL}},$$
$$\eta_L=\frac{E_{GPL}/E_m-1}{E_{GPL}/E_m+\xi_L},\quad \eta_W=\frac{E_{GPL}/E_m-1}{E_{GPL}/E_m+\xi_W},\quad(7)$$

in which E_{GPL}, a_{GPL}, b_{GPL} and h_{GPL} are Young's modulus, average length, width, and thickness of graphene platelets, respectively.

Based on the rule of mixture, Poisson's ratio v, and mass density ρ_0 can be calculated as

$$v(Z)=v_{GPL}V_{GPL}+v_m(1-V_{GPL}),$$
$$\rho_0=\rho_{GPL}V_{GPL}+\rho_m(1-V_{GPL}),\quad(8)$$

where ρ_{GPL} is the mass density of GPL, and ρ_m and v_m are the mass density and Poisson's ratio of the matrix. The shear modulus G_0 can be obtained by

$$G_0=\frac{E_0}{2\left(1+v_0\right)}.\quad(9)$$

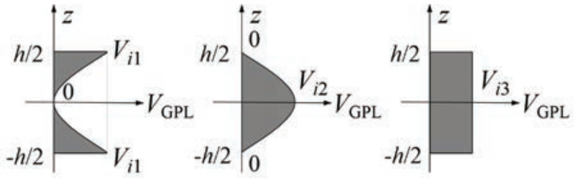

Fig. 3. *Three types of GPL dispersion patterns; a) G—1, b) G—2, and c) G—3*

As shown in Fig. 3, three types of GPL dispersion patterns (G-1, G-2, G-3) are considered. V_{GPL} is expressed as

$$V_{\mathrm{GPL}}(z)=\begin{cases}v_{i1}[1-\cos(\pi Z/h)]\left(G-1\right)\\ v_{i1}\cos(\pi Z/h)]\ \left(G-2\right),\\ v_{i3}\ \left(G-3\right)\end{cases}\quad(10)$$

where v_{i1}, v_{i2} and v_{i3} are the maximum value of V_{GPL}, i $(i=1,2,3)$ indicate the three types of porosity distributions. v_{i1}, v_{i2} and v_{i3} can be reckoned as follows:

$$V_{GPL}^T=\frac{W_{GPL}\rho_m}{W_{GPL}\rho_m+\rho_{GPL}-W_{GPL}\rho_{GPL}},\quad(11)$$

$$V_{GPL}^T\int_{-h/2}^{h/2}\frac{\rho(Z)}{\rho^*}dZ=\begin{cases}v_{i1}\int_{-h/2}^{h/2}\frac{\rho(Z)}{\rho^*}\left[1-\cos\left(\frac{\pi Z}{H}\right)\right]dZ\\ v_{i1}\int_{-h/2}^{h/2}\frac{\rho(Z)}{\rho^*}\cos\left(\frac{\pi Z}{H}\right)dZ\\ v_{i3}\int_{-h/2}^{h/2}\frac{\rho(Z)}{\rho^*}dZ\end{cases},\quad(12)$$

in which V_{GPL}^T and W_{GPL} are the total volume and weight fractions of GPL, respectively.

2 FORMULATIONS

2.1 Governing Equations

As noted by Civalek **[18]**, the effect of nonlinear plate-foundation interaction on the dynamic response of plates on elastic foundations must not be neglected. Therefore, the following three-parameter nonlinear foundation model is adopted:

$$R_f = \bar{K}_1\bar{W} - \bar{K}_2\left(\frac{\partial^4 \bar{W}}{\partial X^4} + 2\frac{\partial^4 \bar{W}}{\partial X^2 \partial Y^2} + \frac{\partial^4 \bar{W}}{\partial Y^4}\right) + \bar{K}_3\bar{W}^3, \quad (13)$$

where $\bar{K}_1$, $\bar{K}_2$, and $\bar{K}_3$ are Winkler, Pasternak, and nonlinear foundation parameters.

According to Reddy's higher-order thick plate theory [20], the displacements of the thick composite plate are assumed to be

$$\bar{u}_1 = \bar{U}(X,Y,t) + Z\left[\psi_1 - \frac{4}{3}\left(\frac{Z}{h}\right)^2\left(\psi_1 + \frac{\partial \bar{W}}{\partial X}\right)\right],$$

$$\bar{u}_2 = \bar{V}(X,Y,t) + Z\left[\psi_y - \frac{4}{3}\left(\frac{Z}{h}\right)^2\left(\psi_y + \frac{\partial \bar{W}}{\partial Y}\right)\right],$$

$$\bar{u}_3 = \bar{W}(X,Y,t), \quad (14)$$

in which $\bar{U}$, $\bar{V}$, $\bar{W}$, ψ_1 and ψ_2 are the displacements and rotations of a point (X, Y) on the mid-plane.

The von Karman strains associated with the displacement field in Eq. (14) can be stated as

$$\varepsilon_1 = \frac{\partial \bar{U}}{\partial X} + \frac{1}{2}\left(\frac{\partial \bar{W}}{\partial X}\right)^2 + Z\frac{\partial \psi_1}{\partial X} - \frac{4Z^3}{3h^2}\left(\frac{\partial \psi_1}{\partial X} + \frac{\partial^2 \bar{W}}{\partial Y^2}\right),$$

$$\varepsilon_2 = \frac{\partial \bar{V}}{\partial Y} + \frac{1}{2}\left(\frac{\partial \bar{W}}{\partial Y}\right)^2 + Z\frac{\partial \psi_2}{\partial Y} - \frac{4Z^3}{3h^2}\left(\frac{\partial \Psi_2}{\partial Y} + \frac{\partial^2 \bar{W}}{\partial Y^2}\right),$$

$$\varepsilon_3 = 0, \qquad \varepsilon_4 = \psi_2 + \frac{\partial \bar{W}}{\partial Y} - \frac{4Z^2}{h^2}\left(\psi_2 + \frac{\partial \bar{W}}{\partial Y}\right),$$

$$\varepsilon_5 = \Psi_1 + \frac{\partial \bar{W}}{\partial X} - \frac{4Z^2}{h^2}\left(\Psi_1 + \frac{\partial \bar{W}}{\partial X}\right),$$

$$\varepsilon_6 = \frac{\partial \bar{U}}{\partial Y} + \frac{\partial \bar{V}}{\partial X} + \frac{\partial \bar{W}}{\partial X}\frac{\partial \bar{W}}{\partial Y} + Z\left(\frac{\partial \psi_1}{\partial Y} + \frac{\partial \psi_2}{\partial X}\right)$$

$$-\frac{4Z^3}{3h^2}\left(\frac{\partial \psi_1}{\partial Y} + \frac{\partial \psi_2}{\partial X} + 2\frac{\partial^2 \bar{W}}{\partial X \partial Y}\right). \quad (15)$$

Based on Hook's law, the relationship between stresses and strains can be expressed as

$$\begin{bmatrix}\sigma_1\\ \sigma_2\\ \sigma_6\end{bmatrix} = \begin{bmatrix}\hat{Q}_{11} & \hat{Q}_{12} & 0\\ \hat{Q}_{12} & \hat{Q}_{22} & 0\\ 0 & 0 & \hat{Q}_{66}\end{bmatrix}\begin{bmatrix}\varepsilon_1\\ \varepsilon_2\\ \varepsilon_6\end{bmatrix},$$

$$\begin{bmatrix}\sigma_4\\ \sigma_5\end{bmatrix} = \begin{bmatrix}\hat{Q}_{44} & 0\\ 0 & \hat{Q}_{55}\end{bmatrix}\begin{bmatrix}\varepsilon_4\\ \varepsilon_5\end{bmatrix}, \quad (16)$$

in which

$$\hat{Q}_{11} = \hat{Q}_{22} = \frac{E}{1-\nu^2}, \quad \hat{Q}_{12} = \frac{\nu E}{1-\nu^2},$$

$$\hat{Q}_{16} = \hat{Q}_{26} = 0, \quad \hat{Q}_{44} = \hat{Q}_{55} = \hat{Q}_{66} = \frac{E}{2(1+\nu)}. \quad (17)$$

The in-plane forces $\bar{N}_i$, bending moment $\bar{M}_i$, higher-order bending moment $\bar{P}_i$, shear forces $\bar{Q}_i$, and higher-order shear forces $\bar{R}_i$ are

$$\left(\bar{N}_i, \bar{M}_i, \bar{P}_i\right) = \int_{-h/2}^{h/2}\sigma_i\left(1, Z, Z^3\right)\mathrm{d}Z, \quad (i = 1,2,6),$$

$$\left(\bar{Q}_2, \bar{R}_2\right) = \int_{-h/2}^{h/2}\sigma_4\left(1, Z^2\right)\,\mathrm{d}Z,$$

$$\left(\bar{Q}_1, \bar{R}_1\right) = \int_{-h/2}^{h/2}\sigma_5\left(1, Z^2\right)\,\mathrm{d}Z. \quad (18)$$

By using the Hamilton principle, the equations of motion for the plate can be derived as

$$\frac{\partial \bar{N}_1}{\partial X} + \frac{\partial \bar{N}_6}{\partial Y} = I_1\ddot{\bar{U}} + \bar{I}_2\ddot{\psi}_1 - I_4\frac{4}{3h^2}\frac{\partial \ddot{\bar{W}}}{\partial X},$$

$$\frac{\partial \bar{N}_6}{\partial X} + \frac{\partial \bar{N}_2}{\partial Y} = I_1\ddot{\bar{V}} + \bar{I}_2\ddot{\psi}_2 - I_4\frac{4}{3h^2}\frac{\partial \ddot{\bar{W}}}{\partial Y},$$

$$\frac{\partial \bar{Q}_1}{\partial X} + \frac{\partial \bar{Q}_2}{\partial Y} + \frac{\partial}{\partial X}\left(\bar{N}_1\frac{\partial \bar{W}}{\partial X} + \bar{N}_6\frac{\partial \bar{W}}{\partial Y}\right)$$

$$+\frac{\partial}{\partial Y}\left(\bar{N}_6\frac{\partial \bar{W}}{\partial X} + \bar{N}_2\frac{\partial \bar{W}}{\partial Y}\right) - \frac{4}{h^2}\left(\frac{\partial \bar{R}_1}{\partial X} + \frac{\partial \bar{R}_2}{\partial Y}\right)$$

$$+\frac{4}{3h^2}\left(\frac{\partial^2 \bar{P}_1}{\partial X^2} + 2\frac{\partial^2 \bar{P}_6}{\partial Y \partial Y} + \frac{\partial^2 \bar{P}_2}{\partial Y^2}\right) + R_f$$

$$= q + I_1\ddot{\bar{W}} - I_7\left(\frac{4}{3h^2}\right)^2\left(\frac{\partial^2 \ddot{\bar{W}}}{\partial X^2} + \frac{\partial^2 \ddot{\bar{W}}}{\partial Y^2}\right),$$

$$\frac{\partial \bar{M}_1}{\partial X} + \frac{\partial \bar{M}_6}{\partial Y} - \bar{Q}_1 + \frac{4}{h^2}\bar{R}_1 - \frac{4}{3h^2}\left(\frac{\partial \bar{P}_1}{\partial X} + \frac{\partial \bar{P}_6}{\partial Y}\right)$$

$$= \bar{I}_2\ddot{\bar{U}} + \bar{I}_3\ddot{\psi}_x - I_5\frac{4}{3h^2}\frac{\partial \ddot{\bar{W}}}{\partial X},$$

$$\frac{\partial \bar{M}_6}{\partial X} + \frac{\partial \bar{M}_1}{\partial Y} - \bar{Q}_2 + \frac{4}{h^2}\bar{R}_2 - \frac{4}{3h^2}\left(\frac{\partial \bar{P}_6}{\partial X} + \frac{\partial \bar{P}_2}{\partial Y}\right)$$

$$= \bar{I}_2\ddot{\bar{V}} + \bar{I}_3\ddot{\psi}_y - I_5\frac{4}{3h^2}\frac{\partial \ddot{\bar{W}}}{\partial Y}. \quad (19)$$

In Eq. (19), the constants I_j and $\bar{I}_j$ were given by Reddy [20]. The superposed dots indicate the differentiation with respect to time.

The strain compatibility equation is

$$\frac{\partial^2 \varepsilon_1^0}{\partial Y^2} + \frac{\partial^2 \varepsilon_2^0}{\partial X^2} - \frac{\partial^2 \varepsilon_6^0}{\partial X \partial Y} = \left(\frac{\partial^2 \bar{W}}{\partial X \partial Y}\right)^2 - \frac{\partial^2 \bar{W}}{\partial X^2}\frac{\partial^2 \bar{W}}{\partial Y^2}. \quad (20)$$

The in-plane forces $\bar{N}_i$ can be expressed by stress function $\bar{F}(X,Y,t)$:

$$\bar{N}_1 = \frac{\partial^2 \bar{F}}{\partial Y^2}, \quad \bar{N}_2 = \frac{\partial^2 \bar{F}}{\partial X^2}, \quad \bar{N}_6 = -\frac{\partial^2 \bar{F}}{\partial X \partial Y}. \quad (21)$$

By substituting Eqs. (18) and (21) into Eqs. (19) and (20), the governing equations of nonlinear vibration for the plate can be derived as follows:

$$\bar{l}_{11}(\bar{W}) - \bar{l}_{12}(\bar{\psi}_1) - \bar{l}_{13}(\bar{\psi}_2) + \bar{l}_{14}(\bar{F}) + R_f$$
$$= \bar{l}(\bar{W},\bar{F}) + \bar{l}_{17}(\ddot{\bar{W}}) + I_8 \frac{\partial \ddot{\bar{\psi}}_1}{\partial X} + I_8 \frac{\partial \ddot{\bar{\psi}}_2}{\partial Y} + q,$$
$$\bar{l}_{21}(\bar{F}) + \bar{l}_{22}(\bar{\psi}_1) + \bar{l}_{23}(\bar{\psi}_2) - \bar{l}_{24}(\bar{W}) = -\frac{1}{2}\bar{l}(\bar{W},\bar{W}),$$
$$\bar{l}_{31}(\bar{W}) + \bar{l}_{32}(\bar{\psi}_1) - \bar{l}_{33}(\bar{\psi}_2) + \bar{l}_{34}(\bar{F}) = I_9 \frac{\partial \ddot{\bar{W}}}{\partial X} + I_{10}\ddot{\bar{\psi}}_1,$$
$$\bar{l}_{41}(\bar{W}) - \bar{l}_{42}(\bar{\psi}_1) + \bar{l}_{43}(\bar{\psi}_2) + \bar{l}_{44}(\bar{F}) = I_9 \frac{\partial \ddot{\bar{W}}}{\partial Y} + I_{10}\ddot{\bar{\psi}}_2, \quad (22)$$

where the constants I_j ($j=8,9,10$), linear operators $\bar{l}_{ij}$ and nonlinear operator $\bar{l}$ were given by Shen **[21]** and Huang and Zheng **[22]**.

The four edges of the plate are assumed to be simply supported. The boundary conditions are expressed as

$$X = 0, \quad \text{a}: \bar{W} = \bar{\psi}_1 = \bar{M}_1 = \bar{P}_1 = \bar{N}_6 = 0,$$
$$Y = 0, \quad \text{b}: \bar{W} = \bar{\psi}_2 = \bar{M}_2 = \bar{P}_2 = \bar{N}_6 = 0. \quad (23)$$

2.2 Solution Procedure

To solve the nonlinear equations, Eqs. (22) and (23), we first introduce the following dimensionless parameters:

$$x = \frac{\pi X}{a}, y = \frac{\pi Y}{b}, z = \frac{Z}{h}, \beta = \frac{a}{b}, W = \frac{\bar{W}}{[D_{11}^* D_{22}^* A_{11}^* A_{22}^*]^{1/4}},$$
$$F = \frac{\bar{F}}{[D_{11}^* D_{22}^*]^{1/2}}, \quad (\psi_1, \psi_2) = \frac{(\bar{\psi}_1, \bar{\psi}_2)a}{\pi [D_{11}^* D_{22}^* A_{11}^* A_{22}^*]^{1/4}},$$
$$(K_1, K_2) = \frac{\left(\frac{a^4}{\pi^4}, \frac{a^2}{\pi^2}\right)}{D_{11}^*(\bar{K}_1, \bar{K}_2)}, K_3 = \frac{\bar{K}_3 a^4 \sqrt{D_{11}^* D_{22}^* A_{11}^* A_{22}^*}}{\pi^4 D_{11}^*},$$
$$\lambda_q = \frac{q a^4}{\pi^4 D_{11}^* [D_{11}^* D_{22}^* A_{11}^* A_{22}^*]^{1/4}}, \quad \tau = \frac{\pi t}{a}\sqrt{\frac{E_m}{\rho_m}}, \quad (24)$$

where the stiffness constants A_{ij}, B_{ij}, and D_{ij} are defined in the standard way **[20]**.

The dimensionless form of the equation (22) can be rewritten as

$$l_{11}(W) - l_{12}(\Psi_1) - l_{13}(\Psi_2) + \gamma_1 l_{14}(F) + K_1 W - K_2 \nabla^2 W$$
$$+ K_3 W^3 = \gamma_1 \beta^2 l(W,F) + l_{17}(\ddot{W}) + \gamma_2 \frac{\partial \ddot{\psi}_1}{\partial x} + \gamma_2 \beta \frac{\partial \ddot{\psi}_2}{\partial y} + \lambda_q,$$
$$l_{21}(F) + \gamma_2 l_{22}(\Psi_1) + \gamma_2 l_{23}(\Psi_2) - \gamma_{24} l_{24}(W) = -\frac{1}{2}\gamma_2 \beta^2 l(W,W),$$
$$l_{31}(W) + l_{32}(\psi_1) - l_{33}(\psi_2) + \gamma_1 l_{34}(F) = \gamma_4 \frac{\partial \ddot{W}}{\partial x} + \gamma_5 \ddot{\psi}_1, \quad (25)$$

where the constants $\gamma_i (i = 1, 2, ..., 5)$, the dimensionless operators l_{ij} and l can be seen in the previous work **[22]**.

The dimensionless form of the boundary conditions in Eq. (23) are also rewritten as:

$$\text{x} = 0, \quad \pi: W = \psi_1 = M_1 = P_1 = N_6 = 0,$$
$$y = 0, \quad \pi: W = \Psi_2 = M_2 = P_2 = N_6 = 0. \quad (26)$$

A two-step perturbation technique is employed to solve the nonlinear governing equations, Eq. (25). As the essence of this procedure, the asymptotic solution is supposed to be

$$W(x,y,\hat{\tau},\varepsilon) = \sum_{i=1} \varepsilon^i w_i(x,y,\hat{\tau}),$$
$$F(x,y,\hat{\tau},\varepsilon) = \sum_{i=1} \varepsilon^i f_i(x,y,\hat{\tau}),$$
$$\psi_x(x,y,\tilde{\tau},\varepsilon) = \sum_{i=1} \varepsilon^i \psi_{1i}(x,y,\hat{\tau}),$$
$$\psi_y(x,y,\hat{\tau},\varepsilon) = \sum_{i=1} \varepsilon^i \psi_{2i}(x,y,\hat{\tau}),$$
$$\lambda_q(x,y,\hat{\tau},\varepsilon) = \sum_{i=0} \varepsilon^i \lambda_i(x,y,\hat{\tau}). \quad (27)$$

In Eq. (27), the time parameter $\hat{\tau}$ ($\hat{\tau} = \varepsilon\tau$) is used to improve the perturbation procedure. Substituting Eq. (27) into Eqs. (25) and (26), then solving the perturbation equations step by step, the displacements W, ψ_x, ψ_y and stress function F can be obtained. The dimensionless transverse load λ_q can be derived as

$$\lambda_q(x,y,\tau) = [g_{41}\varepsilon w_1(\tau) + g_{43}\varepsilon \ddot{w}_1(\tau)]\sin mx \sin ny$$
$$+(\varepsilon w_1(\tau))^2 (g_{441}\cos 2mx + g_{442}\cos 2ny)$$
$$+g_{42}[\varepsilon w_1(\tau)]^3 (\sin mx \sin ny)^3 + o(\varepsilon^3). \quad (28)$$

In Eq. (28), it should be noted that $\hat{\tau}$ is replaced by τ. Multiplying Eq. (28) by $(\sin mx \sin ny)$ and integrating over the plate area, the following nonlinear ordinary differential equation can be obtained:

$$g_1 \frac{d^2(\varepsilon w_1)}{d\tau^2} + g_2(\varepsilon w_1) + g_3(\varepsilon w_1)^2 + g_4(\varepsilon w_1)^3 = \hat{\lambda}_q(\tau), \quad (29)$$

in which

$$\hat{\lambda}_q(\tau) = \frac{4}{\pi^2}\int_0^\pi \int_0^\pi \lambda_q(x,y,\tau)\sin mx \sin ny \, dxdy. \quad (30)$$

The nonlinear ordinary equation, Eq. (29) can be solved by using the Runge-Kutta iteration Scheme [23]. For the free vibration problem ($\lambda_q(\tau)=0$), the approximate nonlinear frequency can be derived as

$$\omega_{NL}=\left[\frac{g_{41}}{g_{43}}+\frac{9g_{42}g_{41}-10g_{44}^2}{12g_{41}g_{43}}A^2\right]^{1/2}, \quad (31)$$

where $A=\bar{W}_{\max}/h$ is the dimensionless vibration amplitude. If A=0, the dimensionless natural frequency is $\omega_L=\sqrt{g_{41}/g_{43}}$.

3 RESULTS AND DISCUSSION

In the section, the several dimensionless parameters are used as follows:

$$k_1=\frac{\bar{K}_w a^4}{D_m},\ k_2=\frac{\bar{K}_w a^2}{D_m},\ k_3=\frac{\bar{K}_3 a^4 h^2}{D_m},$$

$$D_m=\frac{E_m h^3}{12(1-v_m^2)},\ \Omega=\frac{\bar{\omega}_L a^2}{h}\sqrt{\frac{\rho_m}{E_m}},\ \widehat{\Omega}=\bar{\omega}_L h\sqrt{\frac{\rho_m}{E_m}}.$$

3.1 Comparison Studies

To verify the accuracy and effectiveness of the present method, two numerical examples are presented in this subsection.

Eam ple 1 The dimensionless fundamental frequencies of GPL-reinforced porous plates resting on elastic foundations are calculated and listed in Table 1. The material properties and dimensions of GPL are E_{GPL} = 1.01 TPa, ρ_{GPL} = 1062.5 kg/m³, v_{GPL} = 0.186, a_{GPL} = 2.5 µm, b_{GPL} = 1.5 µm, h_{GPL} = 1.5 nm. The material properties of the Matrix are E_m = 200 GPa, ρ_m = 8908 kg/m³, v_m = 0.31.

The geometrical parameters of the plate h = 0.05 m, a = b = 1.0 m. The GPL weight fraction and porosity coefficient are W_{GPL} = 5 %, e_0 = 0.4. It can be observed that the present results are close to those given by Gao et al. [13]. The maximum error is about 2.3 %. This is because Gao et al. [13] employed the classic plate theory and differential quadrature method to calculate the fundamental frequencies, which is different from the present method.

Eam ple 2. The dynamic response of a FG GPL reinforced plate is investigated in this example. The dispersion pattern of GPL is G−2. The plate is subjected to the explore load:

$$q(X,Y,t)=\begin{cases}P_m(1-t/t_p),\ 0\le t\le t_p\\ 0,\quad t<0 \text{ and } t>t_p\end{cases}, \quad (32)$$

where the peak pulse p_m is 500 kPa and the loading time t_p is 0.01 s. The material properties of the matrix are E_m = 3.0 GPa, ρ_m = 1290 kg/m³ and v_m = 0.34. The corresponding parameters of GPLs are E_{GPL}= 1.01 TPa, ρ_{GPL} = 1062.5 kg/m³ and v_{GPL} = 0.186. The geometric parameters of GPLs and the plate are a = b = 0.45, h = 0.045 m, a_{GPL} = 2.5 µm, b_{GPL} = 1.5 µm and h_{GPL} = 1.5 nm. The curves of central transient deflection versus time are depicted in Fig. 4. It is found that the present results are agreement with those given by Song et al. [4].

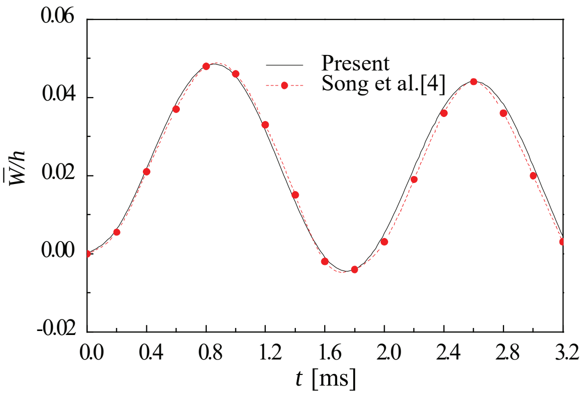

Fig. 4. *Comparison of the central transient deflection for an FG GPL-reinforced plate*

3.2 Parametric Studies

In what follows, the effects of material properties and foundation parameters are investigated in detail. The material and geometric parameters are the same as those in Example 1. Unless specially stated, the weight fraction W_{GPL} and pore coefficient e_0 are 5 % and 0.2. The dimensionless foundation parameters (k_1, k_2, k_3) are (50, 50, 50).

Table 1. *Comparison of dimensionless fundamental frequencies* $\widehat{\Omega}$ *for GPL reinforced plates resting on Winkler-Pasternak elastic foundations*

(k_1, k_2)	Method	P−1, G−1	P−2, G−1	P−1, G−3	P−2, G−3
(100, 100)	Ref. [13]	0.0637	0.0591	0.0745	0.0696
	present	0.0652	0.0603	0.0761	0.0710
	Error [%]	2.3	2.0	2.1	2.0

Tables 2 to 4 list the fundamental natural frequencies of the plate with different GPL dispersion pattern, porosity distribution, weight fractions W_{GPL}, porosity coefficients e_0 and foundation parameters (k_1, k_2). It can be seen that the natural frequency is increased with the rising weight fraction W_{GPL} and foundation parameters (k_1, k_2). The frequency for G−1 is higher than those for G−2 and G−3. This illustrates that G−1 can strengthen the plate more effectively than the other two patterns. Also, it can be seen that the frequency for P−1 is lower than those for P−2 and P−3. The fact demonstrated that P−1 can weaken the plate more seriously. In past studies [11] to [13], a conclusion was drawn that the natural frequency monotonously decreases with the increasing porosity coefficient. However, in the present case, the conclusion was correct only on P−2. On P−1 and P−3, the effect of the porosity coefficient

Table 2. *Dimensionless fundamental frequencies* Ω *for porosity distribution* P−1

GPL	e_0	$(k_1, k_2) = (0, 0)$ [wt%]			$(k_1, k_2) = (50, 0)$ [wt%]			$(k_1, k_2) = (50, 50)$ [wt%]		
		2.0	5.0	8.0	2.0	5.0	8.0	2.0	5.0	8.0
G−1	0.0	9.026	12.234	14.731	9.313	12.488	14.977	13.813	16.739	19.202
	0.2	8.970	12.149	14.623	9.280	12.422	14.889	14.055	16.952	19.400
	0.4	8.928	12.076	14.530	9.265	12.376	14.820	14.378	17.247	19.683
G−2	0.0	7.359	9.072	10.500	7.709	9.411	10.842	12.783	14.580	16.172
	0.2	7.311	8.997	10.404	7.687	9.363	10.773	13.056	14.848	16.440
	0.4	7.283	8.946	10.337	7.672	9.345	10.739	13.415	15.212	16.812
G−3	0.0	8.014	10.364	12.260	8.336	10.663	12.554	13.172	15.420	17.371
	0.2	7.982	10.323	12.210	8.328	10.643	12.526	13.444	15.690	17.643
	0.4	7.973	10.310	12.198	8.348	10.559	12.440	13.803	16.056	18.021

Table 3. *Dimensionless fundamental frequencies* Ω *for porosity distribution* P−2

GPL	e_0	$(k_1, k_2) = (0, 0)$ [wt%]			$(k_1, k_2) = (50, 0)$ [wt%]			$(k_1, k_2) = (50, 50)$ [wt%]		
		2.0	5.0	8.0	2.0	5.0	8.0	2.0	5.0	8.0
G−1	0.0	9.026	12.234	14.731	9.313	12.488	14.977	13.813	16.739	19.202
	0.2	8.283	11.328	13.526	8.617	11.534	13.822	13.629	16.313	18.595
	0.4	7.397	10.035	12.088	7.800	10.394	12.435	13.484	15.889	17.959
G−2	0.0	7.359	9.072	10.500	7.709	9.411	10.842	12.783	14.580	16.172
	0.2	6.775	8.382	9.719	7.180	8.774	10.112	12.765	14.486	16.017
	0.4	6.110	7.606	8.845	6.593	8.072	9.312	12.720	14.468	15.942
G−3	0.0	8.014	10.364	12.260	8.336	10.663	12.554	13.172	15.420	17.371
	0.2	7.337	9.488	11.223	7.712	9.836	11.566	13.072	15.155	16.977
	0.4	6.553	8.473	10.024	7.004	8.894	10.438	13.037	14.945	16.630

Table 4. *Dimensionless fundamental frequencies* Ω *for porosity distribution* P−3

GPL	e_0	$(k_1, k_2) = (0, 0)$ [wt%]			$(k_1, k_2) = (50, 0)$ [wt%]			$(k_1, k_2) = (50, 50)$ [wt%]		
		2.0	5.0	8.0	2.0	5.0	8.0	2.0	5.0	8.0
G−1	0.0	9.026	12.234	14.731	9.313	12.488	14.977	13.813	16.739	19.202
	0.2	9.026	12.234	14.731	9.313	12.488	14.977	13.813	16.739	19.202
	0.4	9.026	12.234	14.731	9.313	12.488	14.977	13.813	16.739	19.202
G−2	0.0	9.026	12.234	14.731	9.313	12.488	14.977	13.813	16.739	19.202
	0.2	9.026	12.234	14.731	9.313	12.488	14.977	13.813	16.739	19.202
	0.4	9.026	12.234	14.731	9.313	12.488	14.977	13.813	16.739	19.202
G−3	0.0	9.026	12.234	14.731	9.313	12.488	14.977	13.813	16.739	19.202
	0.2	8.721	11.821	14.233	9.039	12.103	14.506	13.898	16.719	19.317
	0.4	8.372	11.348	13.664	8.731	11.666	13.972	14.041	16.747	19.354

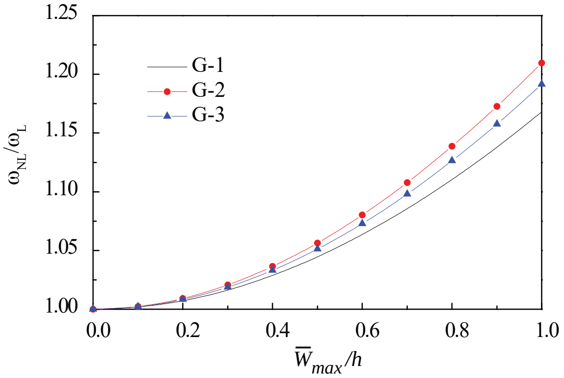

a)

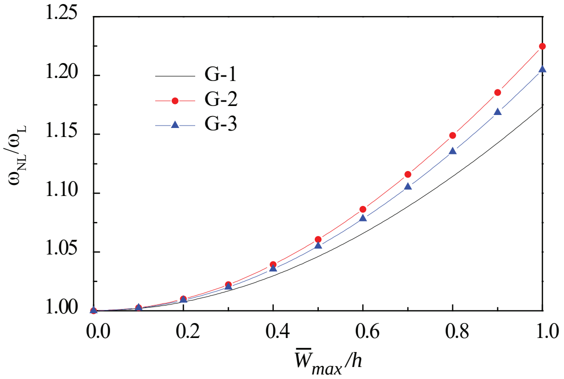

b)

Fig. 5. *Effect of GPL dispersion pattern on the frequency ratio; a) P–1,and b) P–2*

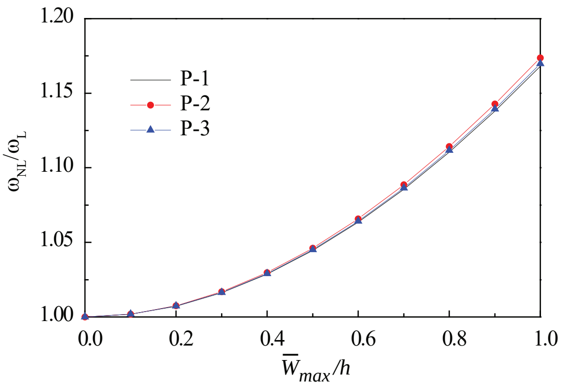

a)

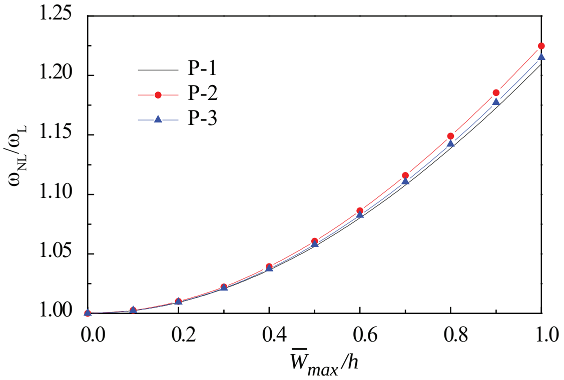

b)

Fig. 6. *Effect of porosity distribution on the frequency ratio, a) G–1, and b) G–2*

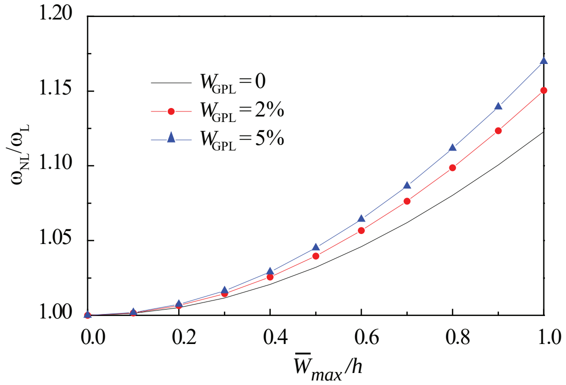

a)

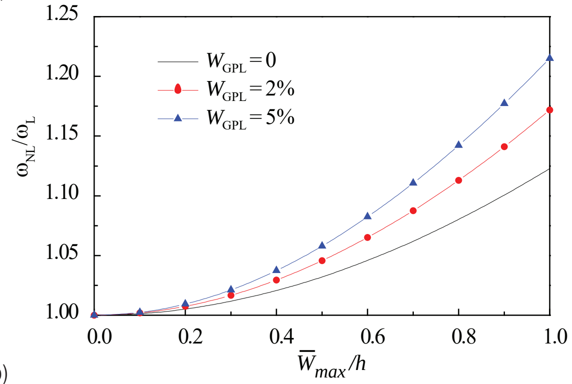

b)

Fig. 7. *Effect of GPL weight fractions on the frequency ratio; a) G–1/P-3, and b) G–2/P–3*

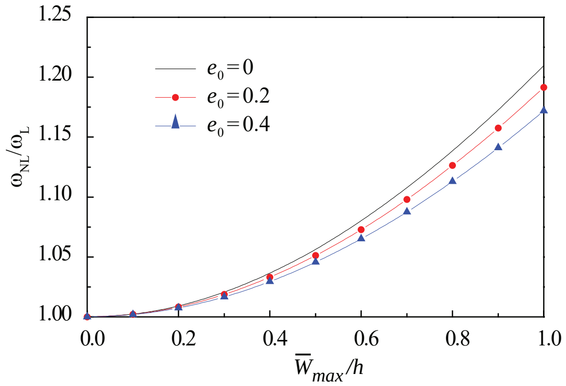

a)

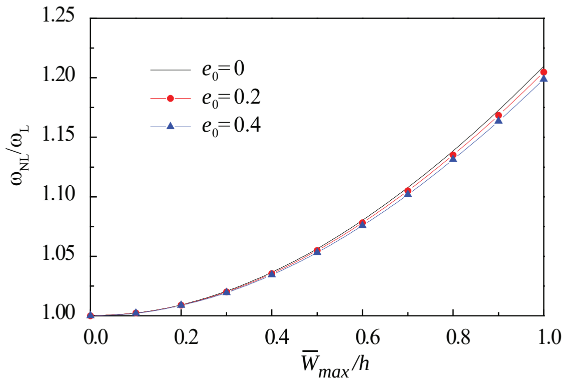

b)

Fig. 8. *Effect of porosity coefficient on the frequency ratio; a) G–3/P–1, and b) G–3/P–2*

is relevant to the values of foundation parameters (k_1, k_2). If foundation parameters are (50, 0) or (0, 0), the natural frequency is decreased. In contrast, the natural frequency for (50, 50) is increased.

Figs. 5 to 8 reveal the influences of GPL dispersion pattern, porosity distribution, GPL weight fraction W_{GPL}, and pore coefficient e_0 on the nonlinear to linear frequency ratio ω_{NL}/ω_L. As can be observed, the frequency ratio for G−2/P−2 is higher than those for other GPL and pore distributions. The frequency ratio is decreased as pore coefficient e_0 rises but rose with the increase of GPL fraction W_{GPL}.

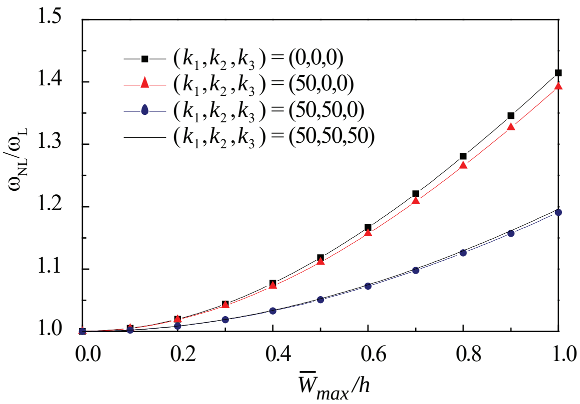

Fig. 9. Effect of elastic foundation on the frequency ratio for G−3/P−3

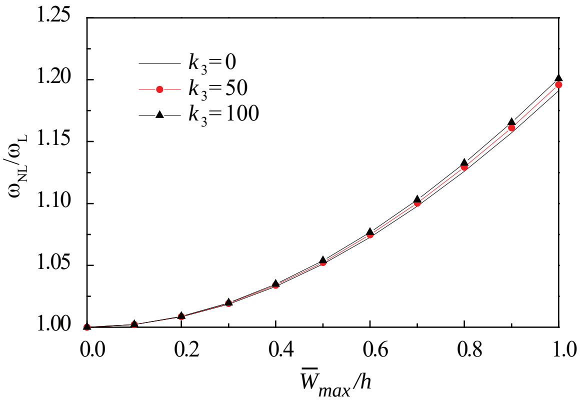

Fig. 10. *Effect foundation parameter k3 on the frequency ratio for G−3/P−3*

The effect of nonlinear elastic foundation parameters on frequency ratio is shown in Figs. 9 and 10. The two figures demonstrated that the frequency ratio reduces with the increasing parameters k_1 and k_2. However, the ratio rises as the nonlinear parameter k_3 increases.

The curves of central transient deflections and bending moments for different distributions of GPLs and pores are depicted in Figs. 11 and 12. It is found

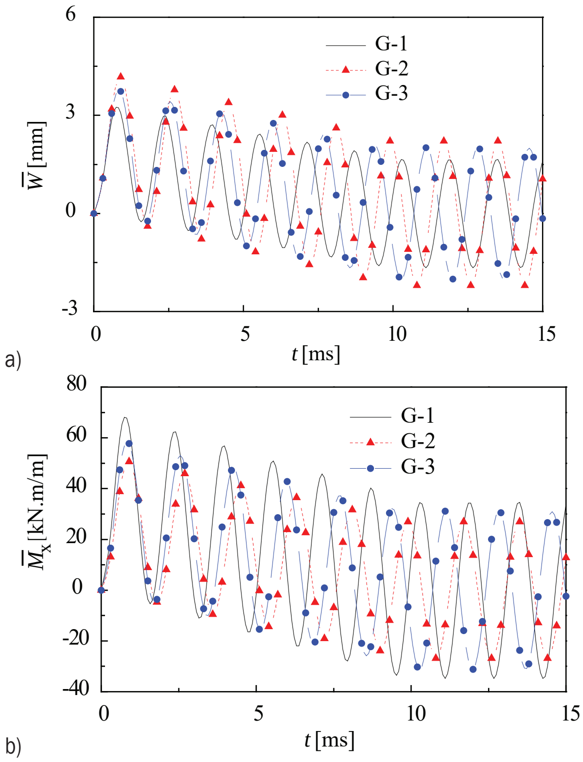

Fig. 11. *Effect of GPL dispersion patterns on the central transient responses for P−3; a) dynamic deflection, and b) dynamic bending moment*

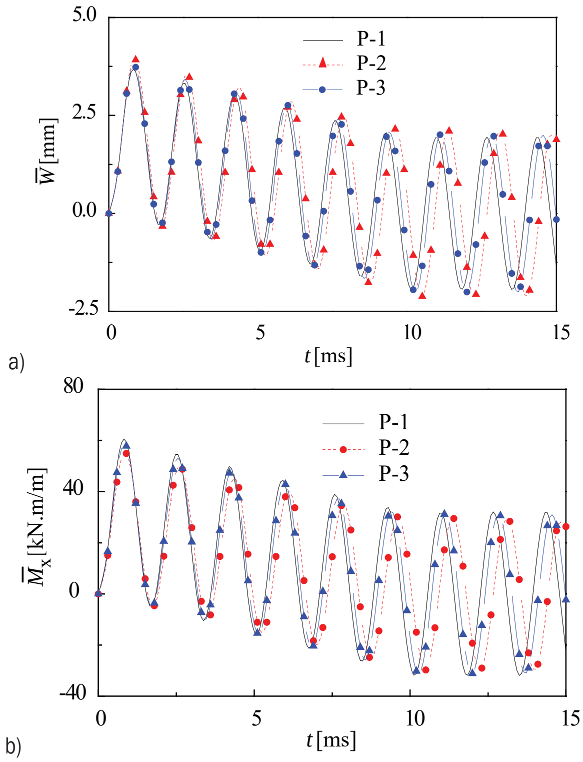

Fig. 12. *Effect of porosity distributions on the transient responses for G−3; a) dynamic deflection, and b) dynamic bending moment*

that the maximum dynamic deflection for G−2/P−2 is the largest among all patterns and distributions. In contrast, the amplitude of the dynamic bending moment for G−2/P−2 is the smallest.

The effects of GPL weight fraction W_{GPL} and pore coefficient e_0 on the transient responses is illustrated in Figs. 13 and 14. It is discerned that the rise of W_{GPL} reduces the amplitude of transient deflection, but increases the amplitude of bending moment. The maximum deflection increases by about 8 % as the porosity coefficient e_0 rises from 0.0 to 0.4. Therefore, a conclusion may be made that the effect of the porosity coefficient on the dynamic response can be negligible.

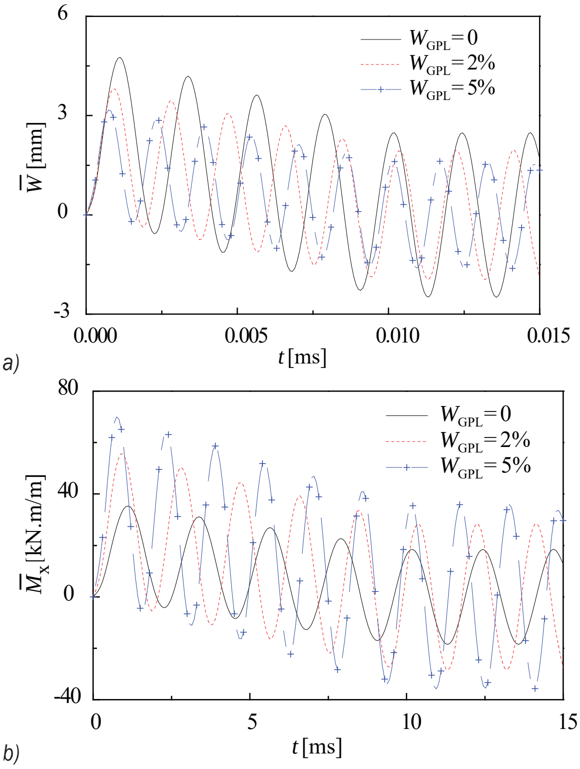

Fig. 13. *Effect of GPL weight fraction on the transient responses for P−1/G−1; a) dynamic deflection, and b) dynamic bending moment*

The effect of foundation parameters (k_1, k_2, k_3) on dynamic responses is presented in Fig. 15. As expected, Winkler and Pasternak elastic foundation parameters reduce the dynamic responses. The dynamic response for Pasternak elastic foundations (50, 50, 0) is very close to those for the nonlinear elastic foundations (50, 50, 50). Hence, a conclusion may be drawn that the effect of nonlinear foundation parameter k_3 on dynamic responses may be neglected, which is different from the statement mentioned by

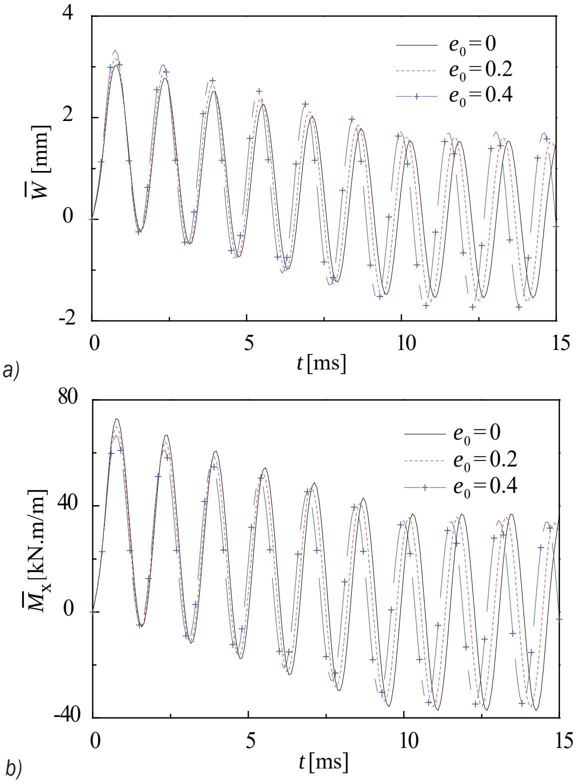

Fig. 14. *Effect of porosity coefficient on the transient responses for P−1/G−1; a) dynamic deflection, and b) dynamic bending moment*

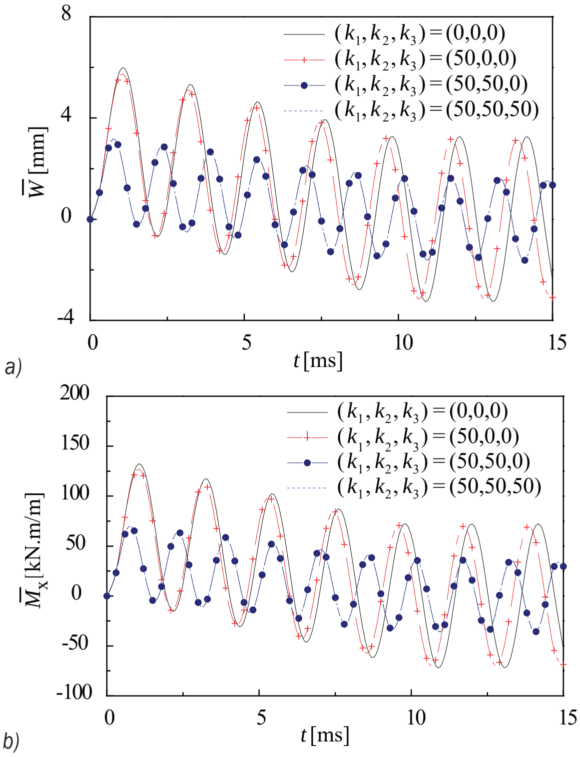

Fig. 15. *Effect of elastic foundation on the transient responses for P−1/G−1; a) dynamic deflection, and b) dynamic bending moment*

Civalek [18] and Najafi et al. [19]. They deemed that the nonlinear foundation parameter k_3 had a significant effect on the dynamic responses of laminated and FGM plates.

4 CONCLUSIONS

The present work presents a reliable and effective method to investigate the nonlinear free and forced vibrations of functionally graded GPL reinforced porous plates on nonlinear elastic foundations. The effects of internal pores, GPLs, and nonlinear elastic foundations are discussed in detail. Some interesting conclusions can be drawn from the numerical results:

1. Both GPL dispersion patterns and porosity distribution can affect the nonlinear vibrations and responses for porous plates. Furthermore, the effect of a GPL dispersion pattern is more significant than that of a porosity distribution.
2. The GPL weight fraction and foundation parameters k_1 and k_2 increase the natural frequency but decrease the nonlinear to linear frequency ratio and transient deflection.
3. The increase of porosity coefficient does not always lead to the rise of natural frequency and transient responses.
4. Nonlinear foundation parameters have insignificant effects on the nonlinear to linear frequency ratio and transient response.

5 ACKNOWLEDGEMENTS

The authors are thankful for the financial support of the National Natural Science Foundation of China [12162010] and the Natural Science Foundation of Guangxi [2021GXNSFAA 220087].

6 REFERENCES

[1] Yusufoglu, E., Avey, M. (2021). Nonlinear dynamic behavior of hyperbolic paraboloidal shells reinforced by carbon nanotubes with various distributions. *Journal of Applied and Computational Mechanics*, vol. 7, p. 913-921, **DOI:10.22055/JACM.2021.36043.2783**.

[2] Avey, M., Yusufoglu, E. (2020). On the solution of large-amplitude vibration of carbon nanotube-based double-curved shallow shells. *Mathematical Methods in the Applied Sciences*, vol. 8, p. 1-13, **DOI:10.1002/mma.6820**.

[3] Zhao, S.Y., Zhao, Z., Yang, Z.C., Ke, L.L., Kitipornchai, S., Yang, Y. (2020). Functionally graded graphene reinforced composite structures: A review. *Engineering Structures*, vol. 210, art. ID 110339, **DOI:10.1016/j.engstruct.2020.110339**.

[4] Song, M., Kittipornchai S., Yang, J., (2017). Free and forced vibrations of functionally graded polymer composite plates reinforced with graphene nanoplatelets. *Composite Structures*, vol. 159, p. 579-588, **DOI:10.1016/j.compstruct.2016.09.070**.

[5] Zhao, Z., Feng, C., Wang, Y., Yang, J. (2017). Bending and vibration of functionally graded trapezoidal nanocomposite plates reinforced with graphene nanoplatelets (GPLs). *Composite Structures*, vol. 180, p. 799-808, **DOI:10.1016/j.compstruct.2017.08.044**.

[6] Gholami R., Ansari R. (2018). Nonlinear harmonically excited vibration of third-order shear deformable functionally graded graphene platelet- reinforced composite rectangular plates. *Engineering and Structures*, vol. 156, p. 197-209, **DOI:10.1016/j.engstruct.2017.11.019**.

[7] Wu, H., Yang, J., Kittipornchai, S. (2018). Parametric instability of thermo-mechanically loaded functionally graded graphene reinforced nanaocomposite plates. *International Journal of Mechanical Science*, vol. 135, p. 431-440, **DOI:10.1016/j.ijmecsci.2017.11.039**.

[8] Bartolucci, S.F., Paras, J., Rafiee, M.A., Rafiee, J., Lee, S., Kapoor, D. (2011). Graphene-aluminum Nanocomposites. *Material Science and Engineering: A*, vol. 528, no. 27, p. 7933-7937, **DOI:10.1016/j.msea.2011.07.043**.

[9] Rashad, M., Pan, F., Tang, A., Asif, M. (2014). Effect of graphene nanoplatelets addition on mechanical properties of pure aluminum using a semi-powder method. *Progress of Natural Science: Materials International*, vol. 24, p. 101-108, **DOI:10.1016/j.pnsc.2014.03.012**.

[10] Wu, H.L, Yang, J., Kitipornchai, S. (2020). Mechanical analysis of functionally graded porous structures: A review. *International Journal of Structural Stability and Dynamics*, vol. 20, no. 13, art. ID 2041015, **DOI:10.1142/S0219455420410151**.

[11] Kittipornchai, S., Chen, D., Yang, J. (2017). Free vibration and elastic buckling of functionally graded porous beams reinforced with graphene platelets. *Material Design*, vol. 116, p. 656-665, **DOI:10.1016/j.matdes.2016.12.061**.

[12] Yang, J., Chen, D., Kittipornchai, S. (2018). Buckling and free vibration analysis of functionally graded graphene reinforced porous nanocomposite plates on Chebyshev-Ritz method. *Composite Structures*, vol. 193, p. 281-294, **DOI:10.1016/j.compstruct.2018.03.090**.

[13] Gao, K., Gao, W., Chen, D., Yang, J. (2018). Nonlinear vibration of functionally graded graphene platelets reinforced porous nanocomposite plates resting on elastic foundation. *Composite Structures*, vol. 204, p. 831-846, **DOI:10.1016/j.compstruct.2018.08.013**.

[14] Saidi, A.R., Bahaadini, R., Majidi-Mozafari, K. (2019). On vibration and stability of porous plates reinforced by graphene platelets under aerodynamic loading. *Composite Part B: Engineering*, vol. 163, p. 778-799, **DOI:10.1016/j.compositesb.2019.01.074**.

[15] Duc, N.D., Lee, J., Nguyen-Thoi, T., Thang, P.T. (2017). Static response and vibration of functionally graded carbon nanotube-reinforced composite rectangular plates resting on Winkler-Pasternak elastic foundations. *Aerospace Science and Technology*, vol. 68, p. 391-402, **DOI:10.1016/j.ast.2017.05.032**.

[16] Haciyev, V.C., Sofiyev, A.H., Kuruoglu, N. (2018). Free bending vibration analysis of thin bidirectionally exponentially graded orthortropic rectangular plates resting on two-parameter

elastic foundations. *Composite Structures*, vol. 184, p. 372-377, **DOI:10.1016/j.compstruct.2017.10.014**.

[17] Nath, Y., Prithviraju, M., Mufti, A.A. (2006). Nonlinear statics and dynamics of antisymmetric composite laminated square plates supported on nonlinear elastic subgrade. *Communication in Nonlinear Science and Numerical Simulation*, vol. 11, p. 340-354, **DOI:10.1016/j.cnsns.2004.11.003**.

[18] Civalek, Ö. (2013). Nonlinear dynamic response of laminated plates resting on nonlinear elastic foundations by the discrete singular convolution-differential quadrature coupled approaches. *Composite Part B: Engineering*, vol. 50, p. 171-179, **DOI:10.1016/j.compositesb.2013.01.027**.

[19] Najafi, F., Shojaeefard, M.H., Googarchin, H.S. (2016). Low-velocity impact response of functionally graded plates with nonlinear elastic foundation in thermal fields. *Composite Part B: Engineering*, vol. 10, p. 123-140, **DOI:10.1016/j.compositesb.2016.09.070**.

[20] Reddy, J.N. (1984). A refined nonlinear theory of plates with transverse shear deformation. *International Journal of Solids and Structures*, vol. 20, p. 881-896, **DOI:10.1016/0020-7683(84)90056-8**.

[21] Shen, H. (1997). Kármán-type equations for a higher-order shear deformation plate theory and its use in the thermal postbuckling analysis. *Applied Mathematics and Mechanics*, vol. 18, p. 1137-1152, **DOI:10.1007/BF00713716**.

[22] Huang, X.-L., Zheng, J.-J. (2003). Nonlinear vibration and dynamic response of simply supported shear deformable laminated plates on elastic foundations. *Engineering Structures*, vol. 25, p. 1107-1119, **DOI:10.1016/S0141-0296(03)00064-6**.

[23] Pearson, C.E. (1986). *Numerical Methods in Engineering & Science*. Van Nostrand Reinhold Company, New York.

Vsebina

Strojniški vestnik - Journal of Mechanical Engineering
letnik 68, (2022), številka 9
Ljubljana, september 2022
ISSN 0039-2480

Izhaja mesečno

Razširjeni povzetki (extended abstracts)

Strojniški vestnik - Journal of Mechanical Engineering 68(2022)9, SI 69

Prejeto v recenzijo: 2022-01-24
Prejeto popravljeno: 2022-04-25
Odobreno za objavo: 2022-06-13

Fraktalna geometrija reber za učinkovit hladilnik

Matjaž Ramšak
Univerza v Mariboru, Fakulteta za strojništvo, Slovenija

Fraktalna geometrija se v naravi srečuje v več oblikah in za različne namene. Omenimo tok krvi v razvejanem žilnem tokokrogu od glavnih žil do kapilar. V tehniškem žargonu je namen prekrvavitve tkiv prenos mase in tudi prenos toplote. Znano je, da mnogo evolucijskih rešitev prekaša današnje inženirske na mnogih področjih. Če to velja tudi za prenosnike toplote, bi morala obstajati fraktalna geometrija hladilnih reber, ki bi bila učinkovitejša od preprostih ravnih reber, ki so danes najpogosteje uporabljena za hlajenje naprav, kot pravi priljubljen slogan: obstaja prostor za izboljšave.

"Kako dolga je obala Britanije?" je vprašanje, ki ga je zastavil pionir fraktalne matematike Mandelbrot. Z uporabo vedno krajšega merila se dolžina obale povečuje v neskončnost. Če to logiko uporabimo za fraktalno oblikovana hladilna rebra, dobimo neskončno hladilno površino (A) in ob nič različni prestopnosti toplote (h) bi morali dobili neskončno toplotno moč ($\dot{Q}$), ki je produkt obeh $\dot{Q} = h\ A\ \Delta T$, pri čemer je ΔT konstantna temperaturna razlika. Cilj prispevka je preveriti omenjeno idejo z uporabo Richardsonove ekstrapolacije rezultatov numeričnih simulacij prestopa toplote iz zaporedja Kochovih snežink na tekočino pri variaciji dolžine osnovnega fraktalnega elementa od 1 do 0.

Za simulacijo prenosa toplote smo uporabili lasten program za Računalniško dinamiko tekočin na osnovi Metode robnih elementov (BEM). Katedra za energetiko in procesno strojništvo na Fakulteti za strojništvo ima že 40 letno tradicijo razvoja BEM za prenosne pojave v trdninah in tekočinah. V tem prispevku uporabljamo BEM z mešanimi elementi in s tehniko podobmočij v limitnem režimu, kjer je vsako podobmočje sestavljajo 3 robni elementi za trikotno podobmočje in 4 za štirikotno. Na tak način se izognemo polni nesimetrični matriki, ki je glavna hiba BEM in dobimo prazno matriko kot pri metodi končnih elementov. Razviti programom smo uspešno validirali in objavili revizijo Benchmark primera vezanega prenosa toplote v trdnini in tekočini.

Ideja o neskončni toplotni moči fraktalnih hladilnih reber je seveda naivna, kar je potrdil tudi pričujoči numerični eksperiment. Za neskončno velikost fraktalne površine ($A \to \infty$) smo izračunali vrednost toplotne prestopnosti enako nič ($h \to 0$). Limita toplotne moči, ki je produkt velikosti površine in toplotne prestopnosti, je končna vrednost ($\dot{Q}$ = konstanta). Slednje je splošno znano dejstvo. Dejstvo je tudi, da je vsaka površina hrapava najsi je fraktalne ali kakšne druge oblike in da je prestop toplote iz trdne stene na tekočino pravzaprav difuzija toplote.

Zamišljeni fraktalni hladilnik v obliki Kochove snežinke ni konkurenčen ravnim hladilnim rebrom. Nadaljnje raziskave v tej smeri nimajo pravega smisla.

Ključne besede: fraktalno hladilno telo, LED in CPU hlajenje, konjugirani prenos toplote, laminarni tok, metoda robnih elementov, Kochova snežinka

*Naslov avtorja za dopisovanje: Univerza v Mariboru, Fakulteta za strojništvo, Smetanova 11, 2000 Maribor, Slovenija, matjaz.ramsak@um.si

Strojniški vestnik - Journal of Mechanical Engineering 68(2022)9, SI 70

Prejeto v recenzijo: 2022-01-17
Prejeto popravljeno: 2022-07-07
Odobreno za objavo: 2022-08-26

Uporaba metod MTPA in MSM za analizo prenosa vibracij po manipulatorju za vrtanje sidrnih vrtin s 6 prostostnimi stopnjami

Youyu Liu[1,3] – Liteng Ma[1,3,*] – Siyang Yang[1,3] – Liang Yuan[2] – Bo Chen[1,3]
[1]Državni laboratorij za senzoriko in pametno upravljanje visokotehnološke opreme, Ministrstvo za izobraževanje, Kitajska
[2] Wuhu Yongyu avtomobilska industrija, Tehnološki oddelek, Kitajska
[3]Politehnika Anhui, Šola za strojništvo, Kitajska

Strojno vrtanje sidrnih vrtin za podporne sisteme v premogovnikih odpravlja težko ročno delo, povzroča pa močne vibracije, ki se od stroja za sidranje po manipulatorju prenašajo na podstavek. Članek obravnava mehanizem prenosa vibracij po manipulatorju med vrtanjem sidrnih vrtin.

TPA je eno od orodij za preučevanje prenosa vibracij, kot so tudi OTPA, GTDT in ITPA. Obstajajo določene omejitve, npr. zaradi motečih dejavnikov, kot sta sklapljanje vzbujanj in šum, manevrirna sposobnost pa je slaba zaradi serijskega sistema z mnogimi podstrukturami.

Na podlagi večstopenjske analize prenosne poti (MTPA) in metode modalne superpozicije (MSM) je bil postavljen model prenosa vibracij za podsistem, sestavljen iz zgibov manipulatorja s šestimi prostostnimi stopnjami (DOF). Določena je bila matrika njegovega frekvenčnega odziva. Izpeljano je bilo vzbujanje stroja za sidranje v šestih prostostnih stopnjah. Vzbujalna sila stroja za sidranje, ki se po manipulatorju prenaša na podstavek, je bila analizirana z Jacobijevo matriko sil in na ta način so bile določene zunanje obremenitve podstavka. Primer iz inženirske prakse kaže, da si amplitude prostostnih stopenj podstavka sledijo v naslednjem vrstnem redu od večjih proti manjšim: upogibne vibracije (komponenta 1), vzdolžne vibracije, torzijske vibracije, upogibne vibracije (komponenta 2), rotacijske vibracije okrog osi z in rotacijske vibracije okrog osi y. Na podstavku se pojavljajo predvsem upogibne vibracije.

(1) Na podlagi metod MTPA in MSM je bil postavljen matematični model prenosa vibracij po manipulatorju pri vrtanju sidrnih vrtin. Izpeljana je bila matrika frekvenčnega odziva podsistemov na vzbujanje v več prostostnih stopnjah. Na podlagi določitve zunanjih vzbujalnih obremenitev je mogoče izračunati funkcijo frekvenčnega odziva vsake prostostne stopnje v točki odziva po matematičnem modelu, ki je univerzalen za serijske sisteme.
(2) Znotraj frekvenčnega območja vzbujanja stroja za sidranje (0 Hz do 200 Hz) se nahajajo frekvenčna območja z največjimi vrednostmi vibracij v šestih prostostnih stopnjah posameznih podsistemov [191,3, 197,4] Hz, [88,95, 91,55] Hz, [42,19, 91,77] Hz, [135,2, 137,8] Hz, [178,8, 187,4] Hz in [73,24, 95,54] Hz. Vibracijski odziv je največji v omenjenih frekvenčnih območjih, resonanci pa se je mogoče izogniti s spremembo vzbujalne frekvence stroja za sidranje.
(3) Primer iz inženirske prakse kaže, da si amplitude prostostnih stopenj podstavka sledijo v naslednjem vrstnem redu od večjih proti manjšim: upogibne vibracije (komponenta 1) ($2{,}12\times10^{-2}$ m) pri 90 Hz, vzdolžne vibracije ($1{,}65\times10^{-2}$ m) pri 45 Hz, torzijske vibracije (9×10^{-3} m) pri 190 Hz, upogibne vibracije (komponenta 2) ($8{,}06\times10^{-3}$ m) pri 180 Hz, rotacijske vibracije okrog osi z ($2{,}46\times10^{-4}$ m) pri 180 Hz, rotacijske vibracije okrog osi y ($2{,}08\times10^{-4}$ m) pri 180 Hz. Na podstavku se pojavljajo predvsem upogibne vibracije.
(4) Izkazalo se je, da resonanca nastopi med komponentama upogibnih vibracij pri frekvencah 90 Hz in 180 Hz, resonanca med komponentama rotacijskih vibracij okrog osi y in z pa je najbolj verjetna med frekvencama 180 Hz in 181 Hz.

Predlagana teorija prenosa vibracij po manipulatorju za vrtanje sidrnih vrtin s šestimi prostostnimi stopnjami bo lahko teoretična osnova za razvoj tehnik blaženja vibracij in konstruiranje blažilnikov.

Na podlagi metod MTPA in MSM je bil postavljen matematični model prenosa vibracij po manipulatorju za vrtanje sidrnih vrtin s šestimi prostostnimi stopnjami. Zunanja obremenitev v točki odziva na podstavku manipulatorja je bila analizirana z Jacobijevo matriko sil. Določena sta bila vibracijski odziv po vsaki prostostni stopnji podstavka in resonančna frekvenca. Študija primera iz inženirske prakse je pokazala, da je podstavek izpostavljen predvsem upogibnim vibracijam.

Ključne besede: manipulator, stroj za sidranje, večstopenjska analiza prenosne poti, metoda modalne superpozicije, prenos vibracij, Jacobijeva matrika sil

*Naslov avtorja za dopisovanje: Wuhu Yongyu avtomobilska industrija, Tehnološki oddelek, Wuhu, Kitajska, ahpulyy@163.com

Strojniški vestnik - Journal of Mechanical Engineering 68(2022)9, SI 71

Prejeto v recenzijo: 2022-04-05
Prejeto popravljeno: 2022-08-02
Odobreno za objavo: 2022-08-10

Utrjevanje funkcijskih površinskih slojev in izboljševanje obrabne obstojnosti strojnih elementov iz malooglјičnega jekla s plazemsko elektrolizo

Kuat Kombayev[1] - Murat Muzdybayev[1] - Alfiya Muzdybayeva[1] -
Dinara Myrzabekova[1] - Wojciech Wieleba[2] - Tadeusz Leśniewski[2]
[1] Državna tehniška univerza vzhodnega Kazahstana, Oddelek za tehnološko opremo in transport, Republika Kazahstan
[2] Znanstveno-tehniška univerza v Wroclawu, Fakulteta za strojništvo, Poljska

Plazemska elektroliza (EPP) je najučinkovitejši postopek za utrjevanje delov vrtalne opreme. V pričujoči raziskavi je bila opravljena eksperimentalna identifikacija parametrov tehnološkega procesa utrjevanja jekla 18CrNi3Mo-Sh s plazemsko elektrolizo. Tehnologija utrjevanja površinskega sloja strojnih elementov iz malooglјičnega jekla je možna alternativa oglјičenju in kaljenju (postopek, ki se uporablja pri kotalnih dletih). Predlagana metoda za utrjevanje površinskega sloja delov iz malooglјičnega jekla vključuje segrevanje dela do temperature 930 °C do 940 °C, ki mu sledi naoglјičenje površine z ogljikovimi ioni do globine 2 mm in nato kaljenje na temperaturi 800 °C do 820 °C. Za postopek je značilno plazemsko segrevanje površine dela, ki je potopljen v tekočem elektrolitu do globine 4 mm do 6 mm.

Za preverjanje učinkovitosti utrjevanja po postopku proizvajalca kotalnih dlet JSC »VKMZ« in po metodi EPP sta bili obdelani dve seriji preizkušancev. Rastrska elementna analiza obdelane katodne površine je pokazala, da EPP poleg utrjevanja povzroči tudi kemično modifikacijo površinskega sloja komponente. EPP omogoča izdelavo utrjenih slojev debeline 1000 µm do 1700 µm. Ugotovljeno je bilo 1,5- do 2-kratno povečanje mikrotrdote v primerjavi z začetnim stanjem. Za mikrostrukturo obdelane površine jeklenih preizkušancev je značilen temen modificirani površinski sloj. Fina igličasta struktura martenzitnega izvora pod temnim slojem se spremeni v začetno perlitno-feritno mikrostrukturo.

Prednost utrjevanja s plazemsko elektrolizo je v majhni porabi energije, visoki hitrosti utrjevanja ter zmožnosti lokalne obdelave površin, zlasti pri večjih delih zahtevnih oblik. Predlagana metoda za obdelavo površin po postopku EPP ne zagotavlja le gladkih površin, temveč tudi izboljša delovne lastnosti komponent, npr. obrabno obstojnost. Ta je bila ocenjena z izgubo mase preizkušanca na enoto časa v obrabnih preizkusih z drsenjem po abrazivnem disku brez maziva. Mikrorelief obrabljene površine jeklenega preizkušanca je pokazal najmanjšo abrazivno obrabo pri delu, obdelanem po postopku EPP. Pri finozrnatem martenzitu se na površini oblikuje močna mikrostruktura, ki je ni uničila niti močna abrazivna obraba (med eksperimenti) in ki tako preprečuje razsežnejše poškodbe. Jekleni preizkušanec, ki je bil toplotno obdelan po postopku JSC »VKMZ«, je inferioren v primerjavi s preizkušancem, utrjenim po postopku EPP. Eksperimenti so tako potrdili, da je z reguliranjem postopka EPP mogoče vplivati na kakovost utrjevanja jekel, pridobiti obrabno obstojne površine in znatno izboljšati produktivnost EPP. Tehnološki postopek EPP je obvladljiv ter primeren za praktično uvedbo razvite tehnologije v proizvodnji.

Ključne besede: malooglјično jeklo, utrjevanje, plazemska elektroliza, prevleke, inženiring površin, obrabna obstojnost

*Naslov avtorja za dopisovanje: Znanstveno-tehniška univerza v Wroclawu, Fakulteta za strojništvo,
Wybrzeże Wyspiańskiego 27, 50-370 Wrocław, Poljska, tadeusz.lesniewski@pwr.edu.pl

Strojniški vestnik - Journal of Mechanical Engineering 68(2022)9, SI 72

Prejeto v recenzijo: 2022-05-04
Prejeto popravljeno: 2022-07-05
Odobreno za objavo: 2022-08-17

Eksperimentalna raziskava v industriji kot prispevek k razvoju eksperimentalnega modela vibracij kotalnih ležajev

Mateusz Wrzochal[1], Stanisław Adamczak[1], Grzegorz Piotrowicz[2], Sylwester Wnuk[2]
[1]Tehniška univerza v Kielcah, Poljska
[2]Polish Bearing Factory, Kraśnik SA, Poljska

V odsotnosti fizičnih simulatorjev za kotalne ležaje obstaja realna potreba po razvoju matematičnih modelov za čim točnejšo aproksimacijo delovanja kotalnih ležajev.

Za dosedanje teoretične študije z matematičnimi modeli kotalnih ležajev so značilne velike poenostavitve in obravnava le nekaterih dejavnikov, ki vplivajo na raven vibracij ležajev. Trenutno ni matematičnega modela, ki bi upošteval večino realnih dejavnikov, pri analizi vibracij pa je največkrat prezrta kontaminacija ležajev in masti. Poleg tega večina analitičnih modelov obravnava ležaje z izrazitimi napakami, ki bi nastale le v primeru dolgega obratovanja ali neprimernih obratovalnih pogojev. Tovrstni modeli v razpoložljivi svetovni literaturi zato niso univerzalni in niso primerni za uporabo v industrijski praksi. Potreben je eksperimentalni model za popolnoma nove ležaje.

Teoretični modeli vibracij ležajev in eksperimentalni preizkusi običajno prezrejo čistočo v notranjosti ležajev. Matematična simulacija kontaminacije je prvič zelo težavna, drugič pa eksperimentalne študije obravnavajo visokoamplitudne komponente v nizko- in srednjefrekvenčnem območju, ki so posledica poškodb ali geometrije površin. Da bi razkrili glavne vzroke za izmet, je bil šest mesecev opazovan proces proizvodnje desetih različnih vrst kotalnih ležajev. Preizkušenih je bilo skupaj 46.811 ležajev. Vsi izdelki, ki so bili izločeni po meritvah vibracij v okviru kontroli kakovosti, so bili skrbno pregledani. Vzroki napak na izdelkih so bili razvrščeni v štiri kategorije.

Za pripravo eksperimentalnega modela kotalnega ležaja je treba opraviti vrsto preizkusov, ki upoštevajo vse dejavnike vpliva na stopnjo vibracij, in vključiti tudi večkriterijsko statistično analizo. Model mora upoštevati nepopolnosti, ki vplivajo na diskretne vibracije (odstopanja oblike, velikosti in položaja, čezmerna valovitost, mikrovalovitost in hrapavost), ter predvsem prisotnost trdnih delcev v ležaju, ki je neizogibno povezana s proizvodnim procesom.

Čeprav so bile študije opravljene na zelo veliki skupini različnih ležajev, specifičnih vzrokov kontaminacije ne opisujejo. Njihovo poznavanje bi lahko omogočilo izboljševanje tehnoloških procesov izdelave kotalnih ležajev.

Avtorji članka nameravajo v prihodnje opraviti podrobnejše raziskave in analizo vpliva stopnje kontaminacije kotalnih ležajev na vibracije ter preveriti stopnjo zaznavanja tovrstnih neskladnosti z merilno opremo in metodami, ki jih uporabljajo v industriji ležajev. Z načrtovanimi preizkusi bo mogoče napovedati vpliv čistoče ležajev na omejevanje vibracij.

Neupoštevanje čistoče v matematičnih modelih in eksperimentalnih raziskavah ni upravičeno. Proizvajalci ležajev, ki se ukvarjajo z razvojem preciznih ležajev, morajo ob naložbah v proizvodnjo razviti tudi procese za zagotavljanje tehnične čistoče. Na končno stopnjo tehnične čistoče komponent, ki se vgrajujejo v končne sestave, ne vplivata le proizvodni proces in pranje. Ključnega pomena so tudi stopnja čistoče v prostorih, kjer potekajo proizvodne in montažne operacije, ter embalaža in ukrepi za preprečitev ponovne kontaminacije.

Ključne besede: kotalni ležaji, vibracije, čistoča ležajev, kontrola kakovosti

*Naslov avtorja za dopisovanje: Tehniška univerza v Kielcah, al. Tysiąclecia Państwa Polskiego 7, 25-314 Kielce, Poljska, mwrzochal@tu.kielce.pl

Strojniški vestnik - Journal of Mechanical Engineering 68(2022)9, SI 73

Prejeto v recenzijo: 2022-02-21
Prejeto popravljeno: 2022-07-01
Odobreno za objavo: 2022-07-11

Varovalna metoda za omejevanje delovnega prostora paralelne delovne glave

Yanbing Ni[1,*] – Wenliang Lu[2] – Shilei Jia[2] – Chenghao Lu[2] – Ling Zhang[2] – Yang Wen[1]
[1] Univerza v Tianjinu, Fakulteta za strojništvo, Kitajska
[2] Državni laboratorij za teorijo mehanizmov in konstrukcijo, Ministrstvo za šolstvo, Kitajska

Paralelna delovna glava 1T2R je topološko zasnovana kot paralelni mehanizem z eno translacijsko in dvema rotacijskima (1T2R) prostostnima stopnjama. Lega konca mehanizma znotraj delovnega prostora je določena z nelinearno preslikavo delovanja servomotorja v prostor sklepov. Informacije o legi konca mehanizma je mogoče pridobiti samo s kompleksnim modeliranjem in izračuni.

Ključni problem, ki ga je treba nujno razrešiti za točno in realnočasovno omejevanje gibanj tovrstnih obdelovalnih strojev, je torej zmanjšanje obsega obdelave in računanja pri ocenjevanju lege konca mehanizma. V članku sta predstavljeni zasnova in implementacija poenostavljenega algoritma za ocenjevanje lege omenjenih mehanizmov.

Najprej je sistematično predstavljena paralelna delovna glava 1T2R, temu pa sledi predstavitev kinematičnega modela paralelnega mehanizma. Sledita analiza položaja ter oblikovanje preslikave med vrednostmi vhodov in gibanjem konca mehanizma z inverzno kinematično rešitvijo. Na osnovi konstrukcije mehanizma, parametrov skaliranja, območja gibanja ter interferenc posameznih kinematičnih parov in drugih omejitev sta določeni množica vseh dosegljivih prostorskih položajev referenčne točke orodja na koncu mehanizma in množica dosegljivih orientacij orodja v dani referenčni točki. Z analizo zakona gibanja glave 1T2R je nato izpeljan poenostavljen algoritem za oceno njenega položaja in orientacije. Položaj referenčne točke na orodju glave je ocenjen s pomočjo vsote dolžin treh nog verige. Orientacija glave je ocenjena s pomočjo razlik v dolžini nog katerih koli dveh od treh vej. Kombinacija obeh zakonov omogoča hitro oceno položaja in orientacije glave z nezahtevnimi izračuni ter hiter odziv varovalne omejevalne funkcije z obstoječo strojno opremo za zaščito pred prekoračitvijo delovnega območja glave.

Pravilnost predlaganega poenostavljenega algoritma so potrdili tudi rezultati simulacij v nadaljevanju. Poenostavljeni algoritem za ocenjevanje položaja in orientacije je bil uporabljen v kombinaciji z mehansko konstrukcijo in krmilnim sistemom servopodajanja glave pri zasnovi dveh metod omejevanja – aktivne in preventivne. Eksperimenti so končno dokazali, da je s poenostavljenim algoritmom za oceno položaja in lege izvedljivo realnočasovno ocenjevanje položaja in lege konca mehanizma med obratovanjem paralelne delovne glave 1T2R. Algoritem daje točne ocene položaja in lege.

Na osnovi rezultatov kinematične analize in analize načina gibanja mehanizma je bil oblikovan predlog algoritma za oceno lege paralelne delovne glave 1T2R. Ta v primerjavi z metodo za ocenjevanje lege po modelu inverznega položaja prihrani 99,42 % računskega časa. Za razliko od metod za ocenjevanje lege, ki uporabljajo zunanje senzorje, ne zahteva nadgradnje originalnega sistema ter je učinkovit, zanesljiv in enostavno izvedljiv. Poenostavljeni algoritem za oceno položaja in lege tako omogoča preprosto in zanesljivo realnočasovno omejevanje položaja glave.

Algoritem trenutno pokriva celotni dosegljivi prostor mehanizma v območju omejevanja in tako izboljšuje zmožnosti hitrega odziva omejevalne funkcije za varnost obratovanja obdelovalnih strojev s tako topologijo.
Ključne besede: paralelna delovna glava, modeliranje, analiza delovnega prostora, ocena položaja in lege, varovanje z omejevanjem, inverzna kinematika

*Naslov avtorja za dopisovanje: Univerza v Tianjinu, Fakulteta za strojništvo, Kitajska, niyb5812@tju.edu.cn

Strojniški vestnik - Journal of Mechanical Engineering 68(2022)9, SI 74

Prejeto v recenzijo: 2022-07-08
Prejeto popravljeno: 2022-09-02
Odobreno za objavo: 2022-09-07

Analiza nelinearnih vibracij funkcionalno gradientnih poroznih plošč, ojačenih s ploščicami grafena, na nelinearnih elastičnih temeljih

Xiaolin Huang* – Chengzhe Wang – Jiaheng Wang – Nengguo Wei
Univerza za elektroniko v Guilinu, Šola za arhitekturo in transport, Kitajska

Pričujoči članek obravnava nelinearne vibracije plošč. Predstavljen je model na podlagi modificiranega mikromehanskega modela Halpin-Tsai in razširjenega zakona zmesi, namenjen vrednotenju lastnosti nanokompozitov z notranjimi porami, ojačenih z grafenom.

Predmet obravnave je funkcionalno gradientna porozna plošča na nelinearnih elastičnih temeljih, ojačena z grafenom. Upoštevane so tri vrste porazdelitve por, tako enakomerne kot neenakomerne. V študiji je predstavljen modificirani model, ki upošteva volumski delež por. Na podlagi modificiranega modela so bile ocenjene dejanske materialne lastnosti porozne plošče. Izpeljane so enačbe nelinearnih vibracij plošče v okviru teorije plošč višjega reda in splošnih Kármánovih enačb, ki upoštevajo vpliv sklopitve z nelinearnimi elastičnimi temelji. Za določitev nelinearnega frekvenčnega in dinamičnega odziva sta bili uporabljeni tehnika dvostopenjskih perturbacij in Galerkinova metoda.

Podrobno so preučeni vplivi por, ploščic grafena in elastičnih temeljev na lastno frekvenco porozne plošče. V predhodnih študijah je bilo ugotovljeno, da se lastna frekvenca monotono znižuje z rastjo koeficienta poroznosti. Izkazalo se je, da pravilo ne velja za dani primer. Koeficient poroznosti pri porazdelitvah por P-1 in P-3 vpliva na vrednosti parametrov temeljev. Pri vrednostih parametrov temeljev (50, 0) in (0, 0) se lastna frekvenca zmanjša, za lastno frekvenco pri parametrih (50, 50) pa velja nasprotno. Preučen je bil tudi vpliv prehodnega odklona. Največji odklon se ob dvigu koeficienta poroznosti z 0,0 na 0,4 poveča za približno 8 % Sledi sklep, da je vpliv koeficienta poroznosti na dinamični odziv zanemarljiv.

Reševanje nelinearnih vodilnih enačb gibanja porozne plošče je zelo težavno, zato je bilo mogoče pridobiti samo asimptotske rešitve tretjega reda. Avtorji nameravajo v prihodnjih raziskavah poiskati asimptotske rešitve višjega reda.

V članku je predstavljen modificiran model za vrednotenje materialnih lastnosti funkcionalno gradientnih nanokompozitov, ojačenih z grafenom. Podanih je več zanimivih ugotovitev v zvezi z vplivom por in nelinearnih elastičnih temeljev. Rezultati bodo lahko uporabni pri projektiranju podobnih konstrukcij v praksi.

Ključne besede: funkcionalno gradientni porozni nanokompoziti, ploščice grafena, pore, nelinearni elastični temelji, nelinearne vibracije, prehodni odgovor

*Naslov avtorja za dopisovanje: Univerza za elektroniko v Guilinu, Šola za arhitekturo in transport, Jinji Road 1#, Guilin, Kitajska, xlhuang@guet.edu.cn

Guide for Authors

All manuscripts must be in English. Pages should be numbered sequentially. The manuscript should be composed in accordance with the Article Template given above. The suggested length of contributions is 10 to 20 pages. Longer contributions will only be accepted if authors provide justification in a cover letter. For full instructions see the Information for Authors section on the journal's website: http://en.sv-jme.eu .

SUBMISSION:

Submission to SV-JME is made with the implicit understanding that neither the manuscript nor the essence of its content has been published previously either in whole or in part and that it is not being considered for publication elsewhere. All the listed authors should have agreed on the content and the corresponding (submitting) author is responsible for having ensured that this agreement has been reached. The acceptance of an article is based entirely on its scientific merit, as judged by peer review. Scientific articles comprising simulations only will not be accepted for publication; simulations must be accompanied by experimental results carried out to confirm or deny the accuracy of the simulation. Every manuscript submitted to the SV-JME undergoes a peer-review process.

The authors are kindly invited to submit the paper through our web site: http://ojs.sv-jme.eu. The Author is able to track the submission through the editorial process - as well as participate in the copyediting and proofreading of submissions accepted for publication - by logging in, and using the username and password provided.

SUBMISSION CONTENT:

The typical submission material consists of:

- A **manuscript** (A PDF file, with title, all authors with affiliations, abstract, keywords, highlights, inserted figures and tables and references),
- Supplementary files:
  - a **manuscript** in a WORD file format
  - a **cover letter** (please see instructions for composing the cover letter)
  - a ZIP file containing **figures** in high resolution in one of the graphical formats (please see instructions for preparing the figure files)
  - possible **appendicies** (optional), cover materials, video materials, etc.

Incomplete or improperly prepared submissions will be rejected with explanatory comments provided. In this case we will kindly ask the authors to carefully read the Information for Authors and to resubmit their manuscripts taking into consideration our comments.

COVER LETTER INSTRUCTIONS:

Please add a **cover letter** stating the following information about the submitted paper:

1. Paper **title**, list of **authors** and their **affiliations**. **One** corresponding author should be provided.
2. **Type of paper**: original scientific paper (1.01), review scientific paper (1.02) or short scientific paper (1.03).
3. A **declaration** that neither the manuscript nor the essence of its content has been published in whole or in part previously and that it is not being considered for publication elsewhere.
4. State the **value of the paper** or its practical, theoretical and scientific implications. What is new in the paper with respect to the state-of-the-art in the published papers? Do not repeat the content of your abstract for this purpose.
5. We kindly ask you to suggest at least two **reviewers** for your paper and give us their names, their full affiliation and contact information, and their scientific research interest. The suggested reviewers should have at least two relevant references (with an impact factor) to the scientific field concerned; they should not be from the same country as the authors and should have no close connection with the authors.

FORMAT OF THE MANUSCRIPT:

The manuscript should be composed in accordance with the Article Template. The manuscript should be written in the following format:

- A **Title** that adequately describes the content of the manuscript.
- A list of **Authors** and their **affiliations**.
- An **Abstract** that should not exceed 250 words. The Abstract should state the principal objectives and the scope of the investigation, as well as the methodology employed. It should summarize the results and state the principal conclusions.
- 4 to 6 significant **key words** should follow the abstract to aid indexing.
- 4 to 6 **highlights;** a short collection of bullet points that convey the core findings and provide readers with a quick textual overview of the article. These four to six bullet points should describe the essence of the research (e.g. results or conclusions) and highlight what is distinctive about it.
- An **Introduction** that should provide a review of recent literature and sufficient background information to allow the results of the article to be understood and evaluated.
- A **Methods** section detailing the theoretical or experimental methods used.
- An **Experimental section** that should provide details of the experimental set-up and the methods used to obtain the results.
- A **Results** section that should clearly and concisely present the data, using figures and tables where appropriate.
- A **Discussion** section that should describe the relationships and generalizations shown by the results and discuss the significance of the results, making comparisons with previously published work. (It may be appropriate to combine the Results and Discussion sections into a single section to improve clarity.)
- A **Conclusions** section that should present one or more conclusions drawn from the results and subsequent discussion and should not duplicate the Abstract.
- **Acknowledgement** (optional) of collaboration or preparation assistance may be included. Please note the source of funding for the research.
- **Nomenclature** (optional). Papers with many symbols should have a nomenclature that defines all symbols with units, inserted above the references. If one is used, it must contain all the symbols used in the manuscript and the definitions should not be repeated in the text. In all cases, identify the symbols used if they are not widely recognized in the profession. Define acronyms in the text, not in the nomenclature.
- **References** must be cited consecutively in the text using square brackets [1] and collected together in a reference list at the end of the manuscript.
- **Appendix(-icies)** if any.

SPECIAL NOTES

Units: The SI system of units for nomenclature, symbols and abbreviations should be followed closely. Symbols for physical quantities in the text should be written in italics (e.g. *v*, *T*, *n*, etc.). Symbols for units that consist of letters should be in plain text (e.g. ms^{-1}, K, min, mm, etc.). Please also see: http://physics.nist.gov/cuu/pdf/sp811.pdf .

Abbreviations should be spelt out in full on first appearance followed by the abbreviation in parentheses, e.g. variable time geometry (VTG). The meaning of symbols and units belonging to symbols should be explained in each case or cited in a **nomenclature** section at the end of the manuscript before the References.

Figures (figures, graphs, illustrations digital images, photographs) must be cited in consecutive numerical order in the text and referred to in both the text and the captions as Fig. 1, Fig. 2, etc. Figures should be prepared without borders and on white grounding and should be sent separately in their original formats. If a figure is composed of several parts, please mark each part with a), b), c), etc. and provide an explanation for each part in Figure caption. The caption should be self-explanatory. Letters and numbers should be readable (Arial or Times New Roman, min 6 pt with equal sizes and fonts in all figures). Graphics (submitted as supplementary files) may be exported in resolution good enough for printing (min. 300 dpi) in any common format, e.g. TIFF, BMP or JPG, PDF and should be named Fig1.jpg, Fig2.tif, etc. However, graphs and line drawings should be prepared as vector images, e.g. CDR, AI. Multi-curve graphs should have individual curves marked with a symbol or otherwise provide distinguishing differences using, for example, different thicknesses or dashing.

Tables should carry separate titles and must be numbered in consecutive numerical order in the text and referred to in both the text and the captions as Table 1, Table 2, etc. In addition to the physical quantities, such as *t* (in italics), the units [s] (normal text) should be added in square brackets. Tables should not duplicate data found elsewhere in the manuscript. Tables should be prepared using a table editor and not inserted as a graphic.

REFERENCES:

A reference list must be included using the following information as a guide. Only cited text references are to be included. Each reference is to be referred to in the text by a number enclosed in a square bracket (i.e. [3] or [2] to [4] for more references; do not combine more than 3 references, explain each). No reference to the author is necessary.

References must be numbered and ordered according to where they are first mentioned in the paper, not alphabetically. All references must be complete and accurate. Please add DOI code when available. Examples follow.

Journal Papers:

Surname 1, Initials, Surname 2, Initials (year). Title. *Journal*, volume, number, pages, DOI code.

[1] Hackenschmidt, R., Alber-Laukant, B., Rieg, F. (2010). Simulating nonlinear materials under centrifugal forces by using intelligent cross-linked simulations. *Strojniški vestnik - Journal of Mechanical Engineering,* vol. 57, no. 7-8, p. 531-538, DOI:10.5545/sv-jme.2011.013.

Journal titles should not be abbreviated. Note that journal title is set in italics.

Books:

Surname 1, Initials, Surname 2, Initials (year). Title. Publisher, place of publication.

[2] Groover, M.P. (2007). *Fundamentals of Modern Manufacturing*. John Wiley & Sons, Hoboken.

Note that the title of the book is italicized.

Chapters in Books:

Surname 1, Initials, Surname 2, Initials (year). Chapter title. Editor(s) of book, book title. Publisher, place of publication, pages.

[3] Carbone, G., Ceccarelli, M. (2005). Legged robotic systems. Kordić, V., Lazinica, A., Merdan, M. (Eds.), Cutting Edge Robotics. Pro literatur Verlag, Mammendorf, p. 553-576.

Proceedings Papers:

Surname 1, Initials, Surname 2, Initials (year). Paper title. Proceedings title, pages.

[4] Štefanić, N., Martinčević-Mikić, S., Tošanović, N. (2009). Applied lean system in process industry. *MOTSP Conference Proceedings*, p. 422-427.

Standards:

Standard-Code (year). Title. Organisation. Place.

[5] ISO/DIS 16000-6.2:2002. *Indoor Air – Part 6: Determination of Volatile Organic Compounds in Indoor and Chamber Air by Active Sampling on TENAX TA Sorbent, Thermal Desorption and Gas Chromatography using MSD/FID.* International Organization for Standardization. Geneva.

WWW pages:

Surname, Initials or Company name. Title, from http://address, date of access.

[6] Rockwell Automation. Arena, from *http://www.arenasimulation.com,* accessed on 2009-09-07.

EXTENDED ABSTRACT:

When the paper is accepted for publishing, the authors will be requested to send an **extended abstract** (approx. one A4 page or 3500 to 4000 characters or approx. 600 words). The instruction for composing the extended abstract are published on-line: http://www.sv-jme.eu/information-for-authors/ .

COPYRIGHT:

Authors submitting a manuscript do so on the understanding that the work has not been published before, is not being considered for publication elsewhere and has been read and approved by all authors. The submission of the manuscript by the authors means that the authors automatically agree to publish the paper uder CC-BY 4.0 Int. or CC-BY-NC 4.0 Int. when the manuscript is accepted for publication. All accepted manuscripts must be accompanied by a Copyright Agreement, which should be sent to the editor. The work should be original work by the authors and not be published elsewhere in any language without the written consent of the publisher. The proof will be sent to the author showing the final layout of the article. Proof correction must be minimal and executed quickly. Thus it is essential that manuscripts are accurate when submitted. Authors can track the status of their accepted articles on https://en.sv-jme.eu/.

PUBLICATION FEE:

Authors will be asked to pay a publication fee for each article prior to the article appearing in the journal. However, this fee only needs to be paid after the article has been accepted for publishing. The fee is 380 EUR (for articles with maximum of 6 pages), 470 EUR (for articles with maximum of 10 pages), plus 50 EUR for each additional page. The additional cost for a color page is 90.00 EUR (only for a journal hard copy; optional upon author's request). These fees do not include tax.

Strojniški vestnik -Journal of Mechanical Engineering
Aškerčeva 6, 1000 Ljubljana, Slovenia, e-mail: info@sv-jme.eu

9 770039 248001
ISSN 0039-2480

http://www.sv-jme.eu

Contents

Papers